

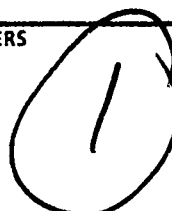
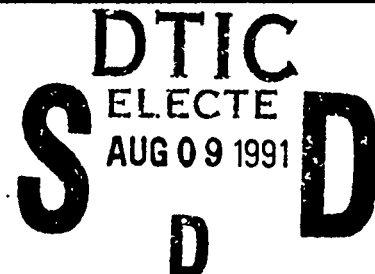

AD-A239 311



## DOCUMENTATION PAGE

Form Approved  
OMB No. 0704-0188

Information is estimated to average 1 hour per response, including the time for reviewing instructions, searching existing data sources, gathering and completing the collection of information. Send comments regarding this burden estimate or any other aspect of this form, including suggestions for reducing this burden, to Washington Headquarters Services, Directorate for Information Operations and Reports, 1215 Jefferson Avenue, Washington, DC 20540, and to the Office of Management and Budget, Paperwork Reduction Project (0704-0188), Washington, DC 20503.

1. AGENCY USE ONLY (Leave blank)		2. REPORT DATE May 1991	3. REPORT TYPE AND DATES COVERED XXXXXX DISSERTATION
4. TITLE AND SUBTITLE Pion Elastic and Inelastic Scattering from 15N			5. FUNDING NUMBERS 
6. AUTHOR(S) David P. Saunders, Captain			
7. PERFORMING ORGANIZATION NAME(S) AND ADDRESS(ES) AFIT Student Attending: University of Texas			8. PERFORMING ORGANIZATION REPORT NUMBER AFIT/CI/CIA- 91-012d
9. SPONSORING / MONITORING AGENCY NAME(S) AND ADDRESS(ES) AFIT/CI Wright-Patterson AFB OH 45433-6583			10. SPONSORING / MONITORING AGENCY REPORT NUMBER
11. SUPPLEMENTARY NOTES			
12a. DISTRIBUTION / AVAILABILITY STATEMENT Approved for Public Release IAW 190-1 Distributed Unlimited ERNEST A. HAYGOOD, 1st Lt, USAF Executive Officer			12b. DISTRIBUTION CODE
13. ABSTRACT (Maximum 200 words) <div style="text-align: center;"> 42 91-07361 </div>			
14. SUBJECT TERMS			15. NUMBER OF PAGES 165
			16. PRICE CODE
17. SECURITY CLASSIFICATION OF REPORT	18. SECURITY CLASSIFICATION OF THIS PAGE	19. SECURITY CLASSIFICATION OF ABSTRACT	20. LIMITATION OF ABSTRACT

# PION ELASTIC AND INELASTIC SCATTERING FROM $^{15}\text{N}$

APPROVED BY

SUPERVISORY COMMITTEE:

Accession For	
NTIS CRA&I	<input checked="" type="checkbox"/>
DTIC TAB	<input type="checkbox"/>
Unannounced	<input type="checkbox"/>
Justification	
By	
Distribution/	
Availability Codes	
Dist	Avail and/or Special
A-1	

*[Signature]*  
*[Signature]*  
*T. Udagawa*  
*RA KJ*  
*S. J. Suster*



Copyright  
by  
David Patrick Saunders  
1991

For Debbi and David.

**PION ELASTIC AND INELASTIC SCATTERING  
FROM  $^{15}\text{N}$**

**by**

**DAVID PATRICK SAUNDERS, B.S., M.A.**

**DISSERTATION**

**Presented to the Faculty of the Graduate School of**

**The University of Texas at Austin**

**in Partial Fulfillment**

**of the Requirements**

**for the Degree of**

**DOCTOR OF PHILOSOPHY**

**THE UNIVERSITY OF TEXAS AT AUSTIN**

**May, 1991**

## Acknowledgments

Thanks to my advisor, Professor C. Fred Moore, for keeping me on board while I went off to do other things, and for threatening me when I needed it. Special thanks to Dr. Susan Seestrom for allowing me to use her experiment for my dissertation, and for all the direction she gave me during its analysis, to Dr. Mike Franey and Allen Williams for their enlightening discussions and support, to Dr. Mohini Rawool-Sullivan for her proofreading of this manuscript, and to Herb Ward for his invaluable help. I would also like to thank Dr. Chris Morris, all the MP-10 staff, and all of the LAMPF collaborators and staff for their help to me in running, analyzing, and understanding the experiment. Many thanks to Captain Doug Lier (USN Retired) for his unceasing support of my work through the Service Academy Research Associate Program, as well as the myriad other means through which he aided me here at Los Alamos. Thanks are also due to Frank J. Seiler Research Lab at the Air Force Academy for sponsoring me to finish off my Ph.D. this past year. Finally, I would like to thank the U. S. Department of Energy, the Robert A. Welch Foundation, and the United States Air Force for their support.

DAVID PATRICK SAUNDERS

The University of Texas at Austin

May, 1991

## Table of Contents

<b>Acknowledgments</b>	<b>v</b>
<b>Table of Contents</b>	<b>vi</b>
<b>List of Tables</b>	<b>viii</b>
<b>List of Figures</b>	<b>ix</b>
<b>Abstract</b>	<b>xiv</b>
<b>1. Introduction</b>	<b>1</b>
<b>2. Experimental Apparatus and Procedure</b>	<b>13</b>
2.1 Accelerator . . . . .	13
2.2 EPICS . . . . .	15
2.2.1 EPICS Channel . . . . .	17
2.2.2 EPICS Scattering Chamber . . . . .	19
2.2.3 EPICS Spectrometer . . . . .	21
2.2.4 EPICS Detector System . . . . .	21
2.2.5 Data Acquisition and Analysis System . . . . .	29
2.3 Experimental Detail . . . . .	31
<b>3. Data Analysis and Results</b>	<b>33</b>
3.1 Event Analysis . . . . .	33

3.2	Data Reduction . . . . .	43
3.3	Data . . . . .	51
<b>4.</b>	<b>Theoretical Interpretations of the Data</b>	<b>55</b>
4.1	Theoretical Models for Elastic Scattering . . . . .	56
4.2	Theoretical Models for Inelastic Scattering . . . . .	60
4.3	Theoretical Results . . . . .	62
4.3.1	Elastic Scattering . . . . .	62
4.3.2	Inelastic Scattering . . . . .	69
4.4	Discussion . . . . .	87
4.4.1	Low Lying Positive Parity States . . . . .	87
4.4.2	High Lying Positive Parity States . . . . .	91
4.4.3	Stretched (M4) Excitation States . . . . .	94
4.4.4	Negative Parity States . . . . .	100
<b>5.</b>	<b>Summary</b>	<b>103</b>
<b>A.</b>	<b>Experimental Data Plots</b>	<b>106</b>
<b>B.</b>	<b>Tabulated Data</b>	<b>134</b>
	<b>BIBLIOGRAPHY</b>	<b>163</b>
	Vita	



## List of Tables

2.1	EPICS system specifications* . . . . .	19
3.1	Weighted average experimental $\frac{\sigma(\pi^+)}{\sigma(\pi^-)}$ cross section ratios. . .	53
4.1	Phase shifts* $\delta_l$ used in PIPIT calculations. . . . .	57
4.2	Neutron(n) and proton(p) One Body Density Matrix Elements for calculations made on excitation of positive parity $J^\pi = \frac{1}{2}^+$ states in $^{15}\text{N}$ with a $1-\hbar\omega$ basis. . . . .	84
4.3	Neutron(n) and proton(p) One Body Density Matrix Elements for calculations made on excitation of positive parity $J^\pi = \frac{3}{2}^+$ states in $^{15}\text{N}$ with a $1-\hbar\omega$ basis. . . . .	85
4.4	Neutron(n) and proton(p) One Body Density Matrix Elements for calculations made on excitation of positive parity $J^\pi =$ $\frac{5}{2}^+, \frac{7}{2}^+$ states in $^{15}\text{N}$ with a $1-\hbar\omega$ basis. . . . .	86

## List of Figures

1.1	$\pi^\pm$ -N cross sections as a function of pion energy. . . . .	6
1.2	$^{15}\text{N}$ shell model. . . . .	8
1.3	$^{13}\text{C}$ stretched state configurations. . . . .	10
1.4	$^{15}\text{N}$ stretched state configurations. . . . .	11
2.1	LAMPF Facility. . . . .	14
2.2	LAMPF Experimental Area and Switchyard. . . . .	16
2.3	Energetic Pion Channel and Spectrometer. . . . .	17
2.4	EPICS Channel and Optics. . . . .	18
2.5	EPICS Cooled Gas Target Vessel and System. . . . .	20
2.6	EPICS Spectrometer. . . . .	22
2.7	EPICS Spectrometer optics and Detector System. . . . .	23
2.8	Kinematics calculation flow chart. . . . .	24
2.9	EPICS wire chamber wire plane representation. . . . .	25
2.10	EPICS Data Acquisition Electronics/Logic System. . . . .	30
2.11	Illustration of change in effective target thickness with angle for EPICS spectrometer with cooled gas cylindrical target vessel.	32
3.1	LAMPF Experiment 703 Data Display File, Exp703.set. . . .	34

3.2	Experiment 703 Test File, Exp703.tst, loop 1. . . . .	35
3.3	Experiment 703 Data Replay Particle Identification (PID) Box. . . . .	35
3.4	Experiment 703 Test File, Exp703.tst, loop 2. . . . .	36
3.5	Experiment 703 Test File, Exp703.tst, loop 3. . . . .	39
3.6	Experiment 703 $X_{tgt}$ Histogram. . . . .	40
3.7	Experiment 703 $\theta_{tgt}$ Histogram. . . . .	41
3.8	Experiment 703 Test File, Exp703.tst, loop 4. . . . .	42
3.9	The 60° 164 MeV $\pi^+$ Spectrum, along with a fit to its 0 MeV region. . . . .	44
3.10	The 60° 164 MeV $\pi^+$ Spectrum, along with a fit to its 4.5-14.2 MeV region. . . . .	45
3.11	The 60° 164 MeV $\pi^+$ Spectrum, along with a fit to its 14.2-19.5 MeV region. . . . .	46
3.12	Epics spectrometer $\delta$ -scan. . . . .	48
3.13	70° $\pi^+$ and $\pi^-$ spectra, along with the difference spectrum between the $\pi^\pm$ runs. . . . .	52
4.1	Elastic $\pi^\pm$ data with DWPI (dashed line) and PIPIT (solid line) calculations. . . . .	63
4.2	Effect of variation of energy shift elastic input parameter on in- elastic calculations performed with DWPI. Solid lines, dashed lines, and dotted lines are $E_{sh}=23, 28,$ and $33$ MeV, respectively. . . . .	65

4.3	Effect of variation of energy shift elastic input parameter to PIPIT on inelastic calculations performed with ARPIN. Solid lines, dashed lines, and dotted lines are $E_{sh}=18, 23$ , and $28$ MeV, respectively. . . . .	66
4.4	Effect of variation of momentum space s wave damping factor elastic input parameter, DAMP1, to PIPIT on inelastic calculations performed with ARPIN. Solid lines, dashed lines, and dotted lines are $DAMP1= 3 \times 10^{-6}, 3 \times 10^{-5}$ , and $1.5 \times 10^{-4}$ , respectively. . . . .	67
4.5	Effect of variation of momentum space p wave damping factor elastic input parameter, DAMP2, to PIPIT on inelastic calculations performed with ARPIN. Solid lines, dashed lines, and dotted lines are $DAMP2= 2.5 \times 10^{-7}, 2.5 \times 10^{-6}$ , and $2.5 \times 10^{-5}$ , respectively. . . . .	68
4.6	DWPI macroscopic model calculation results for states with excitation energies from $5.27$ to $9.15$ MeV. . . . .	70
4.7	DWPI macroscopic model calculation results for states with excitation energies from $9.7$ to $14.4$ MeV. . . . .	71
4.8	DWPI macroscopic model calculation results for states with excitation energies from $14.6$ to $17.6$ MeV. . . . .	72
4.9	Results for ARPIN microscopic model calculations with no effective charge enhancements for states with excitation energies from $5.27$ to $7.57$ MeV. . . . .	73

4.10	Results for ARPIN microscopic model calculations with no effective charge enhancements for states with excitation energies from 11.2 to 15.1 MeV. . . . .	74
4.11	Results for ARPIN microscopic model calculations with effective charge enhancements for states with excitation energies from 5.27 to 8.31 MeV (The 8.31 MeV $\pi^+$ calculation has been multiplied by 100 here). . . . .	75
4.12	Results for ARPIN microscopic model calculations with effective charge enhancements for states with excitation energies from 8.57 to 15.1 MeV. . . . .	76
4.13	Results for ARPIN microscopic model calculations with effective charge enhancements for states with excitation energies from 16.4 to 19.0 MeV. For the state at 18.9 MeV, the dashed line is a $J = \frac{3}{2}$ calculation, the dotted line is a $J = \frac{1}{2}$ calculation, and the solid line is the sum of the two. . . . .	77
4.14	Constant momentum transfer excitation functions for states not identified as having "stretched" transitions with excitation energies from 5.27 to 11.9 MeV. . . . .	79
4.15	Constant momentum transfer excitation functions for states not identified as having "stretched" transitions with excitation energies from 13.1 to 18.3 MeV. . . . .	80
4.16	Constant momentum transfer excitation functions for states identified as having "stretched" transitions. . . . .	81

4.17 $\pi^+$ angular distribution and $70^\circ$ differential cross section, along with a pure M4 calculation, for 164 MeV pion scattering from $^{15}\text{N}$ to the excited state at 10.7 MeV. . . . .	95
4.18 $\pi^\pm$ angular distributions, along with a M4 calculation (dotted line), a C2 calculation (chain-dash lines), and the sum of these two calculations (solid line), for 164 MeV pion scattering from $^{15}\text{N}$ to the excited state at 12.5 MeV. . . . .	96
4.19 $\pi^\pm$ angular distributions, along with a M4 calculation (dotted line), a C3 calculation (chain-dash lines), and the sum of these two calculations (solid line), for 164 MeV pion scattering from $^{15}\text{N}$ to the excited state at 14.1 MeV. . . . .	97
4.20 $\pi^\pm$ angular distributions, along with a M4 calculation (dotted line), a C2 calculation (chain-dash lines), and the sum of these two calculations (solid line), for 164 MeV pion scattering from $^{15}\text{N}$ to the excited state at 17.2 MeV. . . . .	98
4.21 Calculations along with data for the negative parity "single hole" state at 6.32 MeV. . . . .	102

# PION ELASTIC AND INELASTIC SCATTERING FROM $^{15}\text{N}$

Publication No. \_\_\_\_\_

David Patrick Saunders, Ph.D.

The University of Texas at Austin, 1991

Supervisor: C. F. Moore

*N. Troger. 15*

→ Data were obtained on the Clinton P. Anderson Los Alamos Meson Physics Facility Energetic Pion Channel and Spectrometer for elastic and inelastic pion scattering from ground state  $^{15}\text{N}$  nuclei. States observed here included those of 0.0, 5.27, 6.32, 7.16, 7.30, 7.57, 8.31, 8.57, 9.15, 9.76, 9.9, 10.7, 11.3, 11.9, 12.5, 12.9, 13.1, 14.1, 14.4, 14.6, 15.0, 16.5, 16.9, 17.2, 17.6, 18.3, 18.7, and 18.9 MeV excitation energies. Angular distributions were obtained for scattering at angles from  $25^\circ$  to  $90^\circ$  in  $5^\circ$  increments with an incident pion energy of 164 MeV. Optical model analyses of the elastic (0 MeV) angular distributions with equal point proton and neutron densities in both momentum and coordinate space formulations accurately predict the data, although the two formulations require different energy shifts to do so. This difference is thought to be a result of the more accurate nonlocal representation of the nuclear potential in the momentum space code. Additional spectra were obtained for scattering at constant momentum transfers of .94 and  $1.57 \text{ fm}^{-1}$  in *deg*

*1.57 1.5*

*Cross section*

order to generate constant momentum transfer excitation functions. Use of these excitation functions,  $\left(\frac{\sigma(\pi^+)}{\sigma(\pi^-)}\right)$  ratios, and shell model DWIA calculations allowed identification of several excited states having shell-model-like, single particle-hole, pure spin-flip excitations. Shell model and collective model DWIA calculations, as well as the  $q = .94$  and  $1.57/\text{fm}^{-1}$  excitation functions and the  $\left(\frac{\sigma(\pi^+)}{\sigma(\pi^-)}\right)$  ratios indicate that the other states are generally well represented by a shell model description with collective enhancements.

*cross section*



# Chapter 1

## Introduction

In 1935 Yukawa[YU35] predicted, by a field theoretical treatment, the existence of a particle of approximately  $100 \text{ MeV}/c^2$  mass as the field quantum of the nuclear force. This particle, the pion ( $\pi$ ), was first observed by Powell *et. al.* at the University of Bristol in England as a component of cosmic radiation using photo emulsions. The pion was first artificially produced in 1948 by Gardner and Lattes at the University of California Radiation Laboratory's Synchrocyclotron facility. It very quickly became evident that pions had many advantages in their use for the study of nuclei and nuclear interactions because of their interaction via the strong force, but there were no facilities for production of pions on a scale large enough to do these studies. Initial studies therefore concentrated on pion production cross sections and basic properties. This was the case until the early 1970's, when the "Meson Factories" at the Los Alamos Meson Physics Facility (LAMPF) in the United States, the Swiss Institute for Nuclear Research (SIN) in Switzerland, and the Tri-University Meson Facility (TRIUMF) in Canada came into being.

These facilities produced relatively high current pion beams, and enabled high resolution studies of nuclear structure using the pion. The experiment presented here is one of hundreds performed to date at LAMPF in pursuit of a knowledge of nuclear structure, and it specifically targets the  $^{15}\text{N}$  nucleus.

A knowledge of the basic properties of the pion, along with some of the characteristics of its interactions with nucleons and nuclei is necessary to understanding its advantages as a probe of nuclear structure. The pion is the field quantum of the strong or nuclear force. Specifically, it is the mediator of the longest range, attractive portion of this force, with heavier mesons mediating the shorter range repulsive forces of the nuclear core. It is a pseudoscalar, spin-parity  $(J^\pi) = 0^-$  meson. Herein lies the first of its advantages as a nuclear probe. The fact that it has spin 0, as opposed to  $\frac{1}{2}$  for other probes in popular use, reduces the number of individual initial to final state scattering amplitudes, so that angular momentum considerations lead to a much simpler two-body scattering amplitude.

The pion has 3 charge states,  $\pi^+$ ,  $\pi^0$ , and  $\pi^-$ , and so has isospin  $T=1$ . Because of this, states of higher isospin are obtainable with pion scattering than can be reached with other probes. One of the states that can be reached using the pion is the  $\Delta(1232)$  or  $\Delta(3,3)$  resonance, where 1232 is the energy of the resonance in MeV, and (3,3) represents the spin and isospin ( $2J=3, 2T=3$ ) of the state. The isospin identification of this resonance is made based on conclusions drawn from the assumption of isospin invariance for the strong interaction and isospin algebra performed for  $\pi$ -nucleon ( $\pi$ -N) scattering through this state. With the (experimentally supported) assumption of isospin invariance of the strong interaction (and ignoring the coulomb interaction) comes the requirement that the amplitudes for scattering from the nuclear potential depend only on the system's total isospin[LE73]. So, for states obtained in  $\pi$ -N scattering the cross sections are only dependent on scattering amplitudes, denoted by the symbol  $f$ , associated with  $|\vec{T}_\pi + \vec{T}_N| = \frac{1}{2}, \frac{3}{2}$ . These amplitudes are  $f_{\frac{1}{2}}$  and  $f_{\frac{3}{2}}$ ,

respectively. Because of conservation of isospin and charge there is nonzero amplitude only when isospin and z component of isospin are both conserved:

$$\langle T, T_z | f_T | T', T'_z \rangle \neq 0 \quad (1.1)$$

only if  $T = T'$  and  $T_z = T'_z$ . Now, with the conventions:

$$\begin{aligned} |T, T_z\rangle = & \quad |1, 1\rangle \quad \text{for } \pi^+ \\ & |1, 0\rangle \quad \text{for } \pi^0 \\ & |1, -1\rangle \quad \text{for } \pi^- \\ & |\frac{1}{2}, \frac{1}{2}\rangle \quad \text{for proton (p)} \\ & |\frac{1}{2}, -\frac{1}{2}\rangle \quad \text{for neutron (n)} \end{aligned}$$

one can calculate the scattering cross section:

$$\sigma_{\pi^+p} = |\langle \pi^+ p | f | \pi^+ p \rangle|^2 \quad (1.2)$$

and

$$\begin{aligned} \langle \pi^+ p | f | \pi^+ p \rangle &= \langle \frac{1}{2}, \frac{1}{2} | \langle 1, 1 | f | \frac{1}{2}, \frac{1}{2} \rangle | 1, 1 \rangle \\ &= \langle \frac{3}{2}, \frac{3}{2} | f | \frac{3}{2}, \frac{3}{2} \rangle \end{aligned} \quad (1.3)$$

From equation 1.1,  $f$  must equal  $f_{\frac{3}{2}}$ , so that

$$\sigma_{\pi^+p} \propto |f_{\frac{3}{2}}|^2 \quad (1.4)$$

One may also calculate, by applying the isospin raising operator to the  $T = \frac{3}{2}$ ,  $T_z = \frac{3}{2}^-$  state, the  $T = \frac{3}{2}$  components of the  $\pi^-p$  cross sections:

$$\sigma_{\pi^-p \rightarrow \pi^-p} = |\langle \pi^- p | f_{\frac{3}{2}} | \pi^- p \rangle|^2 \quad (1.5)$$

and

$$\sigma_{\pi^- p \rightarrow \pi^0 p} = | \langle \pi^- p | f_{\frac{3}{2}} | \pi^0 p \rangle |^2 \quad (1.6)$$

raising the  $|\frac{3}{2}, -\frac{3}{2}\rangle$  state:

$$\begin{aligned} |\frac{3}{2}, -\frac{3}{2}\rangle &\rightarrow \alpha |\pi^- p\rangle + \beta |\pi^0 n\rangle \\ &= \alpha |1, -1\rangle |\frac{1}{2}, \frac{1}{2}\rangle + \beta |1, 0\rangle |\frac{1}{2}, -\frac{1}{2}\rangle \\ &= \gamma T^+ |\frac{3}{2}, -\frac{3}{2}\rangle \\ &= \frac{1}{\hbar \sqrt{2T(\pi) + 1}} (T_\pi^+ + T_n^+) |T(\pi), T_z(\pi^-)\rangle |T(n), T_z(n)\rangle \\ &= \frac{1}{\hbar \sqrt{2T(\pi) + 1}} [\hbar \sqrt{2T(\pi)} |1, 0\rangle |\frac{1}{2}, -\frac{1}{2}\rangle + \hbar |1, -1\rangle |\frac{1}{2}, \frac{1}{2}\rangle] \\ &= \sqrt{\frac{2}{3}} |\pi^0, n\rangle + \sqrt{\frac{1}{3}} |\pi^-, p\rangle \end{aligned}$$

so for the amplitudes:

$$\langle \pi^- p | f_{\frac{3}{2}} | \pi^- p \rangle = \sqrt{\frac{1}{3}} f_{\frac{3}{2}} \sqrt{\frac{1}{3}} = \frac{1}{3} f_{\frac{3}{2}} \quad (1.7)$$

$$\langle \pi^- p | f_{\frac{3}{2}} | \pi^0 n \rangle = \sqrt{\frac{1}{3}} f_{\frac{3}{2}} \sqrt{\frac{2}{3}} = \frac{\sqrt{2}}{3} f_{\frac{3}{2}} \quad (1.8)$$

For the  $f_{\frac{1}{2}}$  amplitudes, simply looking up the Clebsch-Gordon Coefficients instead of using isospin algebra:

$$\langle \pi^- p | f_{\frac{1}{2}} | \pi^- p \rangle = \frac{2}{3} f_{\frac{1}{2}} \quad (1.9)$$

$$\langle \pi^- p | f_{\frac{1}{2}} | \pi^0 n \rangle = -\frac{\sqrt{2}}{3} f_{\frac{1}{2}} \quad (1.10)$$

so for the total cross sections come the relations:

$$\sigma_{\pi^+ p \rightarrow \pi^+ p} \propto |f_{\frac{3}{2}}|^2 \quad (1.11)$$

$$\sigma_{\pi^-p \rightarrow \pi^-p} \propto \left| \frac{1}{3}f_{\frac{3}{2}} + \frac{2}{3}f_{\frac{1}{2}} \right|^2 \quad (1.12)$$

$$\sigma_{\pi^-p \rightarrow \pi^0n} \propto \left| \frac{\sqrt{2}}{3}f_{\frac{3}{2}} + \frac{\sqrt{2}}{3}f_{\frac{1}{2}} \right|^2 \quad (1.13)$$

If the  $\Delta(1232)$  resonance has  $T = \frac{3}{2}$  only the  $f_{\frac{3}{2}}$  amplitudes should be involved, and the result should be:

$$\sigma_{\pi^+p \rightarrow \pi^+p} : \sigma_{\pi^-p \rightarrow \pi^-p} : \sigma_{\pi^-p \rightarrow \pi^0n} = 9 : 1 : 2 \quad (1.14)$$

which is the experimentally observed result (see figure 1.1), so that  $T = \frac{1}{2}$  contributions to this resonance are very small[LE73]. Similarly, neutron scattering ratios are seen to be:

$$\sigma_{\pi^-n \rightarrow \pi^-n} : \sigma_{\pi^+n \rightarrow \pi^+n} : \sigma_{\pi^+n \rightarrow \pi^0p} = 9 : 1 : 2 \quad (1.15)$$

These strong  $\frac{\sigma(\pi^+)}{\sigma(\pi^-)}$  ratios for neutron and proton scattering are the basis of the third reason that pion scattering is so attractive for use in nuclear structure studies. An optical potential for  $\pi$ -nucleus ( $\pi$ -A) scattering can be described in terms of the  $\pi$ -N scattering amplitudes using an impulse approximation[LE80, LE80A]. This fact means that the same large  $\frac{\sigma(\pi^+)}{\sigma(\pi^-)}$  ratios should be present in  $\pi$ -A inelastic scattering that is dominated by pure proton or neutron excitation. This has been shown to be true for pure proton and pure neutron transitions in  $^{13}\text{C}$ [DE79] and  $^{14}\text{C}$ [HO85]. Pion scattering therefore aids in assessment of the extent to which the shell model is valid, separation of neutron and proton contributions to nuclear excited states, study of how important collective enhancements are to shell model states, and identification of purely collective states.

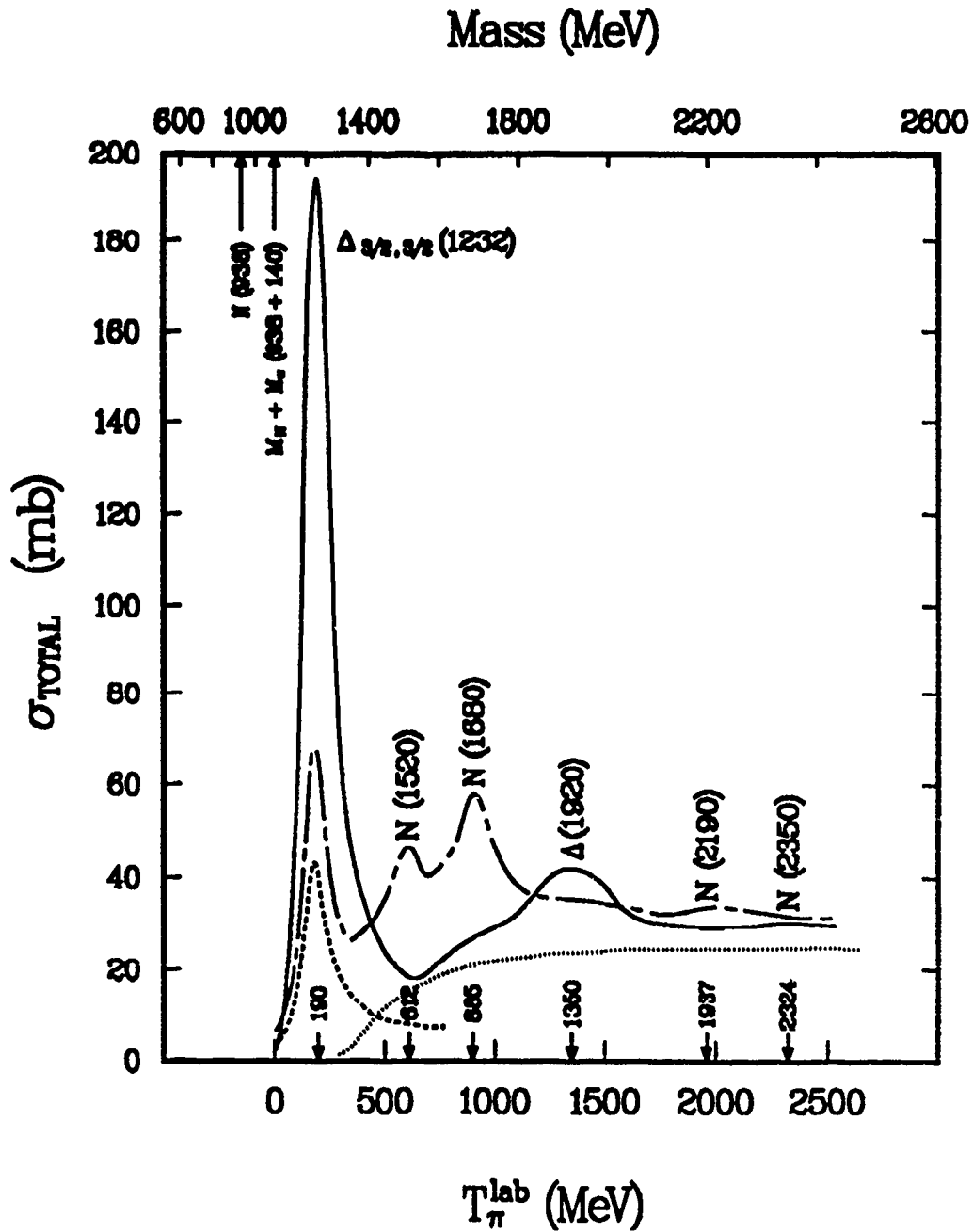


Figure 1.1:  $\pi^{\pm}$ -N cross sections as a function of pion energy. The solid line is the  $\pi^{+} - p$  or  $\pi^{-} - n$ , the chain-dashed line is the total  $\pi^{+} - n$  or  $\pi^{-} - p$ , the dashed line is the  $\pi^{+} - n \rightarrow \pi^{0} - p$  or  $\pi^{-} - p \rightarrow \pi^{0} - n$ , and the dotted line is the  $\pi^{+} - n$  or  $\pi^{-} - p$  inelastic cross section for the production of several pion states or heavier particles[KA64].

Siciliano and Walker[SI81] have shown that, assuming a single step reaction mechanism and using the impulse approximation, pion inelastic scattering can be used to assess the relative contributions of spin-flip ( $\Delta S = 1$ ) and non spin-flip ( $\Delta S = 0$ ) components in transitions to the nuclear excited states. The variation of cross section with energy at a constant momentum transfer,  $q_0$ , near  $q_{max}$  is given by:

$$\frac{d\sigma}{d\Omega} = \Gamma(E)[\Pi(E, \theta) \cos^2(\theta) + \xi(E, \theta) \sin^2(\theta)] \quad (1.16)$$

where  $\Gamma(E)$  is the overall energy dependence,  $\Pi(E, \theta)$  is the non spin-flip dependence, and  $\xi(E, \theta)$  is the spin-flip dependence. At constant  $q$ ,  $\theta$  must decrease as  $E$  increases, and this results in an increase in cross section with increasing energy (decreasing  $\theta$ ) for non spin-flip ( $\Delta S=0$ ) transitions, and the reverse for spin-flip ( $\Delta S=1$ ) transitions.

This dissertation presents the application of scattering and its listed advantages to the study of the  $^{15}\text{N}$  nucleus. The shell model structure of this nucleus is a very stable, filled p-shell  $^{16}\text{O}$  core with a single proton hole in the outer  $p_{\frac{1}{2}}$  shell, as shown in figure 1.2. Considering this structure, one would expect one of the lowest energy states, that formed when the proton hole in the  $p_{\frac{1}{2}}$  shell moves into the  $p_{\frac{3}{2}}$  shell, to be a very strong candidate for a pure proton transition. This is because, in the extreme shell model, it involves only the proton hole and neutrons cannot be involved. However, the work of Macauley *et. al.*[MA76], Suzuki[SU76], and Horikawa *et. al.*[HO77] showed the need for effective charge enhancements to cross section calculations for this state, which represent coupling of the shell model single hole wave functions to collective vibrations of the  $^{16}\text{O}$  core.  $\pi^\pm$  scattering data on this single hole

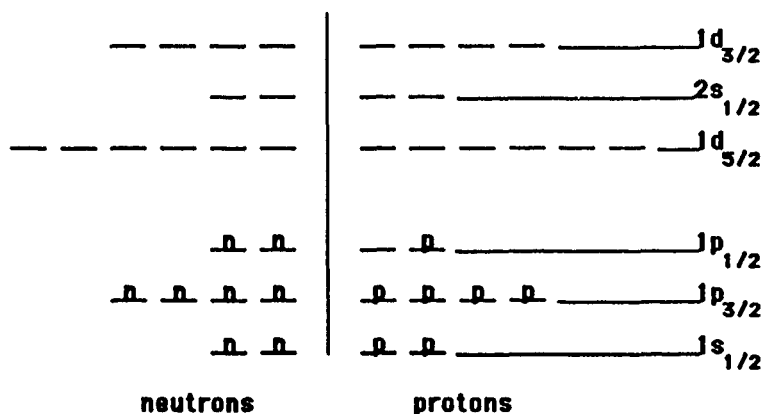


Figure 1.2:  $^{15}\text{N}$  shell model.

state, which is a  $J^\pi = \frac{3}{2}^-$  at 6.32 MeV excitation energy are presented and analyzed here.

Large  $\frac{\sigma(\pi^+)}{\sigma(\pi^-)}$  ratios have been found in other p-shell nuclei, but not where one would initially expect to see them while considering a shell model representation like figure 1.2. In  $^{13}\text{C}$ , three good neutron single particle states were studied using  $\pi$ -A scattering. In the shell model, these states are formed by moving the only valence nucleon, a  $1p_{\frac{1}{2}}$  neutron, to the  $1d_{\frac{5}{2}}$ ,  $2s_{\frac{1}{2}}$ , or  $1d_{\frac{3}{2}}$  shells. If this model were completely valid, a  $\frac{\sigma(\pi^-)}{\sigma(\pi^+)} = 9$  ratio would be expected for these states; the observed values were about 2[DE79]. The reason cited for this is that the  $^{13}\text{C}$  ground state has strong mixing between the  $1p_{\frac{3}{2}}$  and  $1p_{\frac{1}{2}}$  orbitals.  $^{15}\text{N}$ , as mentioned before, might be expected to have a large  $\frac{\sigma(\pi^+)}{\sigma(\pi^-)}$  ratio for the 6.32 MeV state, but other low lying states in  $^{15}\text{N}$  cannot be viewed as simple single particle couplings to a stable closed shell core as can be done in  $^{13}\text{C}$ , so the extreme  $\frac{\sigma(\pi^+)}{\sigma(\pi^-)}$  ratios might not be expected. It has been proposed, though, that such ratios might be seen based on coupling the excited nucleon to a core which has certain excitation due to its isospin state.



Specifically, looking at the  $^{15}\text{N}$  ground state of figure 1.2, if the  $1p_{\frac{1}{2}}$  proton is excited to the  $2s1d$  shell, the isospin of the holes left in the core ( $T_h$ ) is 1, while excitation of a  $1p_{\frac{1}{2}}$  neutron can give either  $T_h = 0$  or 1. Using this “ $T_h$  model” Oset and Strottman[OS82] predict that the lowest lying positive parity states are one-proton-particle two-proton-hole states, and that the next higher set of states will be one-neutron-particle one-neutron-one-proton-hole states, separated in energy from the first set by 4-5 MeV. With the 9:1 ratios for  $\frac{\sigma(\pi^+)}{\sigma(\pi^-)}$  and  $\frac{\sigma(\pi^-)}{\sigma(\pi^+)}$ , this model can be tested. It must be noted that even if this model is expected to be valid, mixing between p shell orbitals in the ground state and collective enhancements to the shell model wave functions may reduce the ratios.

Large  $\frac{\sigma(\pi^-)}{\sigma(\pi^+)}$  ratios have been found in  $^{13}\text{C}$  at higher energies and at large angular momentum transfer values. In fact, the largest ratio was found for a state at 9.5 MeV which has the largest angular momentum transfer value possible in single particle excitation from the p to sd shell; this is called a “stretched” state. Specifically, these transitions go from the  $1p_{\frac{3}{2}}$  to the  $1d_{\frac{5}{2}}$  shell, with spin-flip, giving a total angular momentum transfer of four, and an excited state  $J^\pi$  value of either  $\frac{7}{2}^+$  or  $\frac{9}{2}^+$ . Figure 1.3 shows schematically why this might be expected in  $^{13}\text{C}$ . There are two representations of this state in the shell model. Figure 1.3 a) shows a configuration where a proton has been excited from the  $1p_{\frac{3}{2}}$  to the  $1p_{\frac{1}{2}}$  shell, and a neutron has gone from the  $1p_{\frac{1}{2}}$  to the  $1d_{\frac{5}{2}}$  shell. Figure 1.3 b) gives the same isospin representation, but proceeds simply by the promotion of a  $1p_{\frac{3}{2}}$  neutron to the  $1d_{\frac{5}{2}}$  shell. Because of the nature of the  $\pi$ -A interaction, one step, direct interactions are expected to dominate. Therefore very little of the left configuration is expected, and the

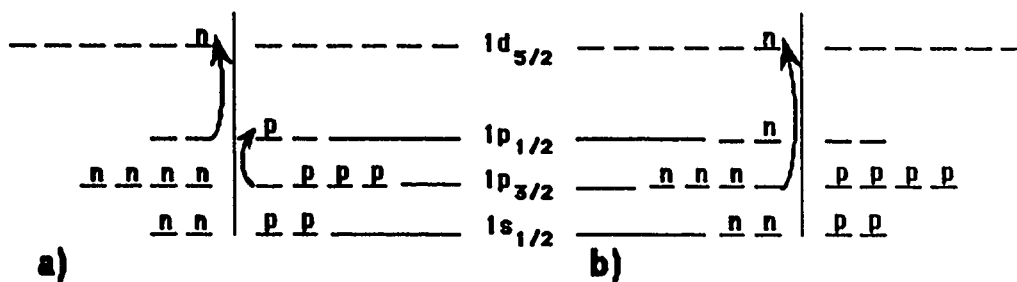
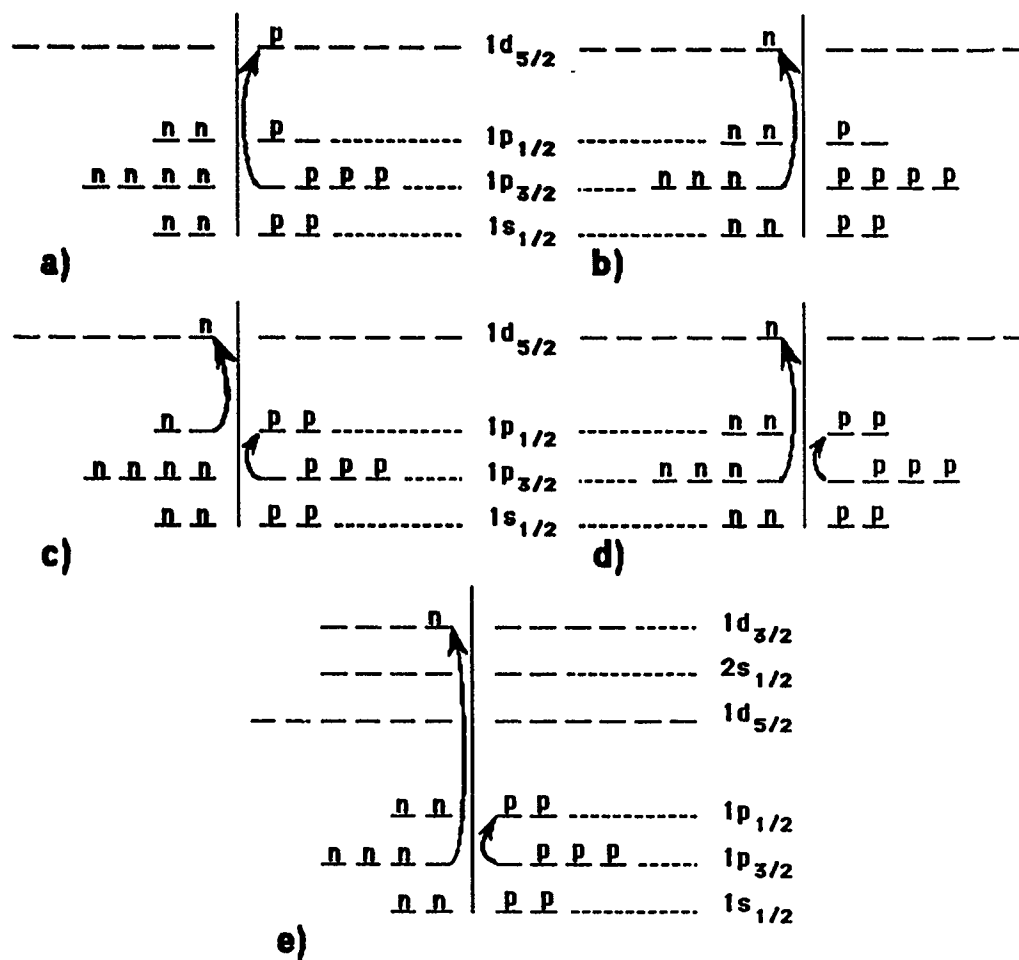


Figure 1.3:  $^{13}\text{C}$  stretched state configurations.

dominance of the right configuration results in an approximately 1:9 ratio for  $\frac{\sigma(\pi^+)}{\sigma(\pi^-)}$ .

In  $^{15}\text{N}$  a similar situation might be expected, and figures 1.4 a) through e) show the possible configurations. Figure 1.4 a) can be described in a weak coupling model as a  $1d_{5/2}$  proton coupled to the first  $2^+$  excited state of  $^{14}\text{C}$ , which has two isospin components,  $T_h = 0$  or 1, leading to the possibility of two proton dominated states here. The configurations in figures 1.4 b) through e) are based on coupling a s-d neutron to a  $^{14}\text{N}$  core excited to a  $2^+$  or  $3^+$  level. Because of the greater closed shell stability (due to the pairing interaction) of the  $^{14}\text{C}$  core as compared to the  $^{14}\text{N}$ , the  $^{14}\text{N}$  core states would be expected to lie at a higher energy. All of the  $^{14}\text{N}$  core configurations except 1.4 b) are reached by multi-step processes, and would not be expected to contain much strength. Configuration 1.4 b) would, however, be expected to produce two small (neutron dominated)  $\frac{\sigma(\pi^+)}{\sigma(\pi^-)}$  ratio states for the  $T_h = 0$  and  $T_h = 1$  portions of this configuration.

A description of the experimental apparatus and procedure used to obtain the  $^{15}\text{N}(\pi^\pm, \pi^\pm)^{15}\text{N}^*$  data is given in Chapter II. Data reduction and analysis, along with some general comments on the results, are presented in

Figure 1.4:  $^{15}\text{N}$  stretched state configurations.

Chapter III. Theoretical interpretations of the data are discussed in Chapter IV.

## Chapter 2

### Experimental Apparatus and Procedure

The data presented here are the results of an experiment performed from 7 to 16 January 1983 at the Clinton P. Anderson Meson Physics Facility (LAMPF) on Mesita de Los Alamos, Los Alamos National Laboratory, New Mexico. LAMPF is a medium energy accelerator and basic nuclear research facility, the main purpose of which is to advance the study of nuclear structure. All measurements were performed using the Energetic Pion Channel and Spectrometer, which is a good resolution ( $\sim 200$  keV) pion momentum dispersion channel and spectrometer at LAMPF. Following are general descriptions of the accelerator, and the EPICS channel, spectrometer, detectors, and electronics, and their use.

#### 2.1 Accelerator

The LAMPF accelerator produces high current beams of medium energy protons ( $H^+$ ), negative hydrogen ions ( $H^-$ ) and polarized negative hydrogen ions ( $P^-$ ). The  $H^+$  beam is used to produce the secondary beams of  $\pi^\pm$  which were used in this experiment. There are four basic portions of the accelerator: the ion sources, the 750 keV preaccelerators, the drift tube linac, and the side coupled linac. These will be discussed briefly here but more details may be found in reference [LI77].

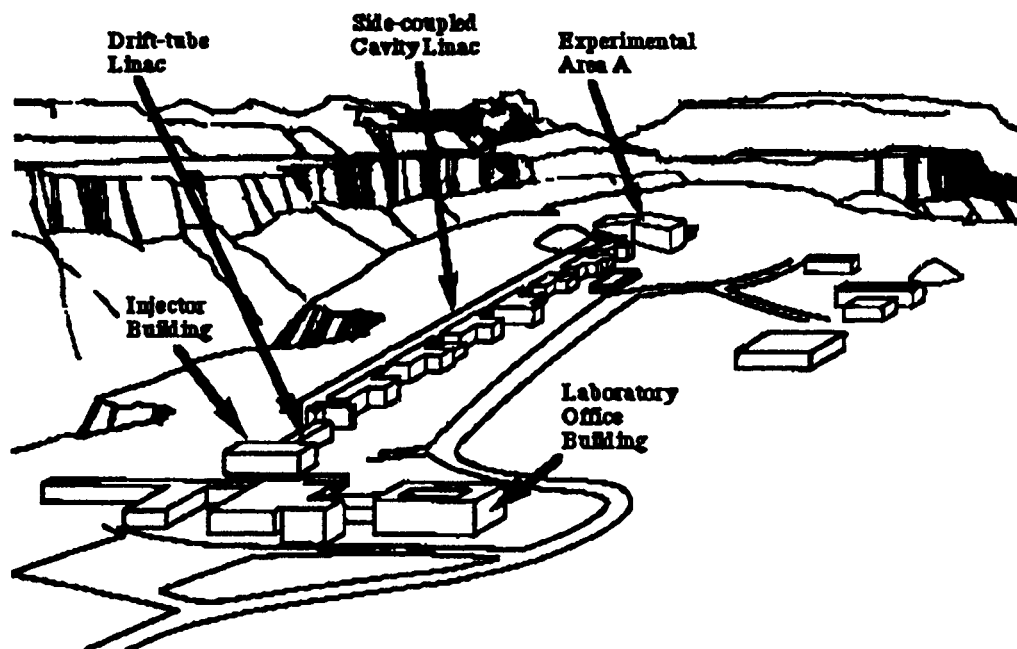


Figure 2.1: LAMPF Facility.

Three different ion sources are used to produce the three ion beams, two of which can be accelerated at any one time ( $H^+$  and  $H^-$  or  $H^+$  and  $P^-$ ). The  $H^+$  source, a Von Ardenne Duoplasmatron, strikes an arc in a 100 micron  $H_2$  atmosphere between a cathode (pulsed at 120 Hz to -135 V with a pulsewidth of  $500\mu s$ ) and an intermediate electrode. The resulting plasma is separated into positive and negative components, with the free electrons accelerated toward the the intermediate electrode and the zero potential anode aperture.  $H_2^+$  and  $H^+$  ions accelerate out through this same anode aperture because of an external extraction electrode, biased to -25kV, which produces the required field gradient.  $H^-$  and  $P^-$  sources are the same as the  $H^+$ , but with attached charge exchange and RF polarizing cells to produce the negative and polarized negative ions as necessary.

Each ion source is housed inside a separate injector terminal, all of which charge to 750 kV (+ for the  $H^+$  beam, - for the others), to give the particles their initial boost to 750 keV. The positive and negative ion sources are pulsed  $180^\circ$  out of phase, and so the  $H^+$  and  $H^-$  are timed to enter the linac portion of the accelerator on the appropriate opposite phases of the accelerating cycle. The injector terminals are raised to 750 kV by Cockcroft-Walton type high voltage electrostatic generators. The first linac portion of the accelerator is a modified Alvarez design drift tube type with quadrupole focusing inside the drift tubes. The RF sources for this portion of the accelerator run at 201.25 MHz, and the section accelerates the beam to 100 MeV. The second linac portion, and last portion of the accelerator, is a resonantly side coupled cavity linac which operates at 800 MHz and accelerates the beam to 800 MeV. At the end of the accelerator is the beam switchyard, which allows the  $H^+$  beam to continue undeflected into area A, the meson physics area, and switches the  $H^-$  or  $P^-$  beam to other areas. Figure 2.2 shows the switchyard and experimental areas.

## 2.2 EPICS

The  $H^+$  beam, directed into area A, is used to produce secondary beams of pions. One of these beams is that which is apertured into the EPICS channel. It is produced when the 800 MeV protons collide with the spinning, water cooled, cylindrical A-1 carbon target. The EPICS beam is taken off at an angle of  $35^\circ$  from the main proton beam, which trades pion beam intensity (maximum at  $0^\circ$ ) for spectrometer angular coverage, while considering the requirements of the other experimental areas in area A. The whole EPICS system

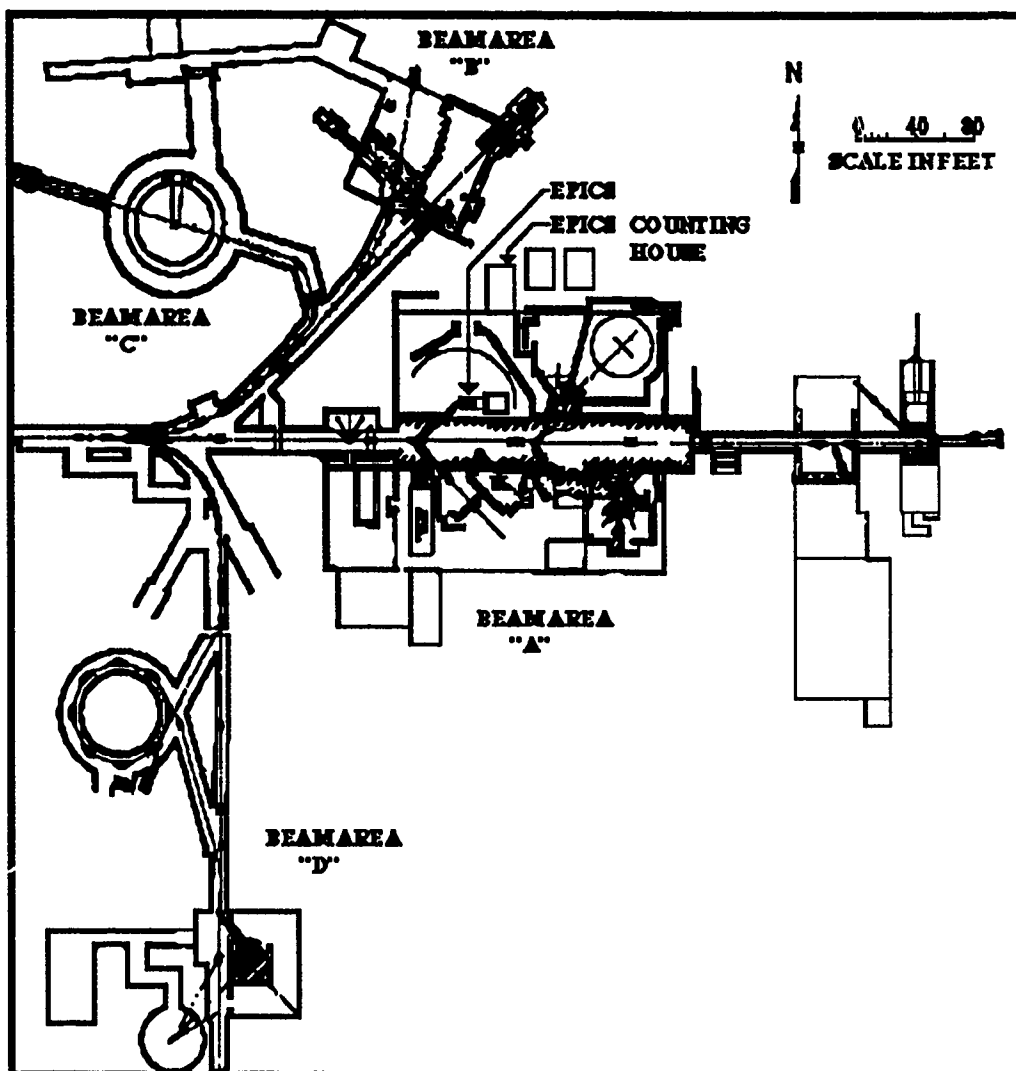


Figure 2.2: LAMPF Experimental Area and Switchyard.



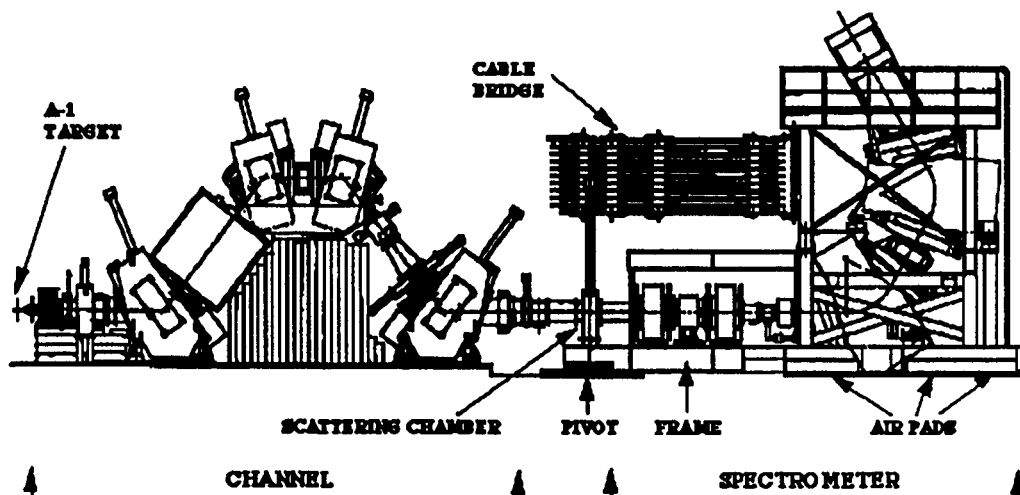


Figure 2.3: Energetic Pion Channel and Spectrometer.

consists of a momentum selecting and dispersing channel, a scattering chamber, and a spectrometer and its associated detectors, electronics, and analysis system.

### 2.2.1 EPICS Channel

The EPICS channel is described in reasonable detail in reference [TH70]. The function of the channel is to select pions of a certain charge, and of a small range of momentum values, and disperse the selected pions in the vertical direction according to their momentum values. The channel and its optics are shown in figure 2.4. This vertical dispersion (or analysis) of the beam by momentum value allows for much higher beam flux (200 times higher) than an essentially monochromatic beam would provide, while retaining the resolution of the beam, since momentum is a well known function of vertical position at the target. Momentum selection and dispersion in the channel are done by

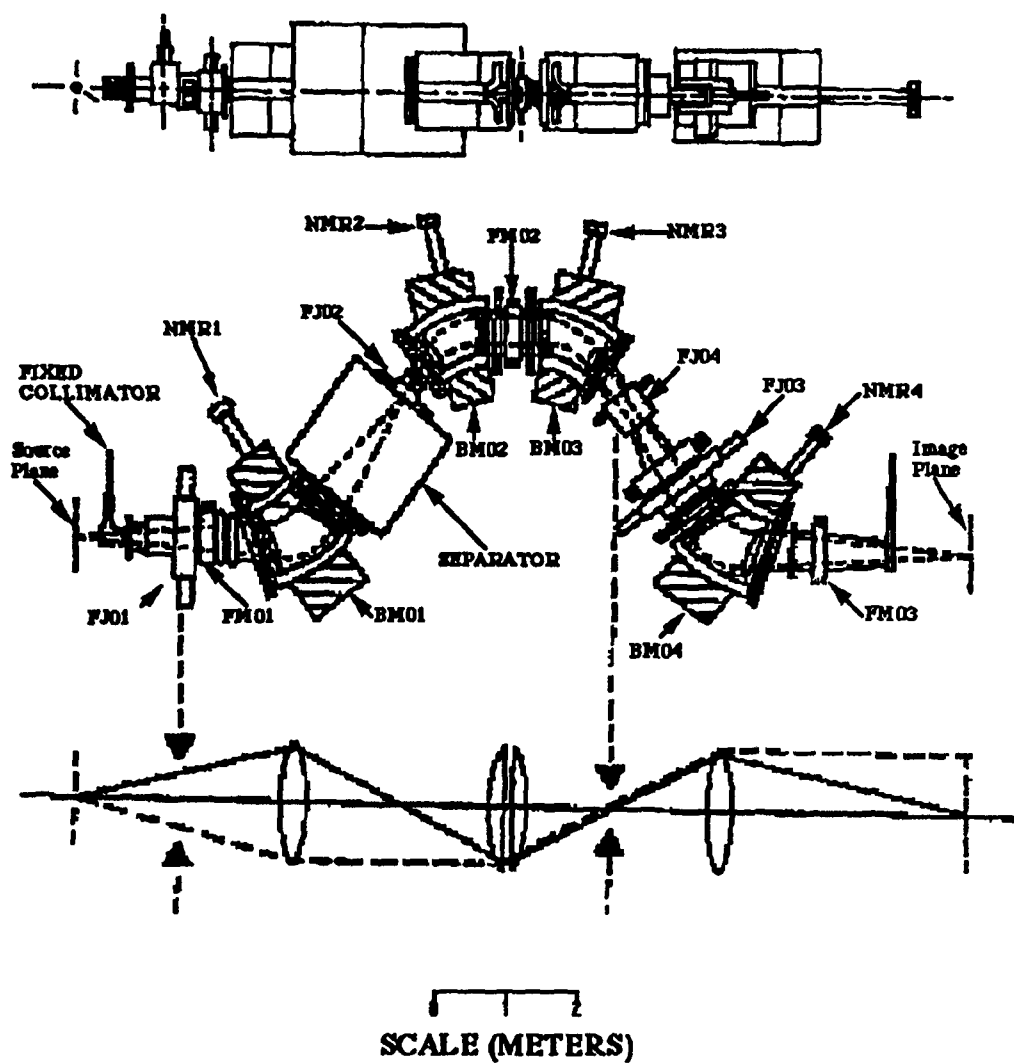


Figure 2.4: EPICS Channel and Optics.

Table 2.1: EPICS system specifications\*.

CHANNEL		SPECTROMETER	
Solid angle	3.4 msr	Solid angle	$\approx 10\text{msr}$
$\Delta p/p$	2%	$\Delta p/p$	14%
Beam size (horiz.)	8 cm	Momentum	100-750 MeV/c
Beam size (vert.)	20 cm	Flight path	$\approx 12.5\text{m}$
Beam divergence (horiz.)	$< 10\text{mrad}$	Dispersion	4 cm/%
Beam divergence (vert.)	100 mrad		
Energy	70-300 MeV		

\*Data taken from reference[LA84].

four dipole bending magnets (BM01-BM04) that focus point to point in the vertical plane, and point to parallel in the horizontal plane. Focussing (or trim) magnets (FM01-FM03) are multipole magnets which fine tune the beam in the channel. Jaws FJ01-FJ04 provide adjustments for channel output beam momentum range, intensity, and divergence. Channel output beam characteristics with all jaws fully open are given in table 2.1.

### 2.2.2 EPICS Scattering Chamber

The EPICS scattering chamber is vacuum coupled to the channel, and normally contains a target ladder system which holds approximately beam size solid targets. Since a gas target was used in this experiment, the target ladder was removed and replaced by a cylindrical cooled gas target vessel. The vessel, shown in figure 2.5, extended outside the limits of the channel output beam spot size in all directions. It was produced by the chemical deposition

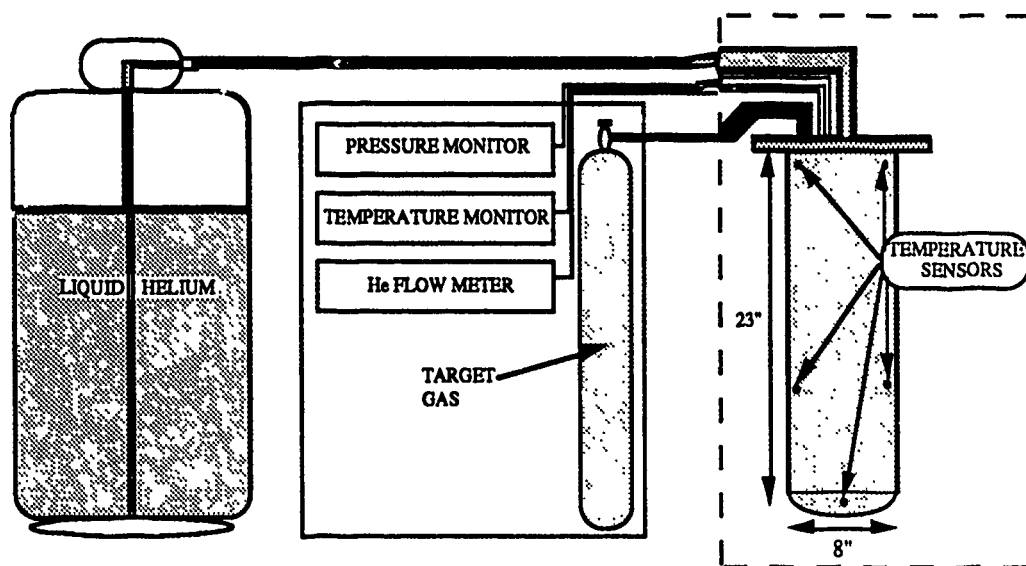


Figure 2.5: EPICS Cooled Gas Target Vessel and System.

of a 25 micron thickness of nickel from a solution of nickel-sulfamate onto a mandrel. The mandrel was subsequently etched away to leave only the vessel itself. Analysis of the vessel showed it to be 99.5% nickel, 0.5% cobalt, with negligible levels of lead and copper. Absolute gas pressure in the vessel was monitored regularly by means of an absolute pressure manometer attached to the vessel's gas input manifold. Gas temperatures in the vessel were regularly monitored, too, by means of five thermocouple temperature monitors placed in various locations from the top to the bottom of the target vessel.

### 2.2.3 EPICS Spectrometer

The EPICS Spectrometer (figure 2.6) is vacuum coupled to the scattering chamber. Because it is not dispersion matched to the channel, the first portion of the spectrometer is a quadrupole triplet which images the pion at the

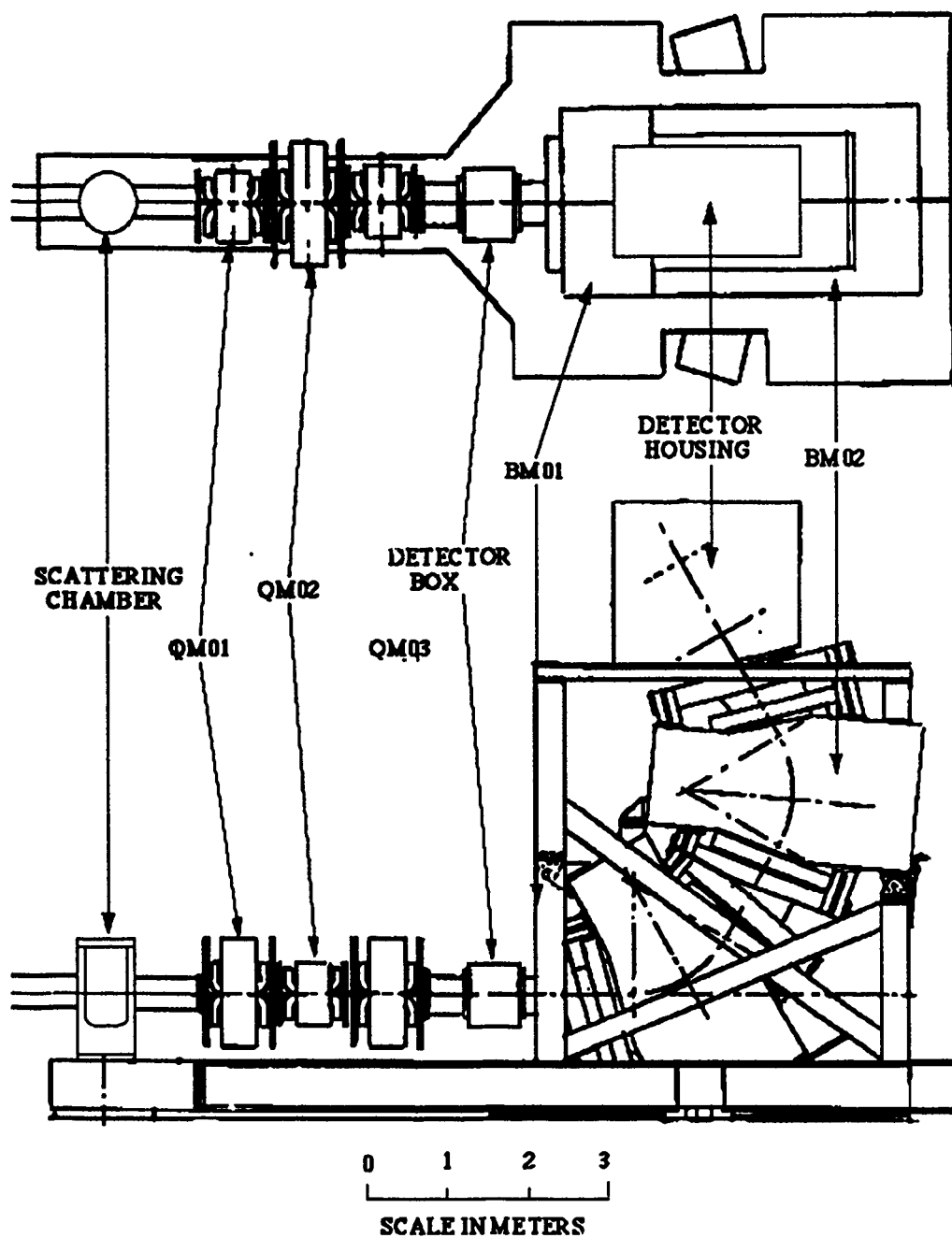


Figure 2.6: EPICS Spectrometer.

target onto a set of chambers (the front chambers). This arrangement is used to determine where (in vertical position) the pion came from, and therefore determine its incident momentum. The triplet focusses the pions, point to point, onto the wire chambers with a magnification of -1 in the vertical direction, and point to parallel in the horizontal direction, where the horizontal position at the front chamber is proportional to the scattering angle at the target. After the triplet are two 60° bending magnets, BM05 and BM06, which provide for analysis of the scattered pion. Another set of wire chambers (the rear chambers) identifies the pion's position and trajectory after analysis through these magnets. Knowing both front and rear chamber position and trajectory and the optics of BM05 and BM06 allows identification of the scattered pions scattering angle and change in momentum. EPICS spectrometer performance and acceptance specifications are shown in table 2.1.

#### **2.2.4 EPICS Detector System**

Parts of the detector system were mentioned briefly during the spectrometer description, as was necessary to a description of its function. In fact, most of the detectors are physically associated with the spectrometer, and the only ones that are not are those used in beam monitoring for the purpose of normalizing experimental runs to normalization and acceptance scan runs. These beam monitors include an ion chamber called "Beam on Target" (BOT) which is located near the A-1 target and monitors the radiation from it. The other monitors are called IC1 and 1ACM02. IC1 is another ionization chamber, located in the scattering chamber along the pion beam axis downstream from the target, which directly monitors the pion beam (and included contaminants

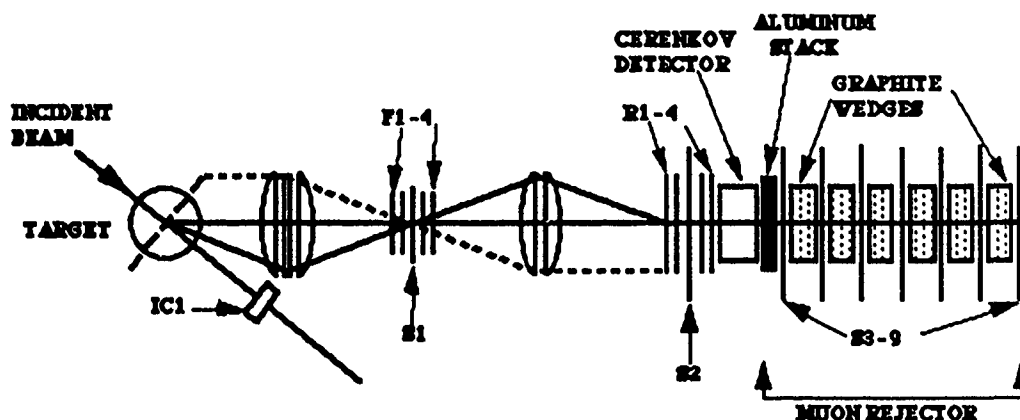


Figure 2.7: EPICS Spectrometer optics and Detector System.

of electrons, muons, and protons) incident on the target. 1ACM02 is a toroidal charge integrating coil which monitors proton beam current upstream from the A-1 target. IC1 was used as the primary normalization detector, but for the few runs where there were problems with IC1, cross normalization to BOT and 1ACM02 was used.

The spectrometer detector system is shown schematically in figure 2.7. As was described in the spectrometer section, the front and rear wire

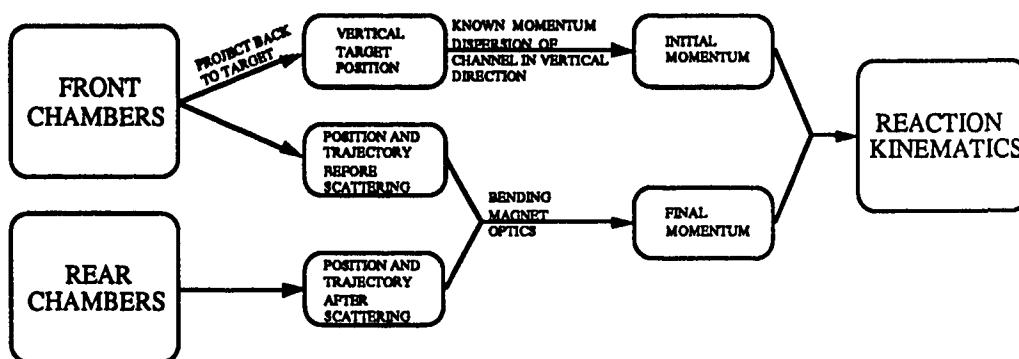


Figure 2.8: Kinematics calculation flow chart.

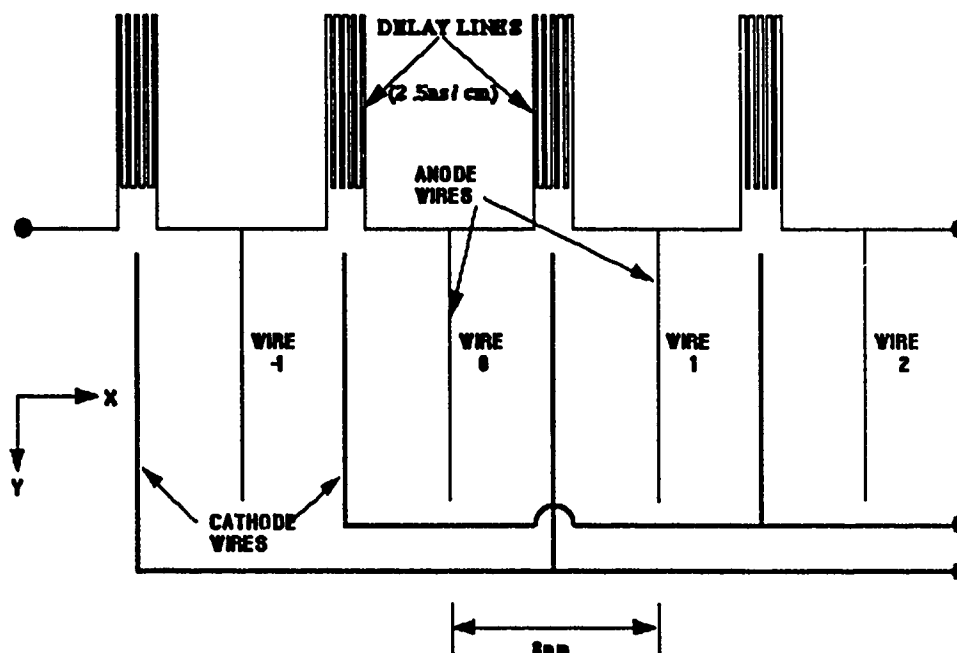


Figure 2.9: EPICS wire chamber wire plane representation.

chambers provide for calculation of reaction kinematics via the flow chart of figure 2.8. Operation of these wire chambers (or Delay-line readout drift chambers) is described in detail in references [AT81, MO82]. A basic description is given here. Figure 2.9 is a representation of one wire plane that measures position in the x direction. The anode wires of this plane are connected, at regular intervals, to a 2.5ns/cm delay line which is biased to approximately 2150V. Anode outputs are taken at each end of the delay line, converted to NIM level fast logic pulses, and are used as stops for CAMAC Time to Digital Conversion (TDC) units. The TDC's are started by the trigger coincidence logic signal of the spectrometer system, S2·S3 (S2 and S3 are scintillator detectors which will be discussed later). Since S2 and S3 are physically located downstream from the wire chambers, up to 200 meters of 50Ω coaxial cable was used to



delay the NIM fast logic pulses. Considering figure 2.9, and assuming that the cabling for both anode outputs are the same length, if wire 0 fires, the time registered on the two associated TDC's will be the same. The TDC time for the left output ( $T_l$ ) minus the time for the right output ( $T_r$ ) will be 0. So if  $T_l - T_r = 0 = T_{diff}$  for an event, it was within  $\pm 4\text{mm}$  of wire 0. In general, then

$$x = a_0 + a_1 (T_{diff}) \quad (2.1)$$

where  $x$  is the wire position,  $a_0$  is a constant offset reference position, and  $a_1$  is a constant involving the delay per unit length of the delay line.

These chambers are actually able to determine position to  $\pm 1.25\text{mm}$ , though, and this is done by using the fact that the sum of the two anode TDC signals is equal to twice the drift time of the ions in the chamber from their point of creation (the pion's position) to the anode wire, plus a constant;

$$T_l + T_r = 2T_{dr} + c \quad (2.2)$$

The constant here is easily determined, since it is just the total delay along both of the anode lines, which is obviously a constant independent of which wire was triggered. This leaves a known drift time, which can be converted to a drift distance through a calibration which only assumes uniform illumination of the 8mm wide drift cells[MO82]. The only problem left now is the decision of whether to add or subtract the drift distance from the wire position  $x$ . In this experiment, this decision was taken care of by placing another wire plane, with anode wires positioned half way between those of the first plane, directly behind the first plane. These measurements give  $x$  position at the wire chambers, and a similar setup, with anode wires at a  $90^\circ$  angle to those used

for the x measurements give y position. 10 cm downstream from the first set of wire planes in the wire chambers is an identical set of planes that give x and y positions once again, so that positions x and y are known, and trajectories  $\theta(= dx/dz)$  and  $\phi(= dy/dz)$  can be calculated.

The detectors presented so far allow for normalizations between runs and determination of kinematics for all events, but an analysis of all events wastes computer time and tape storage space. The remainder of the detectors allow us to classify the events as to whether or not they are good pion events. The first of these are scintillators S2 and S3. As was mentioned before, S2-S3 is used as a start trigger for the TDC's on the front and rear wire chambers. The actual overall hardware good event trigger which causes a set of event measurements (from all system detectors) to be written to tape is S2-S3-(F1 or F2)·(F3 or F4) (where F1-F4 are front wire chamber signals) provided the computer is not already busy. Between S2 and S3 is a slab of lucite which is used to "range out" protons before they reach S3, so that proton events will not be written to tape. Nonetheless, some protons, as well as a large number of electrons and muons, may make it through both S2 and S3. These events must then be software rejected. S2 and S3 aid in the software analysis of these events. At the lower spectrometer momenta, because of their differing masses, electrons, pions, muons, and protons can be resolved based on their velocity or time of flight between the scintillators. So, software cuts are made based on the time of flight between S2 and S3. The pulse height from a scintillator detector is, according to the energy loss equation[ME66]:

$$-\frac{dE}{dx} = a + b \left[ \ln \left( \frac{f\gamma Mc^2}{M} \right) \right]$$

$$= a + b \left[ \ln \left( \frac{fE}{M} \right) \right] \quad (2.3)$$

where  $a$ ,  $b$ , and  $f$  are constants which involve the charge of the incident particle, and  $E$  and  $M$  are the incident particle's total energy and mass, respectively. Since energy loss in matter is dependent on the charge, mass, and energy of the particle traversing it, cuts on S2 and S3 pulse heights (or the geometric mean of their pulse heights) can be used to similarly eliminate non-pion events.

At high momentum values electron, muon, and pion times of flight become unresolvable. A Čerenkov counter, located between S2 and S3, can be used to eliminate electron events, but was not used in this experiment because electrons actually only made up a small fraction of the events.

The last detector system is called the muon rejector (see figure 2.7), and is composed of a variable thickness aluminum stack between scintillators S3 and S4, and carbon wedges interspersed between scintillators S4-S9, along with S4-S9 themselves. This system works based on the fact that, because pions are lighter than muons, a pion's total energy to mass ratio for a given spectrometer momentum value is higher than a muon's, and since energy loss in matter goes as in equation 2.3, the pion loses its energy before the muon. By placing the proper amount of aluminum and carbon between S3 and one of S4-S9, it can be arranged so that only muons arrive at the scintillator of interest. Rejection of anything that makes it to that scintillator is therefore muon rejection.

### 2.2.5 Data Acquisition and Analysis System

Anode signal cables from the wire chambers are capacitively blocked to protect the electronics system from their high DC voltage, and terminated into  $100\Omega$  at the input of an amplifier-discriminator which produces fast logic pulses that are sent on to the electronics system in the EPICS counting house. Light signals from scintillators S2-S9 are optically coupled into two photomultiplier tubes each, whose signals are also cabled into the counting house. A schematic of the electronic/logic system to which these signal cables are input is presented in figure 2.10. This schematic does not include the elastic fast clear system used in this experiment, which uses the obvious correlation between crude x position in the front and rear chambers to reject 9 out of 10 elastic events. This system was used on runs with overly high elastic count rates (basically the forward angle runs) in order to get the inelastics without having to run for an unreasonable period of time. When the logic system provides a hardware trigger, a PDP 11-45 computer reads the CAMAC TDC's and Analog to Digital Converters (ADC's, used to read scalers like those from IC1 or 1ACM02). In addition to this, the computer reads various other scalers (like EVENT and  $\overline{\text{EVENT} \cdot \text{BUSY}}$ ). The scalers are indicators of the system's performance and were monitored at regular intervals by the experimenters. Interface between the CAMAC modules and the computer is provided by a Los Alamos developed Microprogrammable Branch Driver. The computer writes the event data and scalers to tape as they are received, and analyzes them only when it is not busy reading and writing them.

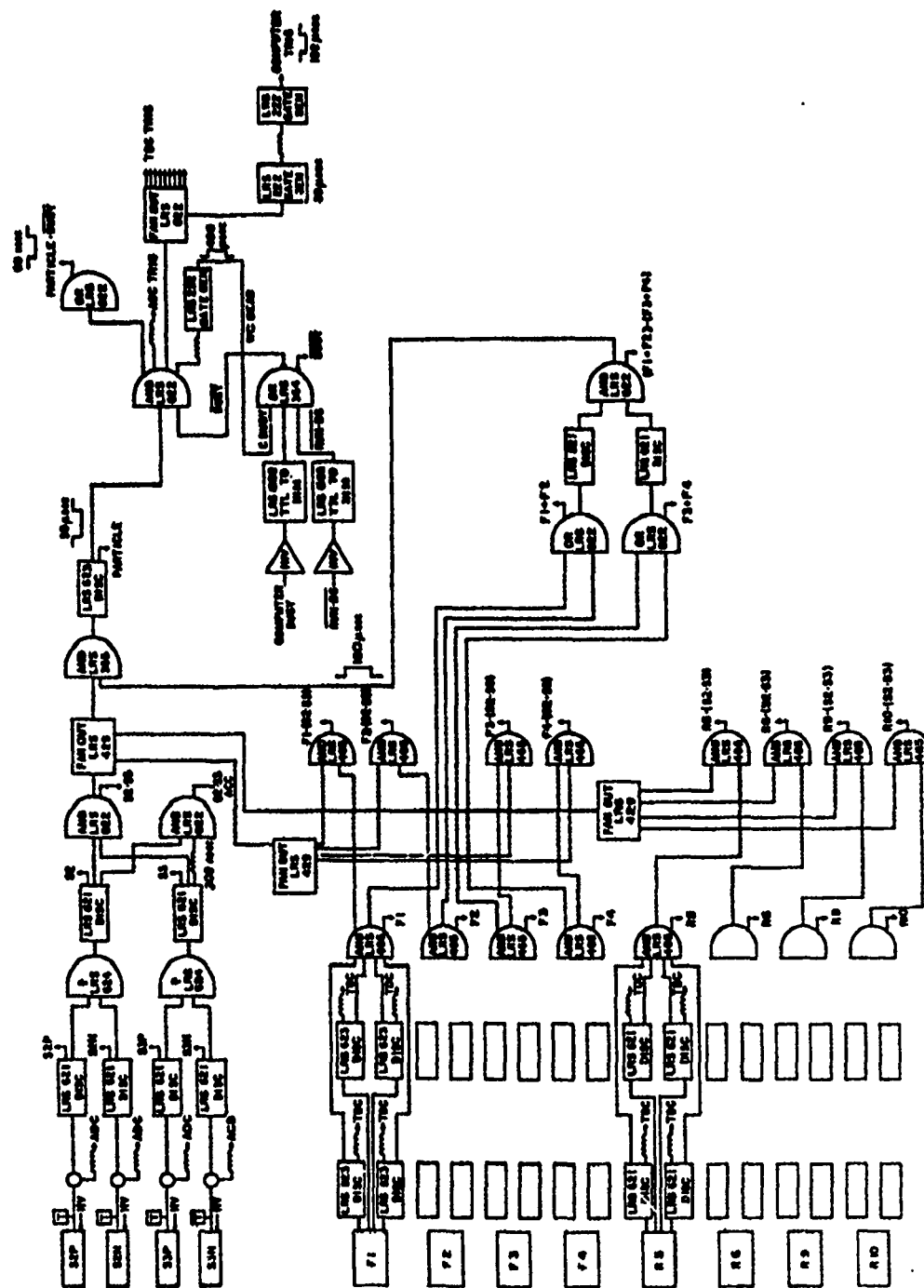


Figure 2.10: EPICS Data Acquisition Electronics/Logic System.

## 2.3 Experimental Detail

This section describes some details specific to this experiment. The target material was cooled nitrogen gas isotopically enriched to 99.7% in the isotope  $^{15}\text{N}$ . The nitrogen gas was maintained at a pressure of about 13 psia and a temperature of approximately 88 K. The gas temperature obtained was achieved through the use of a liquid helium coldfinger in conjunction with a resistive heater, both in thermal contact with the target vessel. The temperature quoted was an average of that read from the five thermocouple temperature monitors placed throughout the target vessel. Maximum variation of any thermocouple reading from the average temperature was 1.8%. Target pressure and temperature were logged every two hours. Nitrogen gas temperature and pressure were not constant throughout the experiment because the target was purged and refilled a number of times. Ratios of Pressure to Temperature ( $P/T$ ) for three different series of  $^{15}\text{N}$  data runs were  $0.1388 \pm 0.0004$ ,  $0.1466 \pm 0.0007$ ,  $0.1485 \pm 0.0003$  psia/K. The  $P/T$  ratios were used in an ideal gas law calculation, along with the beam and target geometries, to get a target thicknesses.

Yields for  $\pi^\pm$ -p elastic scattering were measured by filling the target vessel with  $\text{CH}_4$  (methane) gas. The temperature of the methane gas was approximately 138 K, giving a  $P/T$  ratio of  $0.0916 \pm 0.0010$  psia/K. Methane data were taken at  $5^\circ$  steps from  $\theta_{\text{lab}}=25^\circ$  to  $50^\circ$ , and at  $10^\circ$  steps from  $50^\circ$  to  $90^\circ$ . These measurements provided absolute normalization factors to known cross sections as well as spectrometer acceptance normalization factors which were necessary because of the spectrometer-target geometry, which caused an angle-dependent variation of effective target thickness (see figure 2.11).  $^{15}\text{N}$

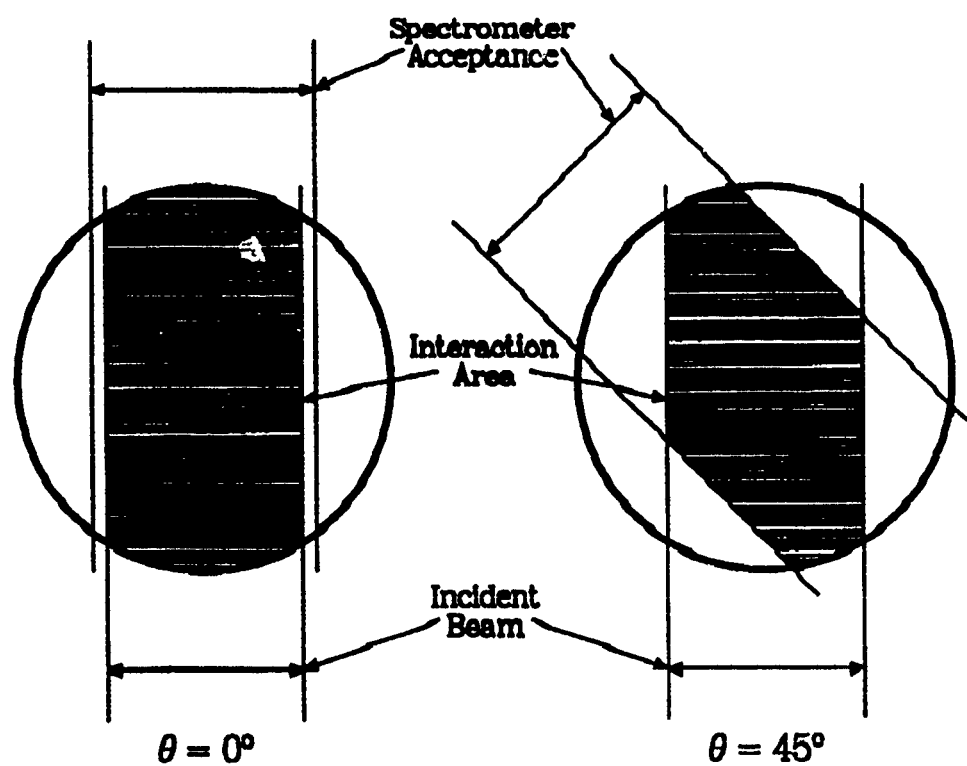


Figure 2.11: Illustration of change in effective target thickness with angle for EPICS spectrometer with cooled gas cylindrical target vessel.

data were taken for  $\pi^+$  and  $\pi^-$  at  $T_\pi = 164$  MeV for scattering angles from  $25^\circ$  to  $90^\circ$ , in increments of  $5^\circ$ . Additional data were taken for 120 MeV  $\pi^+$ , at  $\theta_{lab} = 89.9^\circ$  and  $49.8^\circ$ , and for  $T_{\pi^+} = 260$  MeV at  $\theta_{lab} = 48.8^\circ$  and  $28.5^\circ$ . These data were taken to measure the energy dependence of the excitations at constant  $q$  (momentum transfer) values.  $^{58}\text{Ni}$  contamination from the target vessel seen in the spectra were subtracted out, and the other target vessel contaminants were found to have a negligible effect on the spectra obtained.



## Chapter 3

### Data Analysis and Results

#### 3.1 Event Analysis

The objective of event analysis is to determine the scattering angle and energy loss ("missing mass") of the pion in its interaction with the nucleus. The pion's missing mass is the difference between its incoming and outgoing total energies, and is (approximately) equal to the excitation of the residual nucleus. The analysis is done by the online computer in a "may process" mode, and when event count rates are too high, the runs have to be replayed later, offline in the "must process" mode, to analyze all events. The analysis described here applies to both on and off line analysis modes.

Analysis is performed by the standard EPICS analyzer "Q"[AM79] on an event by event basis. Q contains a main analysis subroutine, PROCO6, in conjunction with a display file (EXP703.set, figure 3.1) and an experiment specific set of tests (which are in the file EXP703.tst, figures 3.2, 3.4, 3.5, and 3.8). These are used to direct PROCO6 in performance of appropriate data tests and setup of data display histograms, dotplots, and histogram storage files. PROCO6 also computes chamber and scintillator quantities (front and rear chamber positions and trajectories, for example). EXP703.tst is composed of 3 test loops, which are performed in order by PROCO6. In between test loops, PROCO6 calculates chamber and scintillator quantities, and reaction

```

; C135,315JEXP703.SET
; CYCLE 37 EXP703 N15 REPLAY
;
FILE=C135,315JEXP703.D8P
FREE ALL
H1=233,8500,11500,20; XTOT
T1=91 ; GOOD CHMRS, ANG CHK
H2=234,8000,12000,30; THTTOT
T2=91 ; GOOD CHMRS, ANG CHK
H3=235,9000,11000,20; YTOT
T3=91 ; GOOD CHMRS, ANG CHKN
H4=236,9000,11000,40; PHITOT
T4=91 ; GOOD CHMRS, ANG CHK
H5=237,9500,10500,20; THETACHK
T5=99 ; GOOD CHMRS
H6=238,9500,10500,20; PHICHECK
T6=99 ; GOOD CHMRS
H7=163,9990,12000,50; FLR(1)
T7=93; GOOD EVENT
H8=164,9990,12000,50; FLR(2)
T8=93; GOOD EVENT
H9=246,9500,13000,4; MHA55
T9=109; GOOD EVENT, -1/10
H10=246,9500,13000,4; MHA55
T10=110; PIDN, -1/10
H11=246,9500,11000,4; MHA55
T11=114; GOOD EVENT, 1/10
CLEAR ALL
; THATS ALL FOLKS

```

Figure 3.1: LAMPF Experiment 703 Data Display File, Exp703.set.

kinematics. A brief description of this analysis sequence follows. Loop 1 is performed first, and consists of tests 1 through 16 in EXP703.tst. The loop is basically a set of two windows or gates, called a box, placed around the mean energy loss in scintillators S2 and S3, and around the time of flight between S2 and S3. It is called the particle identification, or PID, box. A dot plot of S23 Time of Flight versus Energy Loss (Geometric Mean of S2 and S3) with this PID box placed on it taken during replay of the data is shown in figure 3.3. If an event falls within this box, the analyzer continues on the event by computing particle positions and trajectories ( $x_f, y_f, \theta_f, \phi_f, x_r, y_r, \theta_r$ , and  $\phi_r$ ). After these calculations, the analyzer goes to the second loop, tests 17 through 64. These tests make sure that all 16 wire planes fired, and that all wire plane events fall along a straight line trajectory. With these tests passed, the analyzer

```

761.64,64.4          ;L135,312EXP70385 TST  7-JAN-83
GAT,233,10000,12000, ;1  ;S1 DE/DX          ;EXP70384.TST
GAT,253,10000,12000, ;2  ;S2+63 DE/DX
GAT,250,10301,32000, ;3  ;CERENKOV PH SUM
S1,2,0.              ;4  ;S4 MUON
S1,2,1.              ;5  ;S5
S1,2,2.              ;6  ;S6
S1,2,3.              ;7  ;S7
S1,2,4.              ;8  ;S8
S1,2,5.              ;9  ;S9
GAT,3,1,32000.       ;10 ;FAST CLEAR (1/10)
BOX,1.               ;11 ;BOX 1 --> PID
AND,2,3,4.           ;12 ;GOOD DE/DX
IOR,6,7,8,9.         ;13 ;BIT TEST
AND,11,8.            ;14 ;PID=CERENKOV
AND,11,-5.           ;15 ;PID=NOT(CERENKOV)
IOR,1,-1.            ;16 ;LOOP1 COUNTER
END

```

Figure 3.2: Experiment 703 Test File, Exp703.tst, loop 1.

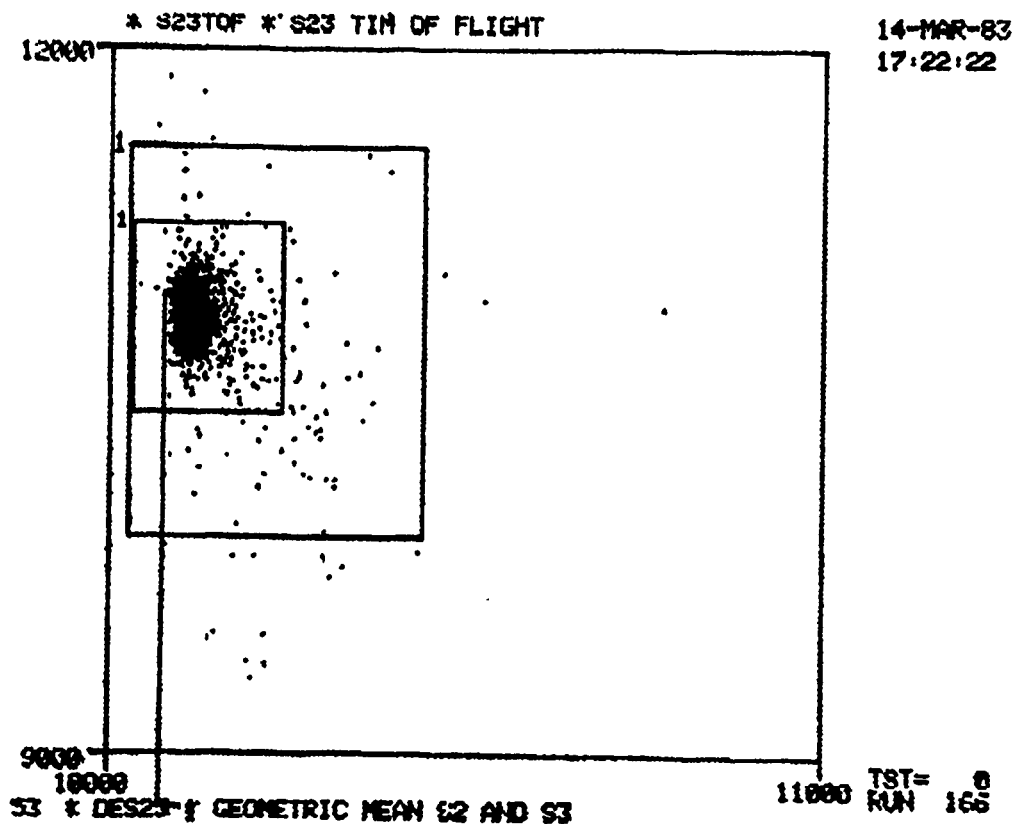


Figure 3.3: Experiment 703 Data Replay Particle Identification (PID) Box.

```

GAT,141,9990,10140, :17 :1A DRAFTMA :CHAMBER LOOP 2
GAT,142,9990,10140, :18 :2A DRAFTMA
GAT,143,9990,10140, :19 :3A DRAFTMA
GAT,144,9990,10140, :20 :4A DRAFTMA
GAT,145,9990,10140, :21 :5A DRAFTMA
GAT,146,9990,10140, :22 :6A DRAFTMA
GAT,149,9990,10140, :23 :9A DRAFTMA
GAT,150,9990,10140, :24 :10A DRAFTMA
GAT,201,9990,10140, :25 :1C DRAFTMC
GAT,202,9990,10140, :26 :2C DRAFTMC
GAT,203,9990,10140, :27 :3C DRAFTMC
GAT,204,9990,10140, :28 :4C DRAFTMC
GAT,205,9990,10140, :29 :5C DRAFTMC
GAT,206,9990,10140, :30 :6C DRAFTMC
GAT,209,9990,10140, :31 :9C DRAFTMC
GAT,210,9990,10140, :32 :10C DRAFTMC
GAT,147,9990,9982, :33 :7 CHECKSUM (QUAD)
GAT,148,9940,10002, :34 :8 CHECKSUM (QUAD)
GAT,272,9990,10020, :35 :FRONT DRF DIF PLANE A
GAT,273,9990,10020, :36 :FRONT DRF DIF PLANE C
GAT,274,9990,10020, :37 :REAR DRF DIF PLANE A
GAT,275,9990,10020, :38 :REAR DRF DIF PLANE C
AND,11,35,36,37,38, :39 :DRF DIF TST*PID --> DRF
AND,11,25,26,27,28, :40 :FRONT C CHAMBERS OK*PID
AND,11,17,18,19,20, :41 :FRONT A CHAMBERS OK*PID
AND,11,29,30,31,32, :42 :REAR C CHAMBERS OK*PID
AND,11,21,22,23,24, :43 :REAR A CHAMBERS OK*PID
AND,40,41, :44 :FRONT OK
AND,42,43, :45 :REAR OK
AND,44,45, :46 :ALL EXCEPT QUAD OK*PID --> CHMRS
IOR,33,34, :47 :QUAD OK
AND,46,47, :48 :ALL OK
AND,10,19,20,40,45, :49 :FALLBUT 1A CHAMBER EFFICIENCY TEST
AND,17,19,20,40,45, :50 :FALLBUT 2A
AND,17,10,20,40,45, :51 :FALLBUT 3A
AND,17,18,19,40,45, :52 :FALLBUT 4A
AND,22,23,24,42,44, :53 :FALLBUT 5A
AND,21,23,24,42,44, :54 :FALLBUT 6A
AND,21,23,24,42,44, :55 :FALLBUT 9A
AND,21,22,23,42,44, :56 :FALLBUT 10A
AND,26,27,28,41,45, :57 :FALLBUT 1C
AND,25,27,28,41,45, :58 :FALLBUT 2C
AND,25,26,28,41,45, :59 :FALLBUT 3C
AND,25,26,27,41,45, :60 :FALLBUT 4C
AND,30,31,32,43,44, :61 :FALLBUT 5C
AND,29,31,32,43,44, :62 :FALLBUT 6C
AND,29,30,32,43,44, :63 :FALLBUT 9C
AND,29,30,31,43,44, :64 :FALLBUT 10C
END

```

Figure 3.4: Experiment 703 Test File, Exp703.tst, loop 2.

calculates the kinematical quantities  $x_{tgt}, y_{tgt}, \theta_{tgt}, \phi_{tgt}$ , incident momentum, scattered momentum, and scattering angle, and from incident and scattered momentum and scattering angle, pion missing mass. Event position and trajectory angles at the target are found by tracing backwards using the position and trajectory angles of the event at the front chambers through the known quadrupole optics. For example, since the magnification of the quadrupoles in the x direction is -1,

$$x_{tgt} = -x_f \quad (3.1)$$

There are aberrations in the quadrupole fields, and the actual calculations made on these quantities involve fourth order polynomials. Incident event momentum ( $P_i$ ) is calculated according to the following equation from  $x_{tgt}$  using the known central momentum of the channel ( $P_c$ , determined by the channel magnetic field settings), and the dispersion of the channel,  $D_c = \left(\frac{\Delta P}{P}\right)_c$ , see table 2.1.

$$P_i = P_c + x_{tgt} \left(\frac{P_c}{D_c}\right) \quad (3.2)$$

Where  $x_{tgt}$  is the positive or negative event position on the target relative to the position of channel central momentum on the target. Scattered event momentum ( $P_{sc}$ ) is determined by an analysis using the spectrometer dipole magnets and is therefore a function of positions before and after analysis by the magnets, and of the spectrometer central momentum and dispersion. Since the magnification of the dipoles in the x direction is -1, the position at the rear chambers should be the negative of that at the front for events which have the same scattered momentum as the spectrometer's central momentum:

$$x_r = -x_f \quad (3.3)$$

or more generally for all momenta:

$$\begin{aligned}x_r &= -x_f + \frac{D_{sp}(P_{sc} - P_{sp})}{P_{sp}} \\P_{sc} &= \left( \frac{x_r + x_f}{D_{sp}} \right) P_{sp} + P_{sp} \\P_{sc} &= \delta_{sp} P_{sp} + P_{sp}\end{aligned}\tag{3.4}$$

to first order, where  $D_{sp} = \left( \frac{\Delta P}{P} \right)_{sp}$ , and  $\delta_{sp} = (x_{fr} + x_r) / D_{sp}$ . Finally, scattering angle,  $\theta_{sc}$  is given by

$$\theta_{sc} = \theta_{sp} + \theta_{tgt}\tag{3.5}$$

where  $\theta_{sp}$  is the spectrometer angle.

Kinematic calculations are done by the subroutine CALKIN, using  $P_i$ ,  $P_{sc}$ , and  $\theta_{sc}$  to calculate incident and scattered event total energies  $E_i$  and  $E_{sc}$ , respectively, and residual nucleus momentum using conservation of energy and momentum. Finally, CALKIN uses conservation of energy in the form of the following equation:

$$E_i + M_n c^2 = E_{sc} + \left[ (P_{nc})^2 + (Q + M_n c^2)^2 \right]^{\frac{1}{2}}\tag{3.6}$$

where  $M_n$  is the mass of the target nucleus,  $P_n$  is the momentum of the residual nucleus, to obtain a value for  $Q$ , the nuclear excitation energy:

$$Q = \left[ (QE_i - E_{sc} + M_n c^2)^2 - (P_{nc})^2 \right]^{\frac{1}{2}} - M_n c^2.\tag{3.7}$$

$Q$  is also called the missing mass because it is approximately equal to the energy lost by, or mass missing from, the scattered particle, for target nuclei much more massive than the particle.

After the analyzer determines missing mass, it returns to loop three in the test file. This loop, called background rejection, places cuts on the events

```

GAT,233,9000,11000,      :65      :XTGT      :BACKGROUND REJECTION LOOP 3
GAT,234,9000,11000,      :66      :THTTGT
GAT,235,9000,10500,      :67      :YTGT
GAT,236,9550,10450,      :68      :PHITGT
GAT,237,9900,10100,      :69      :THTCHK
GAT,238,9900,10100,      :70      :PHICLK
GAT,163,9990,11400,      :71      :FLR1 CUT
GAT,166,9990,11400,      :72      :FLR2 CUT
GAT,221,9095,10740,      :73      :XFRONT PHASE SPACE CUTS
GAT,222,9137,10951,      :74      :THETA FRONT
BOX,2,                    :75      :BOX 2
BOX,3,                    :76      :BOX 3
BOX,4,                    :77      :BOX 4
BOX,5,                    :78      :BOX 5
BOX,6,                    :79      :BOX 6
IGAT,6,                   :80      :GATE 6 ==> ELASTIC PEAK
IGATE,1,                  :81      :TARGET CUTS
IGATE,2,                  :82      :TOF ELECTRON
IGATE,3,                  :83      :TOF MUON
IGATE,4,                  :84      :TOF PION
IGATE,5,                  :85      :CHER ELECTRON
AND,73,74,75,76,         :86      :PHASE SPACE CUTS-FRONT
AND,69,70,80,            :87      :THETACHECK*PHICHECK*GATES
AND,39,46,               :88      :GOOD CHBRS
AND,71,72,               :89      :FLANGE CUTS
AND,88,65,66,67,68,     :90      :TARGET TESTS*GOOD CHBRS ==> (TGT)
AND,88,69,70,            :91      :THTCHK,PHICLK,GOOD CHBRS==>ANG CHK
AND,39,46,               :92      :GOOD CHBRS, AGAIN
AND,90,91,               :93      :TGT*ANG CHK ==> (GOOD EVENT)
AND,80,80,               :94      :ELASTIC, GOOD CHBRS
AND,80,93,               :95      :ELASTIC, GOOD EVENT
AND,84,80,               :96      :GOOD CHBRS*PION TOF
END

```

Figure 3.5: Experiment 703 Test File, Exp703.tst, loop 3.

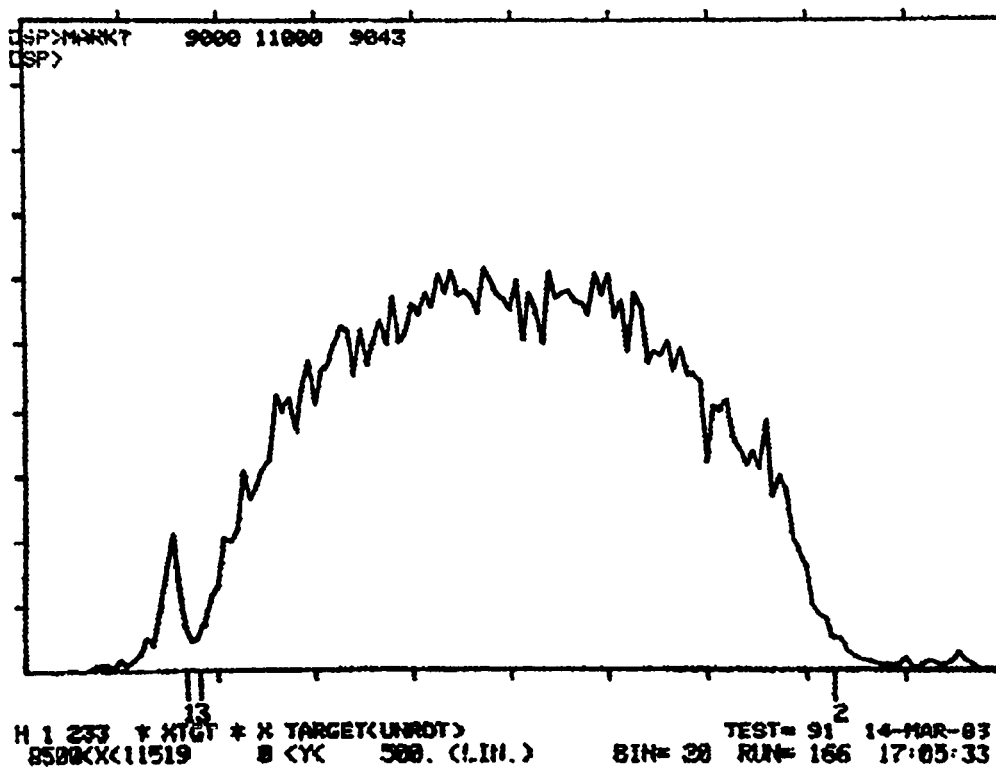


Figure 3.6: Experiment 703  $X_{tgt}$  Histogram.

analyzed to this point based on their  $x_{tgt}$ ,  $y_{tgt}$ ,  $\theta_{tgt}$ ,  $\phi_{tgt}$ ,  $\theta_{check}$ , and  $\phi_{check}$  values. As before, the “tgt” subscripted values are position and trajectory values at the target after scattering.  $\theta_{check}$  and  $\phi_{check}$  are difference angles between  $\theta$  and  $\phi$  measured at the front chambers and  $\theta$  and  $\phi$  calculated at the front chambers from measurements at the rear chambers. The main purpose of cuts on  $\theta_{check}$  and  $\phi_{check}$  is to get rid of events where pions decay into muons between the front and rear chambers. Examples of histograms used to place these cuts are shown in figures 3.6 and 3.7. The last loop in exp703.tst produces the data for histograms with the various cuts or tests applied.



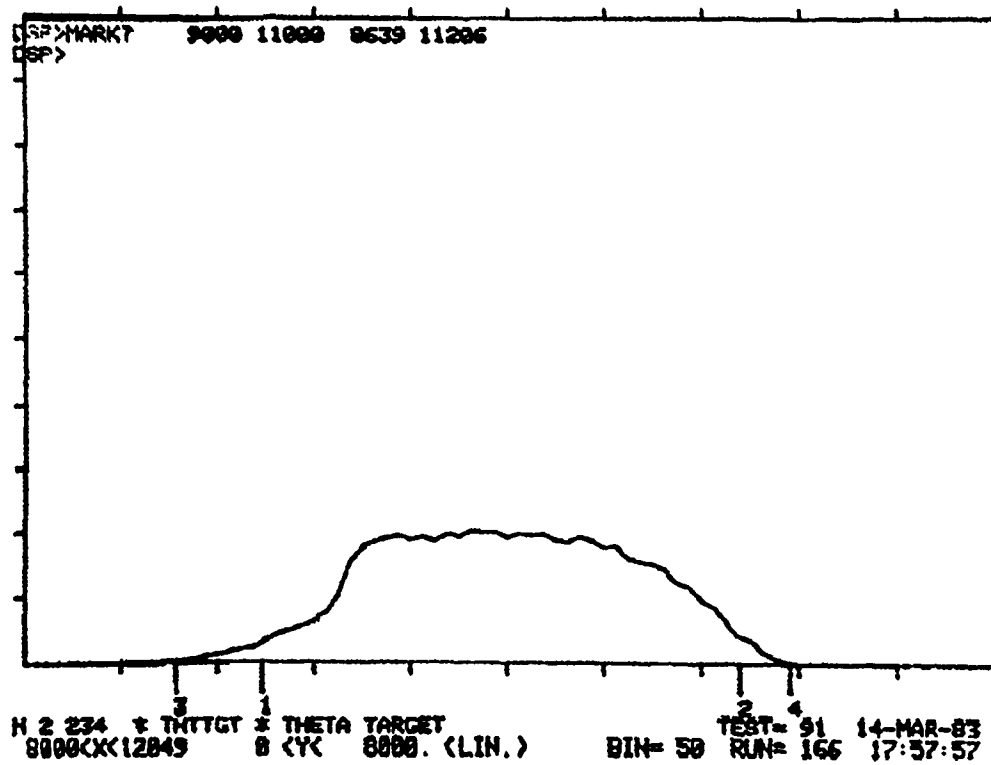


Figure 3.7: Experiment 703  $\theta_{tgt}$  Histogram.

```

CAT,236,9739,9913,      ;97      ; -1.0 DEG
CAT,236,9913,10067,     ;98      ;  0.0 DEG
CAT,236,10067,10261,    ;99      ;  1.0 DEG
81,2,1,                  ;100     ; MUON(IN FP 95 REJ)
CAT,1,1,-1,             ;101     ; SPARE
CAT,1,1,-1,             ;102     ; SPARE
CAT,1,1,-1,             ;103     ; SPARE
CAT,1,1,-1,             ;104     ; SPARE
AND,93,89,               ;105     ; GOOD EVNT,FLNGECUTS
AND,105,-100,           ;106     ; GOOD EVENT,PION(MU REJ)
AND,105,82,             ;107     ; GOOD EVENT ELEC
AND,105,100,            ;108     ; GOOD EVENT MUON (MU REJ)
AND,105,-10,            ;109     ; GOOD EVENT,-1/10
AND,106,-10,            ;110     ; PION GOOD EVENT,-1/10
AND,-1,1,               ;111     ; SPARE
AND,1,-1,               ;112     ; SPARE
AND,1,-1,               ;113     ; SPARE
AND,105,10,             ;114     ; GOOD EV,1/10
AND,114,-100,           ;115     ; GOOD EV,1/10,-MU REJ
AND,114,100,            ;116     ; GOOD EV,1/0,MU REJ
AND,106,70,             ;117     ; PION EVENT AND BOX3
AND,106,79,             ;118     ; PION EVENT AND BOX4
AND,39,46,89,           ;119     ; GOOD CHMBRS,FLSNCE
AND,1,-1,               ;120     ; SPARE
AND,105,97,             ;121     ; GOOD EV,-1 DEG
AND,105,90,             ;122     ; GOOD EV, 0 DEG
AND,105,99,             ;123     ; GOOD EV, 1 DEG
AND,106,80,             ;124     ; PION EVENT AND GATE 6
AND,91,-100,            ;125     ; ANG CHK*-MUON,
AND,81,46,              ;126     ; GATE FOR CH CAL
IOR,1,-1,               ;127     ; LOOP 4 COUNTER (UNDOOPEE WERE DONE)
END
FIN

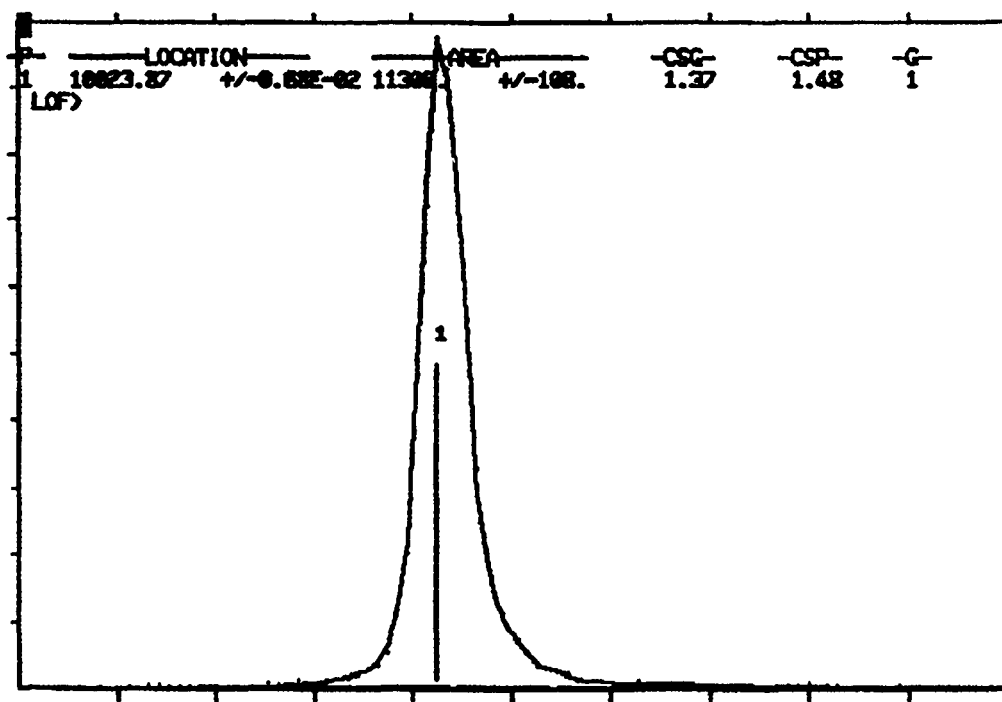
```

Figure 3.8: Experiment 703 Test File, Exp703.tst, loop 4.

## 3.2 Data Reduction

The important results of replay are missing mass histograms or spectra like the one shown in figures 3.9 through 3.11. These histograms consist of events which have passed all test loops, and which have specifically passed test 106 or 110 depending on whether the fast elastic veto was used. The histograms display number of events versus energy, and the events are binned into energy groups 40 keV wide. The spectrometer has an angular acceptance of  $\pm 1.5^\circ$  and all the events from a single angle setting were summed into one histogram, so the events are effectively binned into  $3^\circ$  wide angle groups around the nominal angular value. Number of counts in (or area of) the peaks observed in these histograms is used, along with various normalizations, momentum acceptance values, known absolute normalization cross sections, etc. to get differential cross sections for excitation of the states.

Peak areas for the elastics were obtained using the program LOAF [SM78], while those for the inelastics were extracted using the program FIT [MO]. LOAF used a simple experimental reference peak shape to fit the data, while FIT used an experimental line shape folded with a gaussian of width which varied with excitation energy, but not with angle, for its reference shape. Fits were performed separately on three regions of the spectra: the elastic (0 MeV) region, the region from 4.5 to 14.2 MeV, and that from 14.2 to 19.5 MeV. The regions were fit in order of increasing energy, with iterative variation of overall energy offset and peak energies, widths, and areas to obtain the best overall fit. A linear background was used for all fits. Example fits for the three regions are shown in figures 3.9 through 3.11.



DE0 246 \* GEXACT \* MISSING MASS FROM CALKIN TEST=110 1-AUG-83  
 98520X(10247 0.4Y< 1990. (LIN.) BIN= 4 RUN= 145 20:27:56

Figure 3.9: The 60° 164 MeV  $\pi^+$  Spectrum, along with a fit to its 0 MeV region.

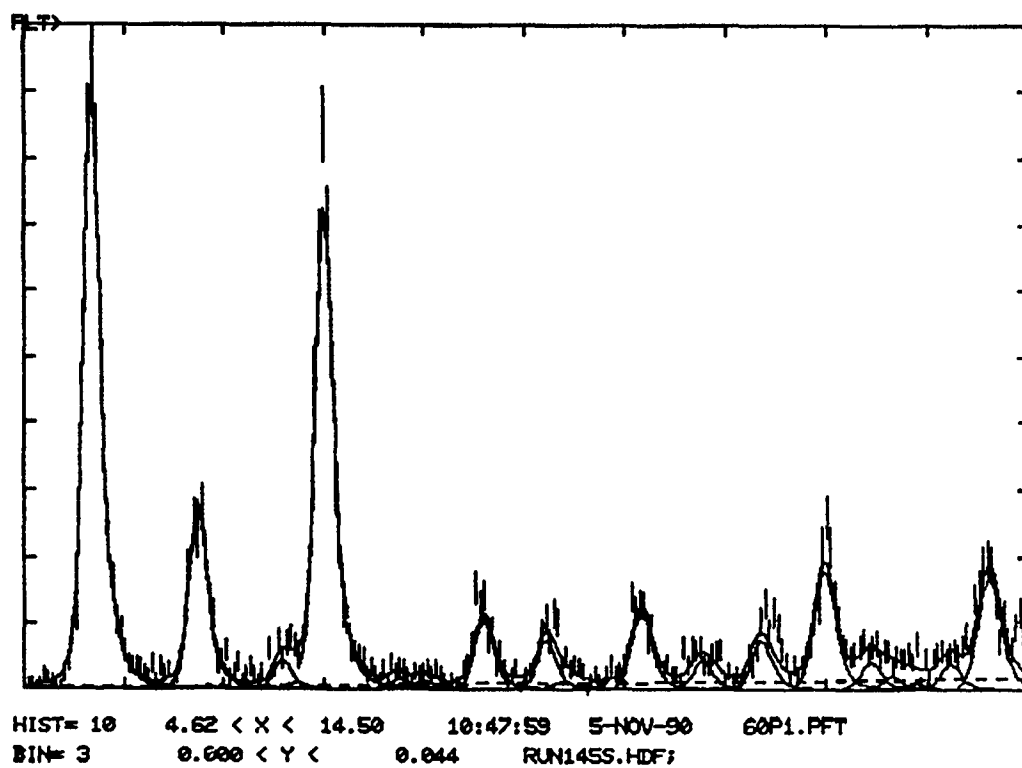


Figure 3.10: The 60° 164 MeV  $\pi^+$  Spectrum, along with a fit to its 4.5-14.2 MeV region.

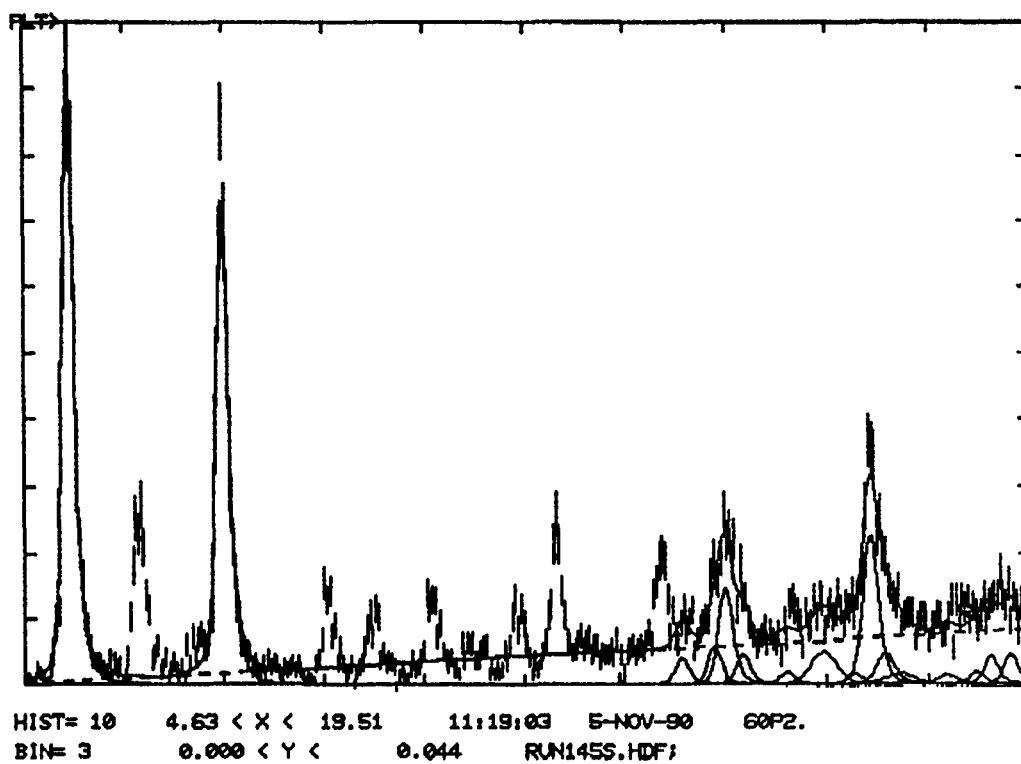


Figure 3.11: The 60° 164 MeV  $\pi^+$  Spectrum, along with a fit to its 14.2-19.5 MeV region.

Peak areas along with various correction factors are used to get a yield for scattering at the various angles:

$$\text{YIELD} = \text{AREA} / (\text{CLT} \cdot \text{DREFF} \cdot \text{CHEFF} \cdot \text{LE} \cdot \text{SF}) \quad (3.8)$$

where CLT is the percent computer live time, or percent of the time the computer is not busy, and able to read in events. DREFF is a correction for drift efficiency and corrects for those events which didn't pass drift difference tests but did fire all chambers. CHEFF corrects for imperfect chamber efficiency, and is a product of the efficiency of the 16 wire planes:

$$\text{CHEFF} = \prod_{i=1}^{16} \left[ \frac{\text{All planes OK}}{\text{All but plane } i \text{ OK}} \right] \quad (3.9)$$

LE is a loop per event correction and is basically a measure of what fraction of the written events were analyzed. Since all of this data was replayed in a "must process" mode, the LE was 1.0. Finally, SF is a survival fraction factor which corrects for the fact that a certain percent (based on pion energy) of the pions decay inside the spectrometer after scattering:

$$\text{SF} = \exp\left(\frac{-L \cdot M}{p \cdot \tau}\right) \quad (3.10)$$

where L is the path length through the spectrometer, M is the pion's rest mass, p is the relativistic momentum, and  $\tau$  is its mean lifetime.

To find the differential cross section,  $\frac{d\sigma}{d\Omega}$ , for excitation to the states seen in the spectra, define the cross section,  $\sigma$ , as the probability that the excitation will occur given a certain flux of pions and a certain target thickness such that:

$$N = \sigma \ln \quad (3.11)$$

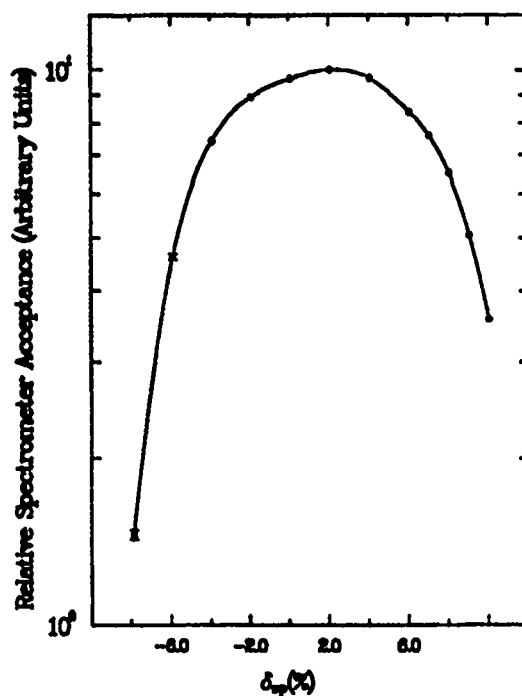


Figure 3.12: Epics spectrometer  $\delta$ -scan.

where  $N$  is the number of excitation events,  $I$  is the incident pion beam flux, and  $n$  is the number of target nuclei per unit area. Simple division of cross section by the solid angle of the spectrometer and multiplication by the lab to center of mass Jacobian,  $G$ , gives differential cross section in the center of mass:

$$\frac{d\sigma}{d\Omega_{cm}} = \frac{N}{I n} \cdot \frac{G}{\Delta\Omega} \quad (3.12)$$

In this experiment, the factors  $\Delta\Omega$ ,  $I$ , and  $n$  are not known absolutely. The design solid angle of the spectrometer is 10 msr, but the exact value is a function of where on the spectrometer focal plane (the rear chambers) the event hits, or equivalently, it is a function of  $\delta_{sp}$  (see equation 3.4). Because of this the yield as a function of  $\delta_{sp}$  was measured for one of the states near a flat part of its



angular distribution by varying the spectrometer fields to place the state at various positions on the focal plane and therefore at various  $\delta_{sp}$  values. A plot of this " $\delta$ -scan" is shown in figure 3.12.

The ion chambers (IC1 and BOT) and proton beam integrating current loop (1ACM02) give quantities which are proportional to  $I$ , the pion beam current incident on the target. The proportionality is energy dependent, though, because the percent of the beam accepted by the channel that is actually pions is energy dependent. IC1 is multiplied by a correction factor, FPI, which is an energy dependent beam pion fraction factor, to get an energy independent value proportional to  $I$ . This allows for scattering at various energies, so that excitation functions at constant momentum transfer can be determined.

Delta scans and pion correction fractions allow removal of focal plane position and energy dependences, but they still do not provide for absolute knowledge of  $\Delta\Omega$  and  $I$ . Because of this, and the fact that  $n$  is not known absolutely (it is a function of scattering angle for the cooled gas target - see figure 2.11) the yield of a reaction for which the differential cross section is well known must be measured and used for an absolute normalization. 164 MeV  $\pi^\pm$  scattering from methane gas at angles from  $25^\circ$  to  $50^\circ$  in  $5^\circ$  steps, and from  $60^\circ$  to  $90^\circ$  in  $10^\circ$  steps provided this. Comparison of these measured  $\pi^\pm$ -p yields to those calculated using the pion-nucleon phase shifts of Rowe, Saloman, and Landau[RO78] provides the absolute normalization factor  $N_{abs}$  used in calculation of absolute differential cross section:

$$\frac{d\sigma}{d\Omega_{cm}} = \frac{Yield \cdot G \cdot N_{abs}}{I_{rel} \cdot n_{rel} \cdot \Delta\Omega_{rel}} \quad (3.13)$$

where values subscripted "rel" are experimental data values relative to the CH<sub>4</sub> normalization data values.

The data presented here include only statistical and fitting errors calculated by the fitting programs. Additional errors that should be included are in correction factors, peak fitting, and absolute normalization. Correction factor errors include  $\pm 3\%$  each for survival fraction uncertainty due to uncertainty in path length through the spectrometer, uncertainty in chamber efficiency measurements, and uncertainty in beam monitoring. Statistical errors in measurement of the acceptance scan were no greater than 2%. Errors in fitting the CH<sub>4</sub> normalization data were no greater than 2.5%, but there was a difference in peak fitting method which introduced an additional error of 2.5%. The hydrogen elastic yields were obtained by simple determination of the area of the peak minus the background. Actual experimental yields were obtained by fitting an experimental lineshape on top of the background to the peak. This leads to a total estimated normalization error of 3.5%. Adding correction factor, statistical acceptance scan, and normalization errors in quadrature gives a total error, in addition to the statistical experimental peak fitting errors, of 7%. Uncertainty in the relative normalization between  $\pi^+$  and  $\pi^-$ , which is composed of all but the acceptance scan, normalization run peak fitting, and survival fraction errors (which are the same for  $\pi^+$  and  $\pi^-$ ), is 5.5%.

### 3.3 Data

This section includes a presentation of the data as well as some general comments on it. A more detailed comparison of the theory with the data follows

in chapter IV. The  $^{15}\text{N}(\pi^{\pm}, \pi^{\pm'})^{15}\text{N}^*$  data, in the form of angle dependent cross sections, is presented graphically in appendix A, and is tabulated in appendix B. The elastic distributions show the strongly forward peaked, highly diffractive pattern characteristic of scattering from a black disk or optical potential. This suggests the suitability of the optical potential to a description of the nuclear potential. Figure 3.13 shows normalized spectra taken at a spectrometer angle of  $70^\circ$  using both  $\pi^{\pm}$ . It also shows the difference spectrum between the  $\pi^+$  and  $\pi^-$  runs. Large peaks in the difference spectrum indicate asymmetries in the neutron/proton nature of the state at the energy of the difference peak. These asymmetries appear at about 5.3, 6.3, 7.6, 10.7, 12.5, and 17.2 MeV. They might be expected in light of extreme shell model descriptions of the low lying states as one particle two hole positive parity states, or, for the negative parity state at 6.32 MeV, as a simple single hole state. However, it is obvious that such an extreme shell model description is not adequate since, for example, the 6.32 MeV single hole state should be completely proton dominated if it were. This is because the extreme shell model represents this state as a  $p_{3/2}$  proton moving to fill the  $p_{1/2}$  proton hole and leaving a  $p_{3/2}$  hole behind. From the  $\pi^{\pm}$  spectra and the  $\frac{\sigma(\pi^+)}{\sigma(\pi^-)}$  cross section ratios (table 3.1), it is obvious that this does not occur, since, with the dominance of the  $\Delta(3,3)$  resonance, the  $\frac{\sigma(\pi^+)}{\sigma(\pi^-)}$  ratio should be 9. This is explained in a model which includes collective enhancements to the shell model transitions. At energies above about 10 MeV, more collective nature should be present, since the excitation energy is above the average binding energy per nucleon of approximately 8 MeV. Single particle (neutron or proton)  $^{15}\text{N}$  excited states above this energy should be less likely because concentration of this excitation energy on a single particle should cause

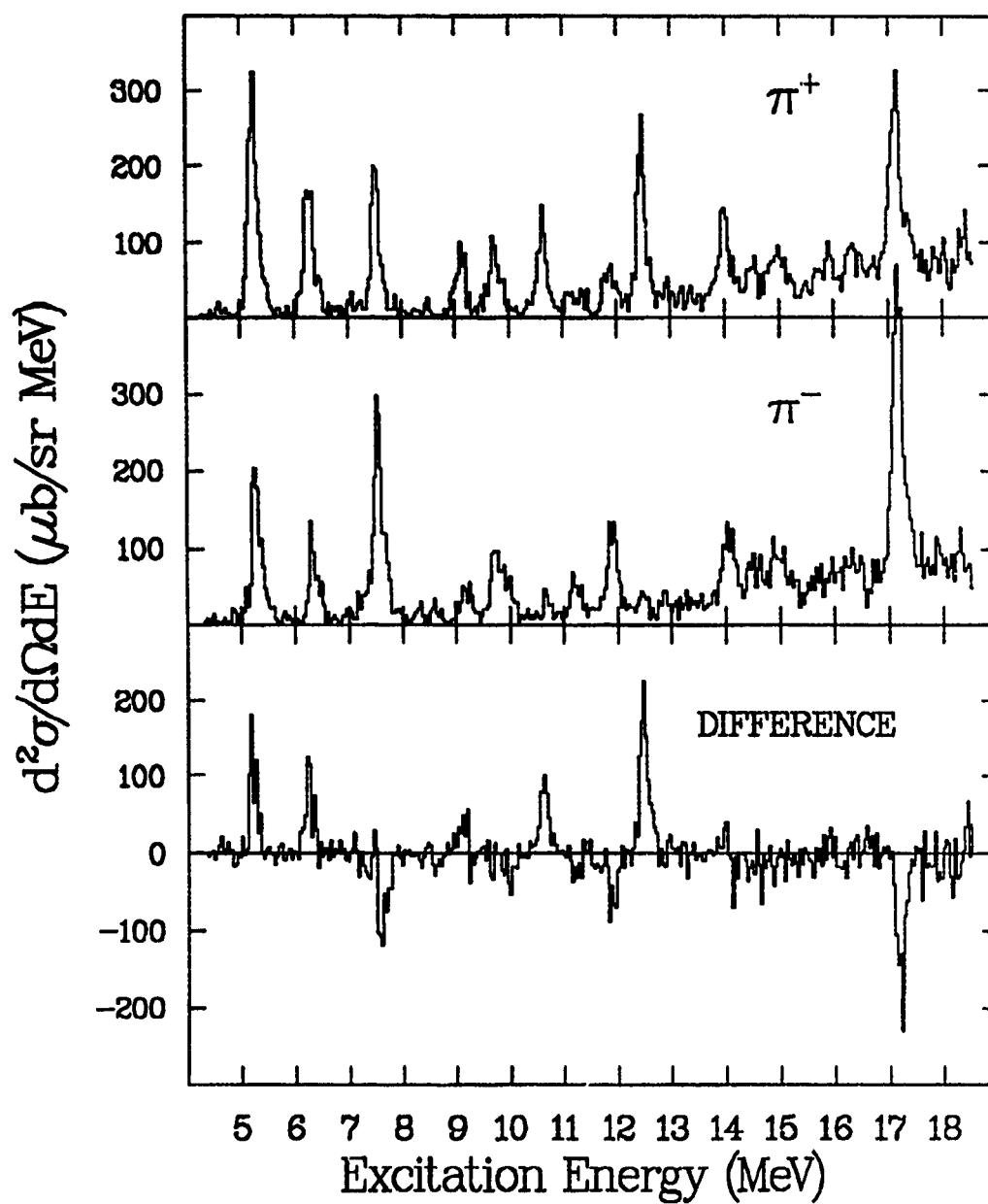


Figure 3.13:  $70^\circ$   $\pi^+$  and  $\pi^-$  spectra, along with the difference spectrum between the  $\pi^\pm$  runs.

Table 3.1: Weighted average experimental  $\frac{\sigma(\pi^+)}{\sigma(\pi^-)}$  cross section ratios.

Energy(MeV)	5.27	6.32	7.16	7.30	7.57	8.31	8.57
Ratio( $\frac{\sigma(\pi^+)}{\sigma(\pi^-)}$ )	1.15	1.78	0.68	1.01	0.62	1.41	1.87
Energy(MeV)	9.15	9.76	9.9	10.7	11.3	11.9	12.5
Ratio( $\frac{\sigma(\pi^+)}{\sigma(\pi^-)}$ )	1.73	0.89	0.43	7.05	1.47	0.74	2.57
Energy(MeV)	12.9	13.1	14.1	14.4	14.6	15.0	16.5
Ratio( $\frac{\sigma(\pi^+)}{\sigma(\pi^-)}$ )	1.24	1.67	0.94	0.98	1.03	0.99	1.49
Energy(MeV)	16.9	17.2	17.6	18.3	18.7	18.9	
Ratio( $\frac{\sigma(\pi^+)}{\sigma(\pi^-)}$ )	1.15	0.79	0.85	1.03	1.25	1.25	

it to become unbound. Figure 3.13 and table 3.1 show that there are only about 4 significant  $\frac{\sigma(\pi^+)}{\sigma(\pi^-)}$  ratios above 10 MeV, out of 17 states identified. One state at the lower end of this excitation range has large ( $\approx 9:1$ )  $\frac{\sigma(\pi^\pm)}{\sigma(\pi^\mp)}$  ratios, and it is reasonable that it would be found here. Large  $\frac{\sigma(\pi^\pm)}{\sigma(\pi^\mp)}$  ratios also appear at 12.5, 14.1 and 17.2 MeV, but as might be expected considering their higher excitation energy, the states seem to be more collectively enhanced and have smaller, though significant,  $\frac{\sigma(\pi^\pm)}{\sigma(\pi^\mp)}$  ratios.

These higher lying one-particle-two-hole states were described in the introduction as stretched or spin-flip states in the extreme shell model. (See figures 1.4 a) and b).) It was also pointed out that these states could be identified by the shape of their constant momentum transfer excitation functions. These excitation functions for the states identified as having spin-flip transitions, and those for the other states, are presented and discussed in chapter four. The spin-flip states are also high energy states ( $>10$  MeV) which have large  $\frac{\sigma(\pi^+)}{\sigma(\pi^-)}$  ratios, as should be the case.

Another artifact of the stretched nature of these states is their angu-

lar distributions. They have the greatest angular momentum transfer they can with excitation of the  $p_{\frac{3}{2}}$  particle to the  $p_{\frac{5}{2}}$  shell,  $\Delta J=4$ . The slowly varying, almost flat shape of the angular distributions for the states at 10.7, 12.5, 14.1, and 17.2 MeV, as compared to the other angular distributions, is characteristic of  $\Delta J=4$  transitions. The other transitions have more forward peaked, diffractive angular distributions, characteristic of lower angular momentum transfer values.

## Chapter 4

### Theoretical Interpretations of the Data

Pion-nucleus ( $\pi$ -A) scattering can be related to  $\pi$ -nucleon ( $\pi$ -N) scattering through the impulse approximation. In the Distorted Wave Impulse Approximation (DWIA) the assumption is that the amplitude for scattering between the pions and the nucleons in the nucleus is the same as that for free  $\pi$ -N scattering, and that the effects of the nucleon being bound in the nucleus are purely kinematical. Details of the DWIA analysis have been explored in depth elsewhere (for example, see reference [KI84]). Basically, though, the  $\pi$ -A multiple scattering amplitude,  $T_A$ , can be related to the individual  $\pi$ -N optical potentials by[FR53]:

$$T_A = V_A + \frac{V_A T_A}{E - H_A - K_\pi + i\epsilon} = \sum_{i=1}^A v_i' + \sum_{i=1}^A \frac{v_i' T_A}{E - H_A - K_\pi + i\epsilon} \quad (4.1)$$

Where  $E$  is the collision energy in the  $\pi$ -A center of mass system,  $H_A$  is the nuclear hamiltonian for the  $A$  nucleons, and the  $v_i$ 's are the bound  $\pi$ -N optical potential operators. The impulse approximation involves replacing these potential operators for nucleons bound in the nucleus with the well known potential operators for pion scattering from free nucleons.

As was mentioned before, the feature of the  $\pi$ -N interaction which dominates at the experimental pion energy of 164 MeV, is the  $\ell=1$ ,  $\Delta_{3/2,3/2}$  (1232 MeV) resonance[KO69]. In particular, the introduction showed that at

this energy the the pion is sensitive to the isospin nature of its target, and so a study of the  $\pi^\pm$  charge dependence on the cross sections gives clues to the neutron/proton nature of the transitions.

## 4.1 Theoretical Models for Elastic Scattering

Two different DWIA computer codes were used in analysis of the elastic scattering data. One of these, PIPIT[EI76B,FRA], describes the scattering through the solution of a relativistic Lippman-Schwinger equation:

$$T'(k, k'; k_0) = U(k, k') + \int \frac{T'(k, k''; k_0)U(k'', k')}{E(k_0) - E_\pi(k'') - E_A(k'') + i\epsilon} d^3k'' \quad (4.2)$$

which is in a momentum space formulation. Because of this momentum space formulation, PIPIT allows for easy inclusion of nonlocal operators (and so nonlocal potentials, i.e. for the spin-orbit interaction, etc.), as compared to coordinate space representations. A standard momentum space optical potential:

$$U(k', k) = \frac{A-1}{A} \{ \rho_p(q)t_{\pi p}(k', k; k_0) + \rho_n(q)t_{\pi n}(k', k; k_0) \} \quad (4.3)$$

developed according to the formalism of Kerman, McManus, and Thaler [KE59] was used. The off-shell T-matrix of equation 4.2 is obtained from an on-shell matrix generated from the on-shell phase shifts presented in table 4.1. These phase shifts are essentially equivalent to those of Rowe, Saloman, and Landau[RO78]. Damping of the off-shell T-matrix was achieved using a model which includes gaussian functions for the separable potentials which make up the off shell factors ( $\sigma_{ij}^\ell(\kappa', \kappa)$ ). These factors have the form:

$$\sigma_{ij}^\ell(\kappa', \kappa) = \frac{g_{ij}^\ell(\kappa')g_{ij}^\ell(\kappa)}{g_{ij}^\ell(\kappa_0)^2} \quad (4.4)$$



Table 4.1: Phase shifts\*  $\delta_\ell$  used in PIPIT calculations.

$E_{cm}$ (MeV)	$S_{31}$	$P_{31}$	$P_{33}$	$S_{11}$	$P_{11}$	$P_{13}$
1186	-10.6	-3.2	38.3	8.9	-0.9	-1.0
1195	-11.4	-3.6	46.6	9.0	-0.5	-1.3
1202	-12.1	-3.9	53.6	9.0	-0.2	-1.4

\*The phase shifts presented here are those which cover the range of center of mass energies that are 23, 18, and 28 MeV below that of our experiment (1212 MeV), corresponding respectively to the energy shifted overall analysis performed here, and to the two variations of this energy shift shown in figures 4.3 and 4.5.

where

$$g_{ij}^\ell(\kappa) = \kappa^\ell e^{-a_\ell \kappa^2} \quad (4.5)$$

are the gaussian functions, and where the  $\kappa$ 's are the pion momenta in the  $\pi$ -N cm frame,  $I$ ,  $\ell$ , and  $j$  are the  $\pi$ -N system isospin, orbital angular momentum, and total angular momentum, respectively, and the  $a_\ell$ 's are the gaussian damping factors. The labels of these two factors in the fortran code are DAMP1 for  $a_0$  and DAMP2 for  $a_1$ , for the  $\ell = 0$  (s-wave) and  $\ell = 1$  (p-wave) components of the transition, respectively. Further, a three-parameter Fermi (3pF) nuclear density distribution was initially used in these calculations, with the parameters being the 3pF nuclear charge density parameters presented in [DE87]. Later, more accurate point proton and neutron nuclear matter densities unfolded for the finite size of the nucleons[FRB] were included because of their more accurate description of the nuclear matter density distribution. Calculations presented here are those made with these point densities. The differential elastic cross section is calculated by squaring

the scattering amplitude in the normal manner:

$$d\sigma/d\omega = |f(\theta)|^2 \quad (4.6)$$

where

$$f(\theta) = f_c(\theta) + f_A(\theta) \quad (4.7)$$

and  $f_c(\theta)$  is the overall  $\pi$ -nucleus coulomb amplitude, and

$$f_A(\theta) = (1/2ik_0) \sum_{\ell=0}^{\text{LPIMAX}-1} (2\ell+1)e^{2i\sigma_\ell}(S_\ell-1)P_\ell(\cos\theta). \quad (4.8)$$

Here  $\sigma_\ell$  is the point charge coulomb phase shift, LPIMAX is the number of  $\pi$ -A partial waves used, and

$$S_\ell = e^{2i\bar{\delta}_\ell} = e^{-2i\bar{\delta}_\ell^I} e^{2i\bar{\delta}_\ell^R} = \bar{\eta}_\ell e^{2i\bar{\delta}_\ell^R} \quad (4.9)$$

where  $\eta_\ell$  represents the phase shifts for the imaginary or absorptive portion of the scattering (which at 164 MeV is essentially nonexistent, so that  $\eta_\ell = 1$ ), and the  $\bar{\delta}_\ell^R$  are the real parts of the phase shifts. The overlining simply indicates that the phase shifts are from coulomb matched transition matrices, such that

$$\bar{\delta}_\ell = \frac{1}{2} \tan^{-1} \left( \frac{-2\rho \bar{T}_\ell^R}{1 + 2\rho \bar{T}_\ell^I} \right) \quad (4.10)$$

in radians, where  $\rho$  is a phase space factor. The T-matrices used here are just those generated in equations 4.2-4.4, and as indicated, are coulomb matched.

The other pion elastic scattering code used here was DWPI [EI74], [EI76A]. DWPI is a coordinate space code which solves the Klein-Gordon equation:

$$E^2 - (pc)^2 = (mc^2)^2 \quad (4.11)$$

where  $E$  is the total energy,  $m_0$  is the pion rest mass, and  $p$  is the momentum operator,  $\vec{p} = i\hbar\vec{\nabla}$ . These calculations used a standard Kisslinger optical potential[KI55]:

$$V_n^\pm(r) = (k_\pi^2 b_0^\pm \rho(r) - b_1^\pm \vec{\nabla} \rho(r) \cdot \vec{\nabla}) \quad (4.12)$$

where  $k_\pi$  is the pion momentum,  $\rho(r)$  is the radial dependence of the nuclear matter density distribution, and the complex constants  $b_0$  and  $b_1$  are determined according to the equations[AU67]:

$$b_0^+ = F(E_\pi, E_N) \left\{ (A - Z) \frac{\alpha_{33}^0 + 2\alpha_{11}^0}{3} + Z\alpha_{31}^0 \right\} A^{-1} \quad (4.13)$$

$$b_1^+ = F(E_\pi, E_N) \left\{ (A - Z) \frac{2\alpha_{33}^1 + \alpha_{31}^1 + 4\alpha_{13}^1 + 2\alpha_{11}^1}{3} + Z(2\alpha_{33}^1 + \alpha_{31}^1) \right\} \quad (4.14)$$

where  $F(E_\pi, E_N)$  is the kinematic factor relating the free  $\pi$ -N phase shifts to those for the bound nucleons,

$$\alpha_{2T,2J}^L = \exp(i\delta_{2T,2J}^L) \sin \delta_{2T,2J}^L$$

and

$$(A - Z) \rightarrow Z \text{ and } Z \rightarrow (A - Z) \text{ for } b_0^- \text{ and } b_1^-$$

since the potentials differ for  $\pi^+$  and  $\pi^-$ . The phase shifts  $\delta_{2T,2J}^L$  used here are those of Rowe, Saloman, and Landau[RO78], and the nuclear matter density was again a 3pF distribution with parameters taken from [DE87], initially. The calculations presented here, though, used a 3pF density distribution with parameters adjusted to reproduce the unfolded point density distribution used in the PIPIT calculation. This adjustment was accomplished by using the portion of PIPIT which calculates the nuclear density

from the 3pF distribution, and adjusting the parameters until the 3pF distribution matched the point distribution. Finally, both elastic calculations employed a phenomenologically motivated energy shift which caused the  $\pi$ -N interaction to be evaluated at an energy of 20 to 30 MeV below that of the incident pions. Cottingham and Holtkamp have shown[CO80] that such an energy shift systematically improves DWPI's description of experimental angular distributions for target nuclei from  $^{12}\text{C}$  to  $^{208}\text{Pb}$ . This energy shift has also been found to improve PIPIT calculations. The underlying physical feature which is thought to produce this effect is the Fermi momentum of the struck nucleon.

## 4.2 Theoretical Models for Inelastic Scattering

In the analysis of the inelastic data, two different DWIA codes were used, ARPIN and DWPI. ARPIN[FRA,LE80] (Argonne Pion Inelastic Code) is a momentum space DWIA code that uses microscopic transition densities. The  $\pi$ -N off-shell transition matrix (T-matrix) is generated by PIPIT. This T-matrix along with initial and final wave functions and their associated transition densities are input to ARPIN, which then calculates the differential cross sections. The shell model calculations which produced these wave functions and transition densities were performed by D. John Millener, and were essentially the same as those performed in [MI75].

DWPI was used for both elastic and inelastic calculations, and macroscopic transition densities were used for the inelastic transitions. In this macroscopic treatment, the radius parameter in the density distribution

used is made a function of angle:

$$c = c_0 \left( 1 + \sum_{\lambda\mu} \alpha_{\lambda\mu} Y_{\lambda\mu}(\hat{r}) \right) \quad (4.15)$$

Here,  $\alpha_{\lambda\mu}$  is a linear combination of creation and annihilation operators  $b_{\lambda\mu}$  and  $b_{\lambda\mu}^\dagger$ , which create/destroy a nuclear excitation phonon of angular momentum  $\lambda$  and projection  $\mu$ .

$$\alpha_{\lambda\mu} = \beta_\lambda \hat{\lambda}^{-1} [b_{\lambda\mu} + (-)^\mu b_{\lambda-\mu}^\dagger] \quad (4.16)$$

With this deformed radius parameter substituted into the 3pF density distribution, the program continues on to calculate the nuclear excitation. This nuclear excitation is generated by the portion of the optical potential calculated from the deformed part of the nuclear density distribution. The calculations presented here were actually done with DWFIT, which is DWPI modified by R. Eisenstein to use separate deformation parameters,  $\beta_p$  and  $\beta_n$  for the individual proton and neutron contributions to the density distribution and optical potential, and also linked by S. J. Seestrom to the optimization code MINUIT[JA89], for optimization of the fit of the calculated to the experimental cross section by variation of the parameters  $\beta_p$  and  $\beta_n$ .

Both macroscopic and microscopic calculations were used here for a number of reasons. A comparison of microscopic calculations to experimental cross sections is important because the microscopic model involves detailed nuclear structure calculations and this comparison provides feedback on our knowledge of this structure. On the other hand, some states are found to be enhanced: they are stronger than predicted by microscopic calculations.

This is explained by the macroscopic (or collective) effective charge enhancements to the microscopic transitions just covered. A completely macroscopic calculation like DWPI may also be used to predict angular distributions for very strong, collectively enhanced states. Finally, DWPI calculates excitation transition strengths, which allows a comparison of neutron and proton transition strengths and indicates the neutron/proton nature of the transitions and allows an almost direct comparison of proton strengths to  $\gamma$ -ray transition strengths presently found in the literature.

## 4.3 Theoretical Results

### 4.3.1 Elastic Scattering

Calculations of the elastic scattering were performed with the two different codes described above. Input to the two codes which produced the calculated angular distributions shown in figure 4.1 are described below. Both codes used essentially equivalent ground state density distributions. As mentioned before, PIPIT used point proton and neutron distributions which were unfolded for the finite size of the nucleons, and DWPI used a 3pF fit to this point distribution. The 3pF parameters of this distribution were  $C=2.334$ ,  $T=0.460$ , and  $W=0.160$ , all in fm, where  $C$  is the density distribution radius,  $T$  is the diffusivity (or 10 to 90% thickness), and  $W$  is the dip parameter. Comparison calculations using PIPIT were made in which the only parameters that differed between the calculations were the 3pF fit versus the point densities distribution, and no discernible difference was seen between the two. Energy shifts used in the two codes were different, with

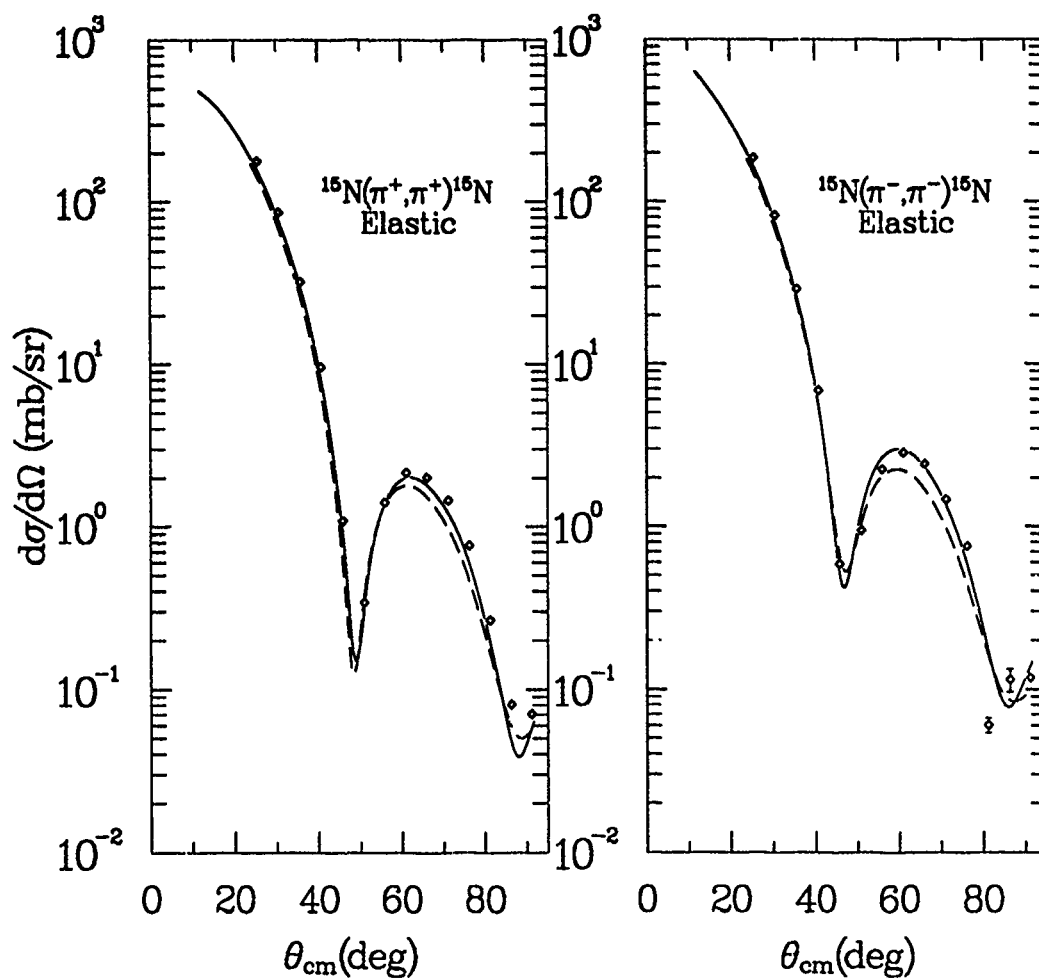


Figure 4.1: Elastic  $\pi^\pm$  data with DWPI (dashed line) and PIPIT (solid line) calculations.

the optimum shift for PIPIT at -23 MeV, and that for DWPI at -28 MeV. The shift of -28 MeV for DWPI agrees well with the results of Cottingham and Holtkamp, but considering the association of this shift with the Fermi momentum of the nucleons, it does not agree with the calculated Fermi energy of the nucleons in a nucleus of 23 MeV[PR75]. The difference in energy shift required by the two codes might be due to the fact that PIPIT has a more accurate nonlocal description of the potential, and therefore of the interaction. Finally, optimum damping factors for the  $\pi$ -N interaction range in PIPIT were found to be  $\text{DAMP1} = 3 \times 10^{-5} \text{ fm}^{-1}$  and  $\text{DAMP2} = 2.5 \times 10^{-6} \text{ fm}^{-1}$ .

Tests of the effect of changes to elastic parameters on the inelastic calculations were also made. In these tests the energy shift was varied in both elastic calculations, as well as the nuclear force range factors DAMP1 and DAMP2 in PIPIT, around the optimum values reported above. Distorted waves from these calculations were used in inelastic calculations of the state at 5.27 MeV. Angular distributions for both elastic and inelastic test calculations are shown in figures 4.2 through 4.5. These figures show that for both calculations, changes to the energy shift parameter produce much less significant changes in the inelastic distributions than in the elastics. Therefore, simple optimization of these parameters for the elastics and use of the distorted waves produced in the inelastic calculations is appropriate. The same is generally true for the range factors in PIPIT, but going to the larger momentum space range factors resulted in marked changes in the elastic and inelastic distributions. In fact, a DAMP1 value of  $3 \times 10^{-4} \text{ fm}^{-1}$  produced a divide by zero error in running the code. Care in the selection of these range factors is recommended since it appears that the code goes nonlinear with



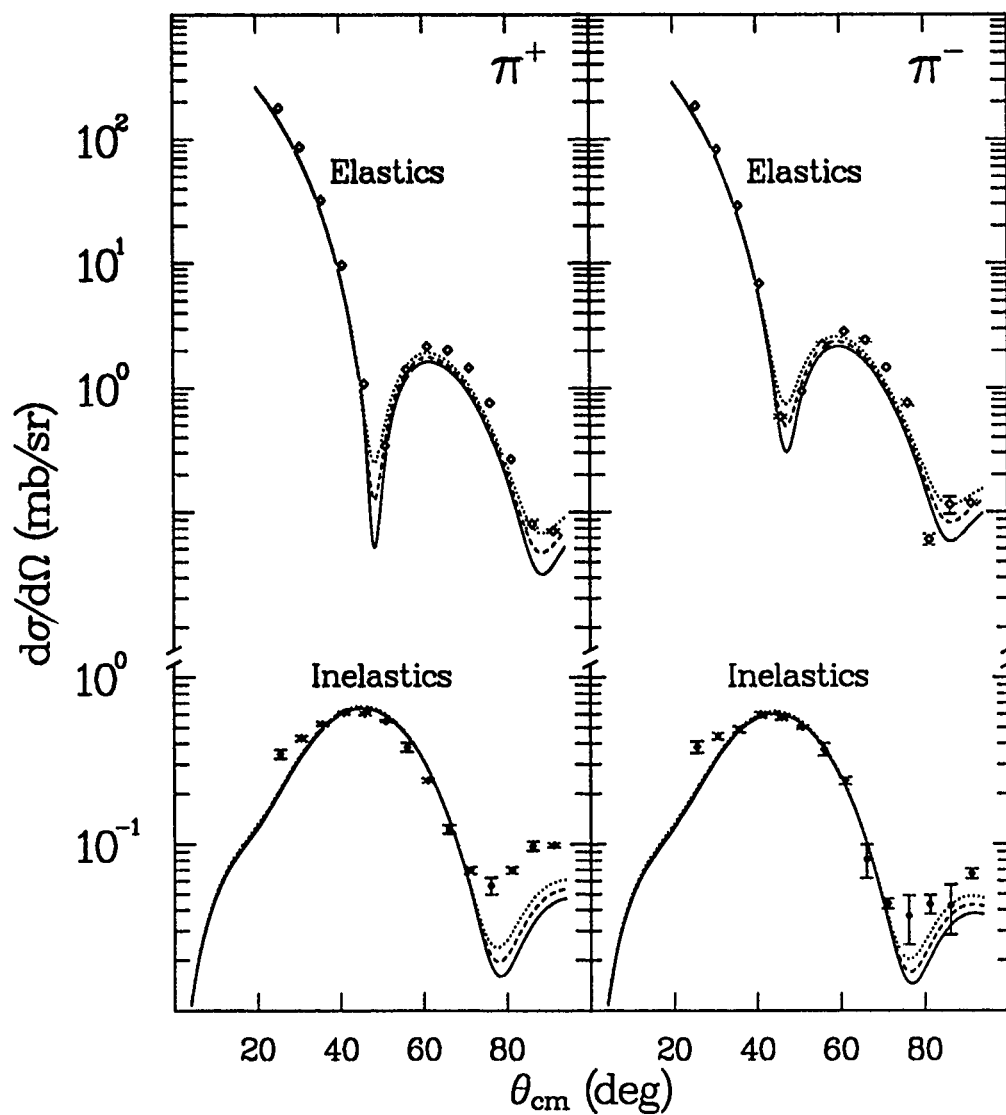


Figure 4.2: Effect of variation of energy shift elastic input parameter on inelastic calculations performed with DWPI. Solid lines, dashed lines, and dotted lines are  $E_{sh}=23, 28$ , and  $33$  MeV, respectively.

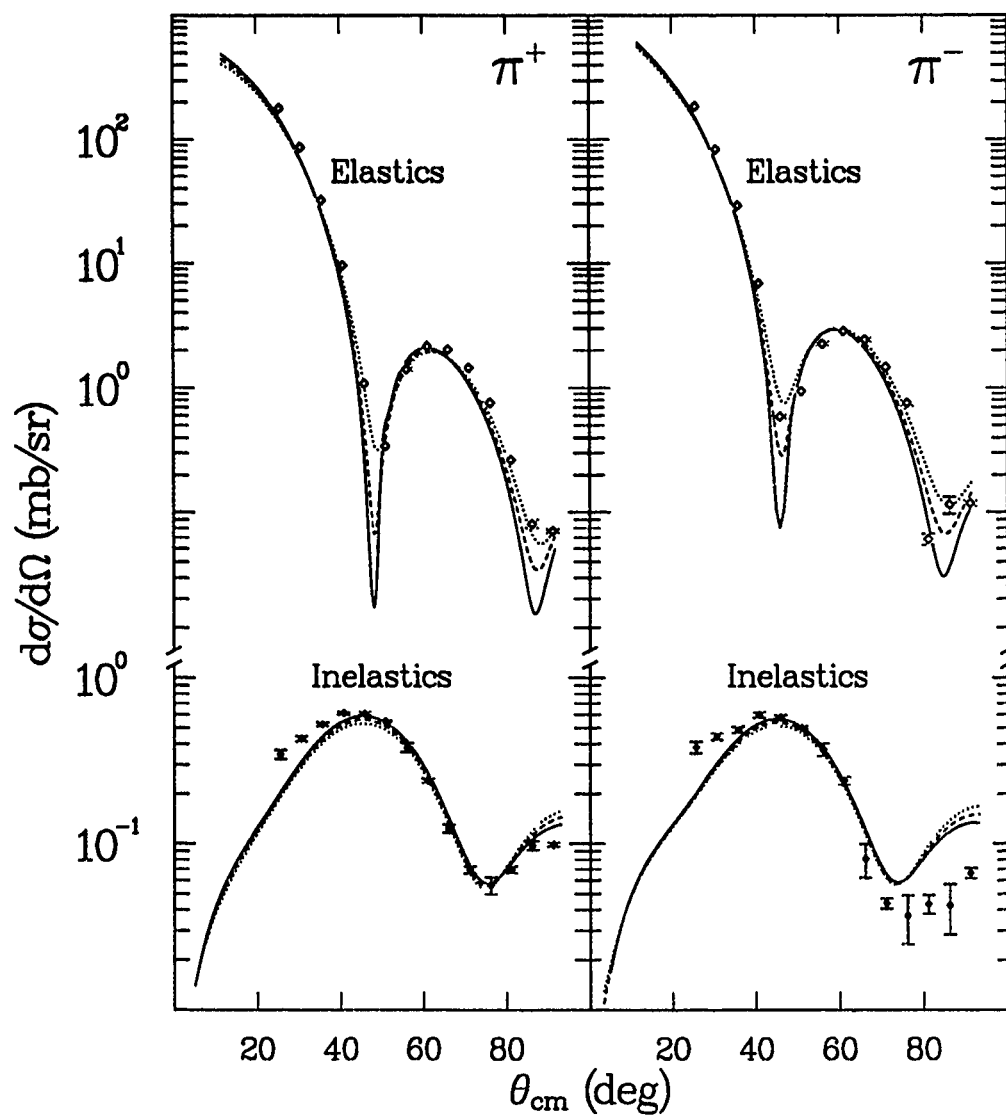


Figure 4.3: Effect of variation of energy shift elastic input parameter to PIPIT on inelastic calculations performed with ARPIN. Solid lines, dashed lines, and dotted lines are  $E_{sh}=18, 23$ , and  $28$  MeV, respectively.

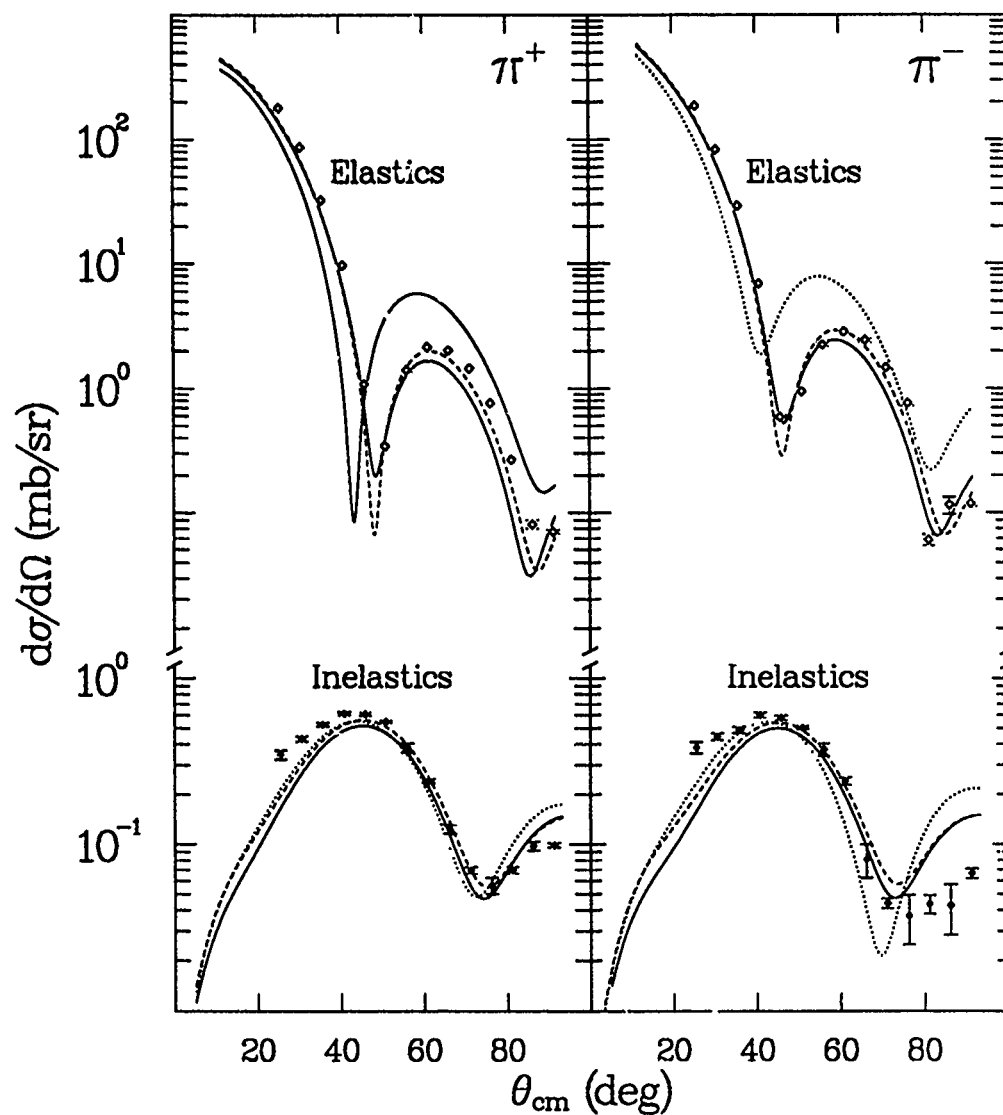


Figure 4.4: Effect of variation of momentum space s wave damping factor elastic input parameter, DAMP1, to PIPIT on inelastic calculations performed with ARPIN. Solid lines, dashed lines, and dotted lines are DAMP1 =  $3 \times 10^{-6}$ ,  $3 \times 10^{-5}$ , and  $1.5 \times 10^{-4}$ , respectively.

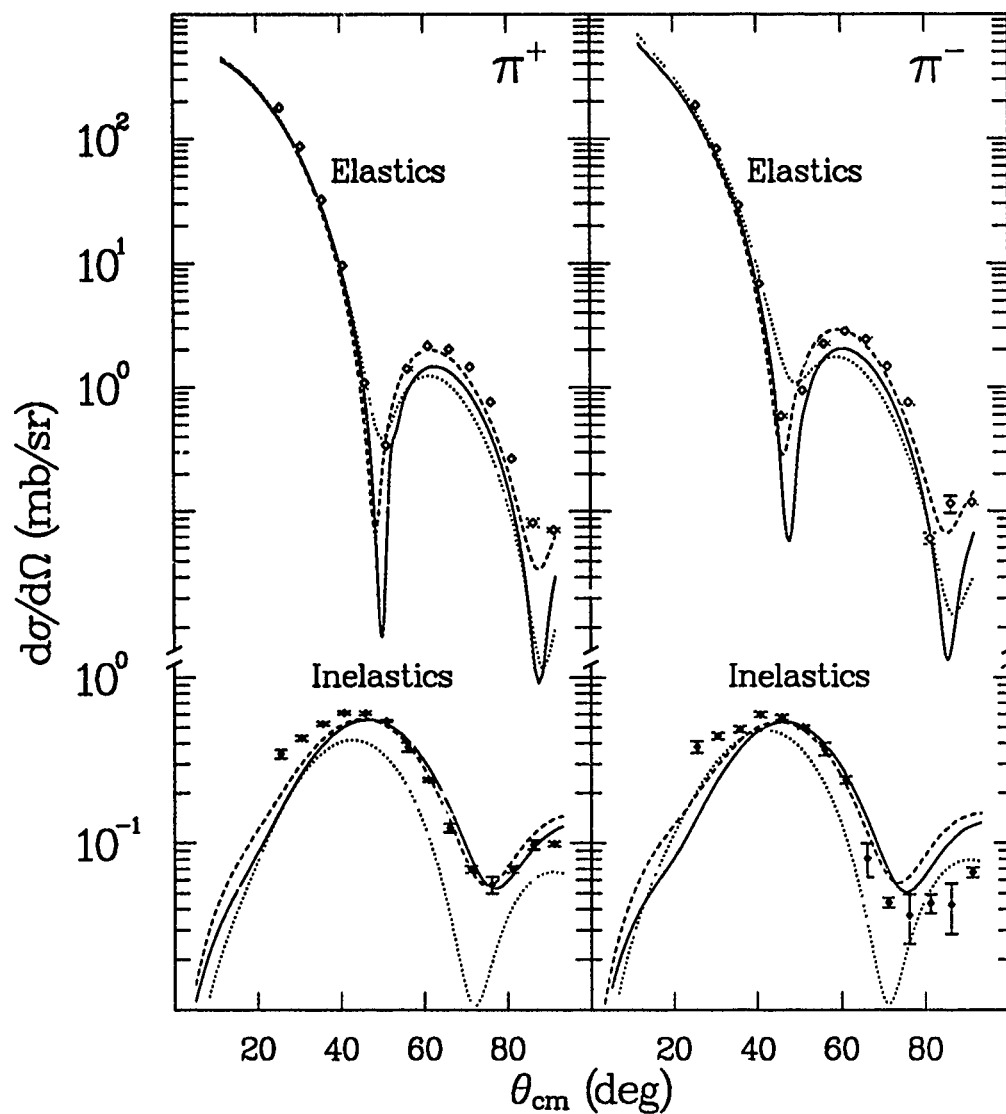


Figure 4.5: Effect of variation of momentum space p wave damping factor elastic input parameter, DAMP2, to PIPIT on inelastic calculations performed with ARPIN. Solid lines, dashed lines, and dotted lines are DAMP2 =  $2.5 \times 10^{-7}$ ,  $2.5 \times 10^{-6}$ , and  $2.5 \times 10^{-5}$ , respectively.

large values.

### 4.3.2 Inelastic Scattering

Figures 4.6 through 4.13 show the angular distributions for transitions from 5.27 up to 18.9 MeV, along with the associated theoretical calculations. Following are spin or spin-parity assignments for the states observed here, with "possible" assignments being those made in the forthcoming  $^{15}\text{N}$  inelastics paper: 5.27- ( $\frac{5}{2}^+$ ), 6.32- ( $\frac{3}{2}^-$ ), 7.16- ( $\frac{5}{2}^+$ ), 7.30- ( $\frac{3}{2}^+$ ), 7.57- ( $\frac{7}{2}^+$ ), 8.31- ( $\frac{1}{2}^+$ ), 8.57- ( $\frac{3}{2}^+$ ), 9.15- ( $\frac{3}{2}^-$  and  $\frac{5}{2}^+$ ), 9.76- ( $\frac{5}{2}^-$ ), 9.93- ( $\frac{3}{2}^-$ ), 11.29(11.24)- (possible  $\frac{7}{2}$ ), 11.88- ( $\frac{3}{2}^-$ ), 12.94(12.92)- ( $\frac{3}{2}^-$ ), 13.15- (possible  $\frac{3}{2}^-$ ), 14.38(14.24)- ( $\frac{5}{2}^+$ ), 14.65- (possible  $\frac{3}{2}^+$ ), 15.03- (possible  $\frac{5}{2}^+$ ), 16.46- (possible  $\frac{3}{2}$ ), 16.91- (possible  $\frac{3}{2}^-$ ), 17.58- ( $\frac{3}{2}^+$ ), 18.27- (possible  $\frac{3}{2}$ ), 18.70- (possible  $\frac{3}{2}$ ) and 18.91- ( $\frac{3}{2}+\frac{1}{2}$ ). (The energies given here are those at which the states were analyzed, and when there are two different energies, the one in parentheses is the energy of the known state with which the state in the present data is identified.) With EPICS' resolution at approximately 200 keV, the published literature[AJ86] shows that states of about 12 MeV energy and above are generally unresolvable from neighboring states, and some of them have multiple spin-parity assignments. Many of the high-lying states seen here were so weak that their statistics were not good enough to warrant their presentation.

The  $\pi^+/\pi^-$  cross section ratios of table 3.1 show that, at energies below about 12 MeV, asymmetries in cross section are present in almost every excitation. This indicates that these low energy transitions have distinct proton or neutron characteristics in their transition densities. This in turn

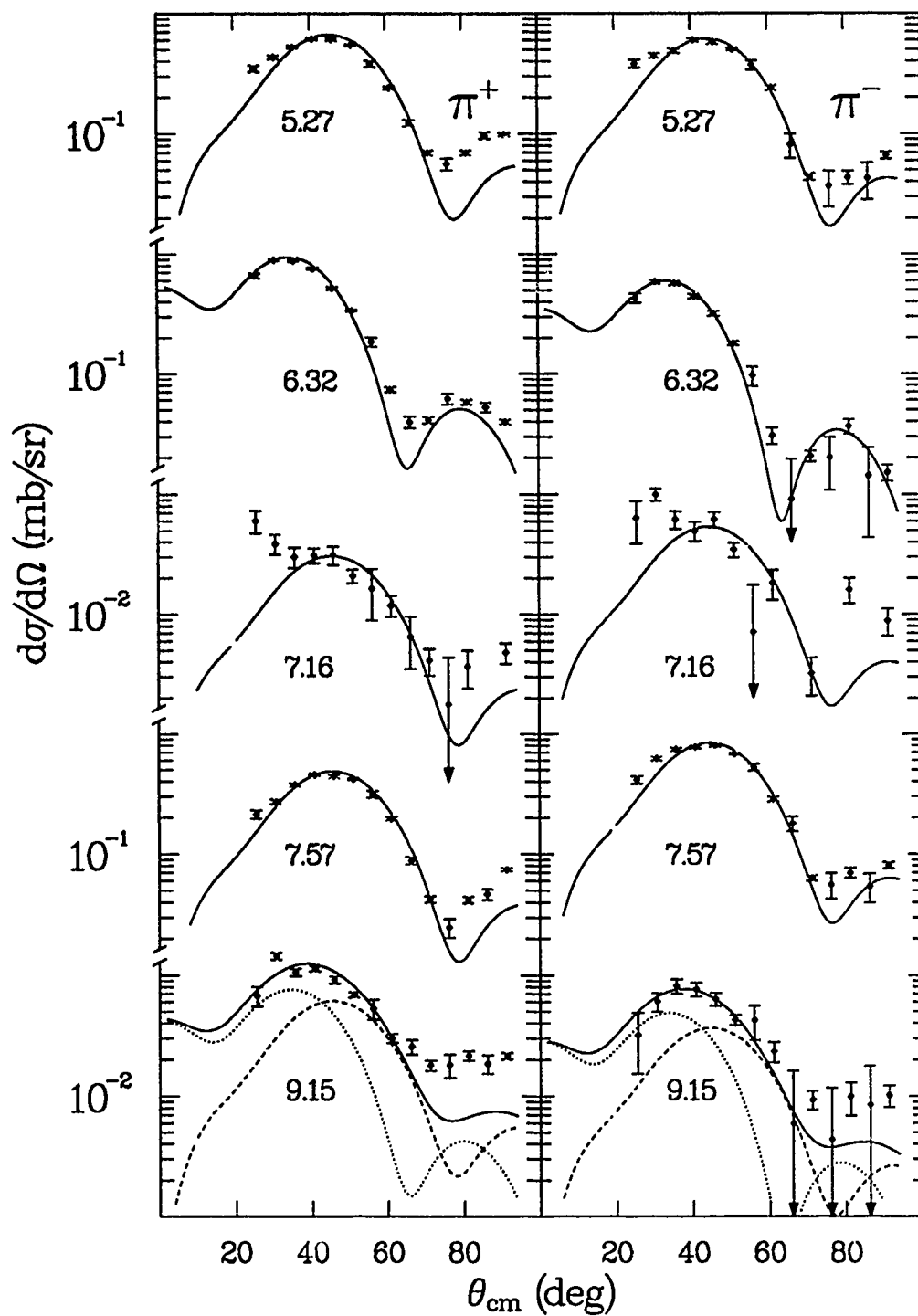


Figure 4.6: DWPI macroscopic model calculation results for states with excitation energies from 5.27 to 9.15 MeV.

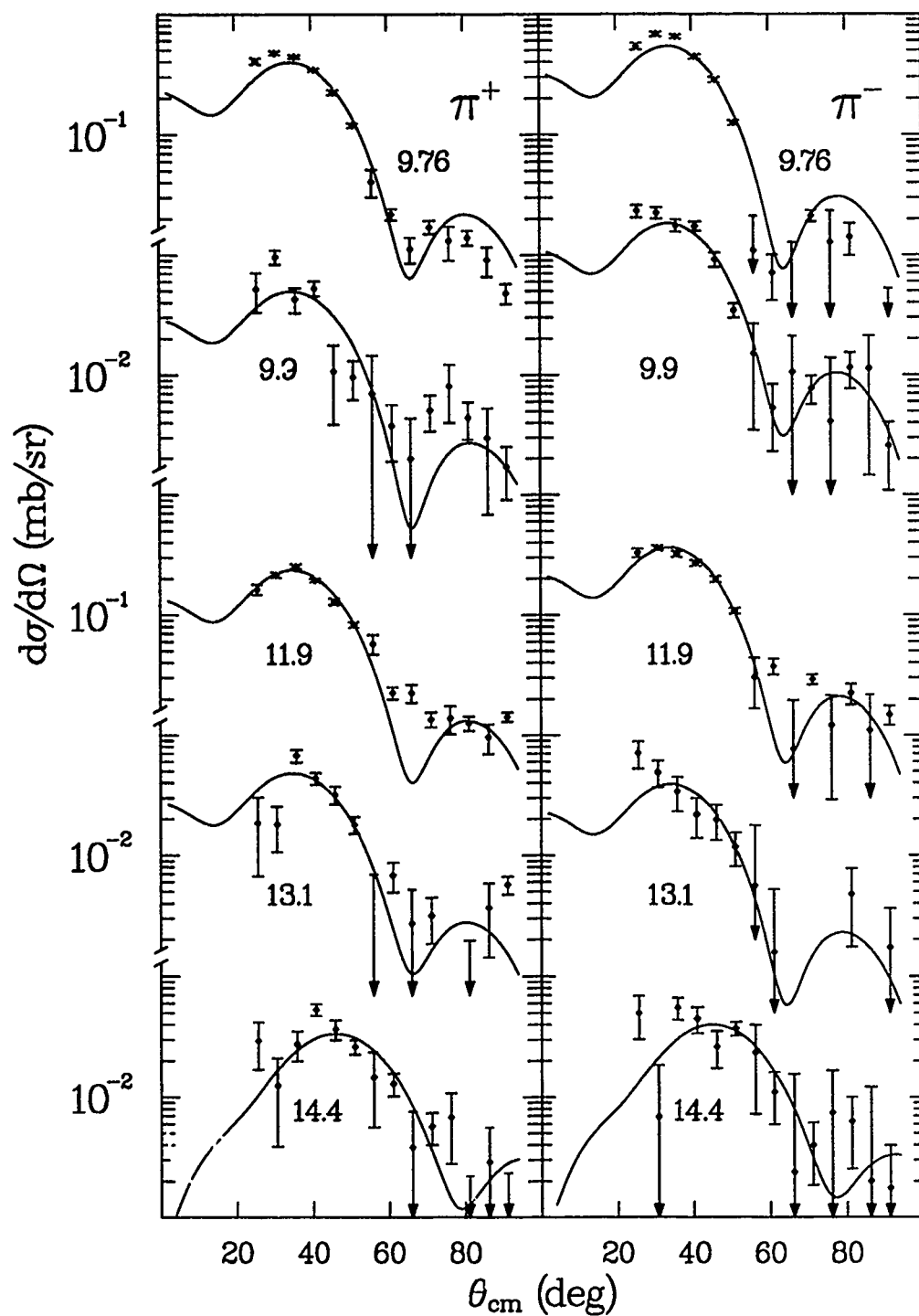


Figure 4.7: DWPI macroscopic model calculation results for states with excitation energies from 9.7 to 14.4 MeV.

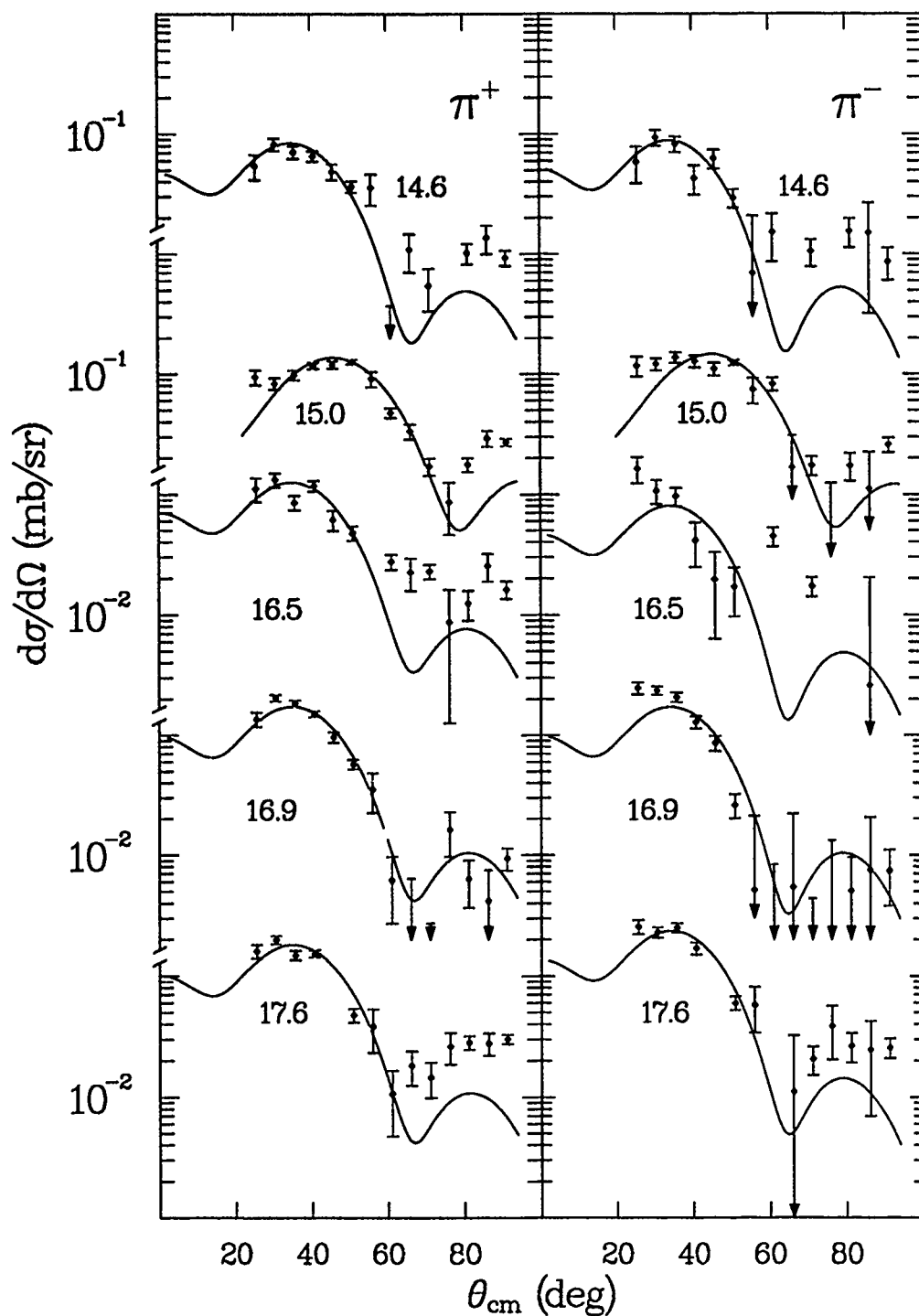


Figure 4.8: DWPI macroscopic model calculation results for states with excitation energies from 14.6 to 17.6 MeV.



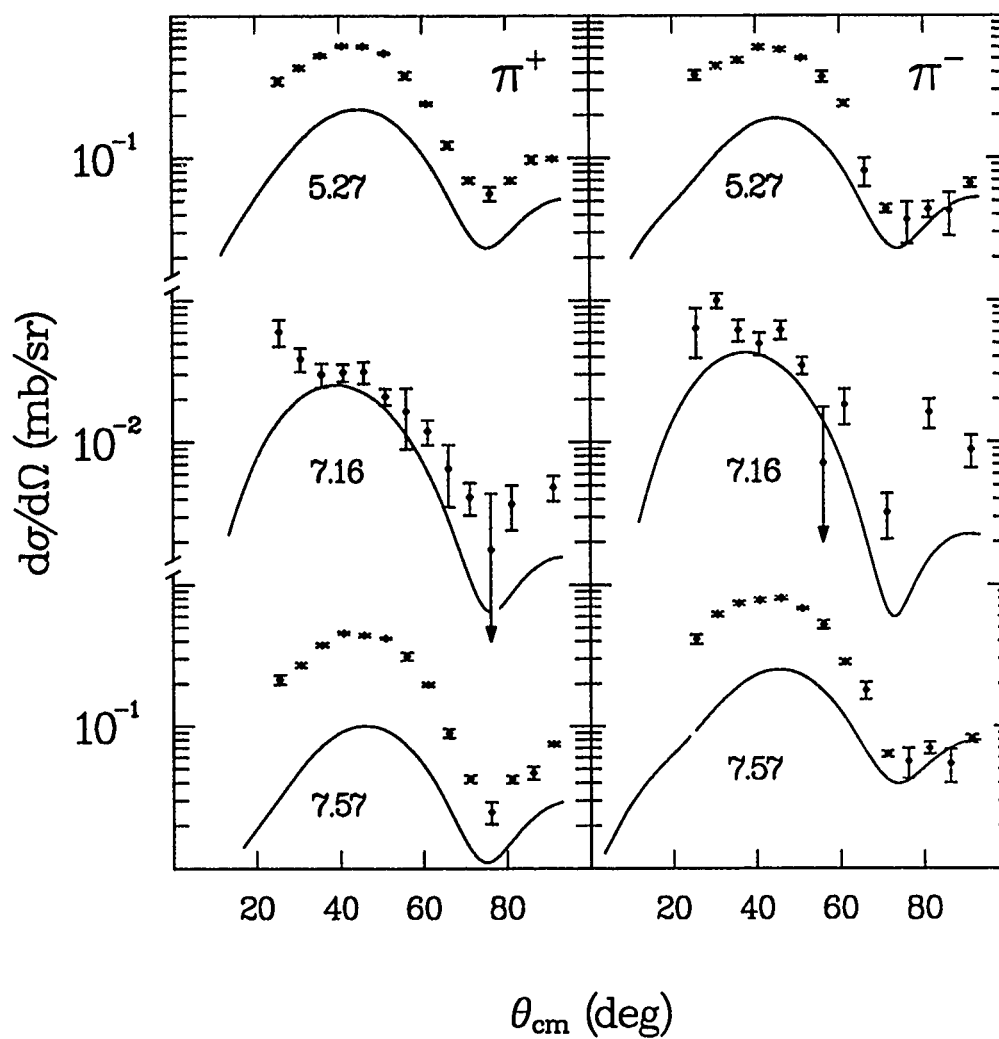


Figure 4.9: Results for ARPIN microscopic model calculations with no effective charge enhancements for states with excitation energies from 5.27 to 7.57 MeV.

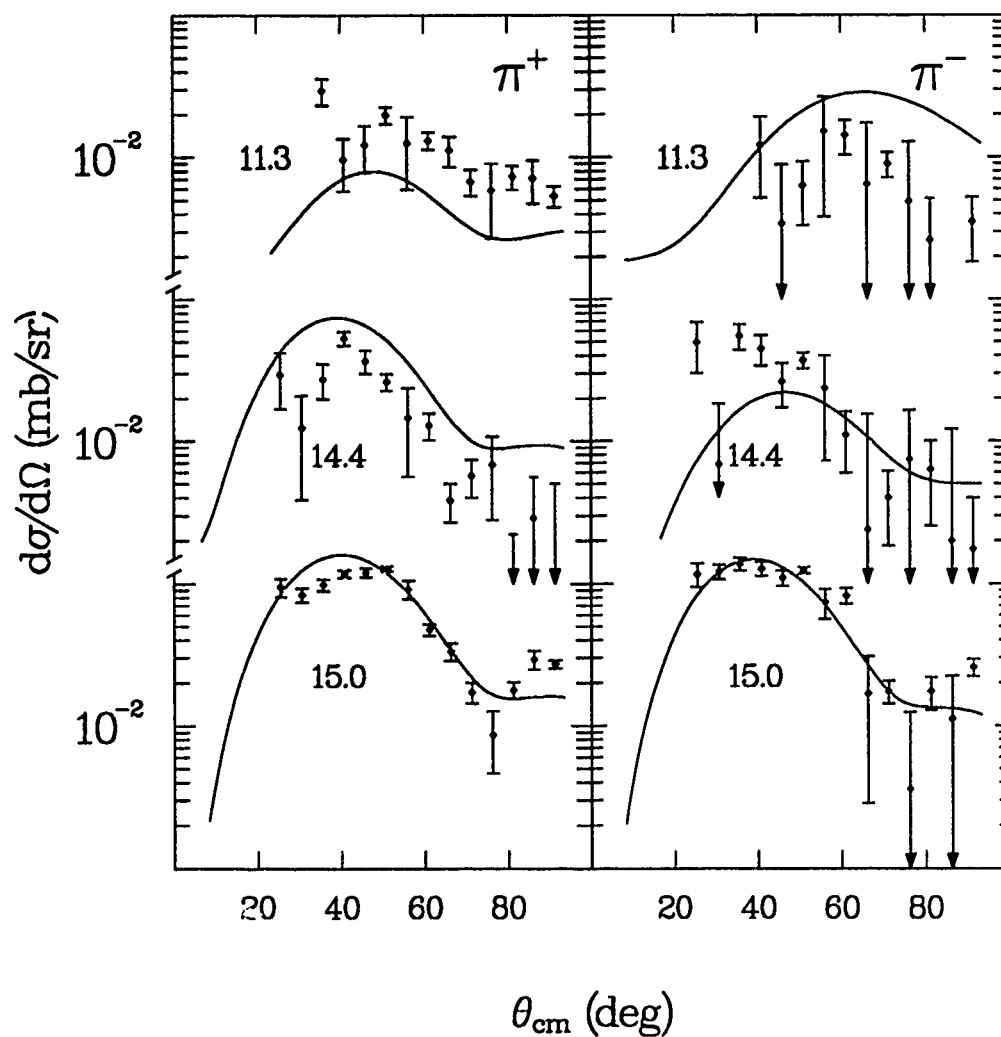


Figure 4.10: Results for ARPIN microscopic model calculations with no effective charge enhancements for states with excitation energies from 11.2 to 15.1 MeV.

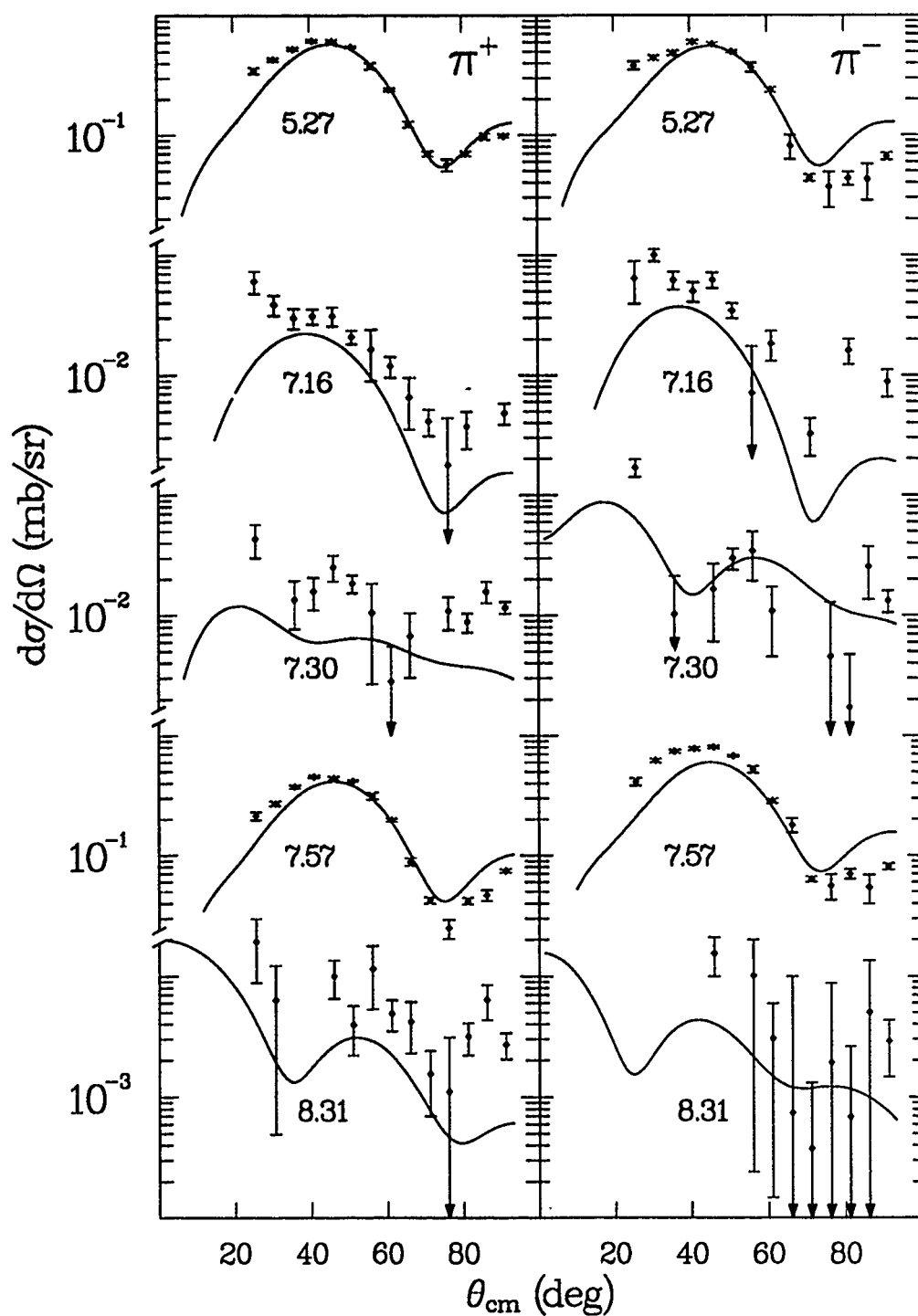


Figure 4.11: Results for ARPIN microscopic model calculations with effective charge enhancements for states with excitation energies from 5.27 to 8.31 MeV (The 8.31 MeV  $\pi^+$  calculation has been multiplied by 100 here).

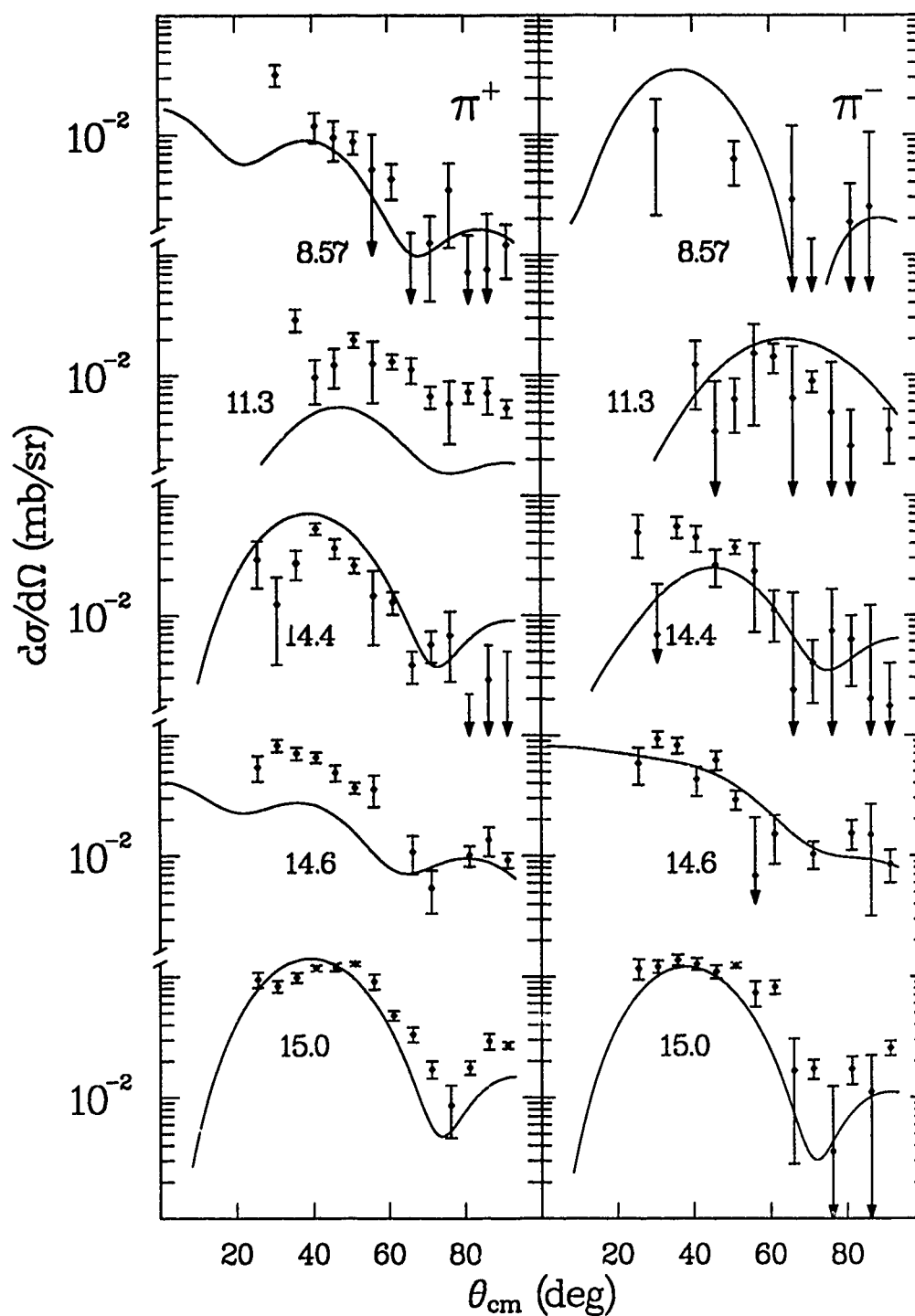


Figure 4.12: Results for ARPIN microscopic model calculations with effective charge enhancements for states with excitation energies from 8.57 to 15.1 MeV.

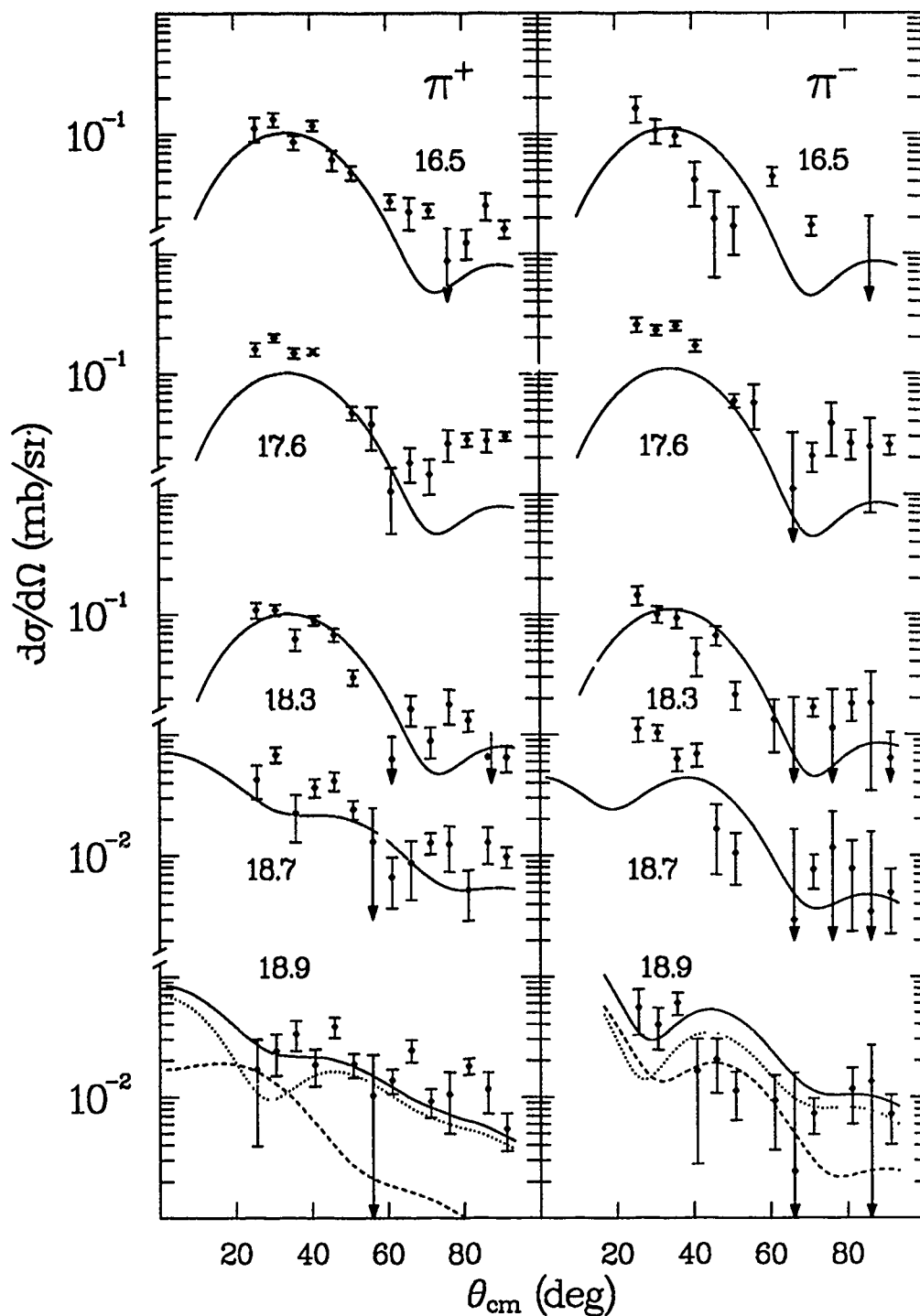


Figure 4.13: Results for ARPIN microscopic model calculations with effective charge enhancements for states with excitation energies from 16.4 to 19.0 MeV. For the state at 18.9 MeV, the dashed line is a  $J = \frac{3}{2}$  calculation, the dotted line is a  $J = \frac{1}{2}$  calculation, and the solid line is the sum of the two.

suggests that these transitions are rather discrete shell-model-like transitions. One also notices that above this energy, the ratios are mostly approximately 1. With no preferential excitation by  $\pi^+$  or  $\pi^-$  here, it appears that these states are probably much less discrete, that their excitation mechanism is basically macroscopic. There should, of course be high lying shell model states, but it appears that because of the high density of states and the spectrometer resolution of approximately 200 keV, an identification of these states is difficult. Nonetheless, because single (or few) nucleon interactions are most likely in pion excitations, it would seem reasonable to assume that shell model states would be preferentially excited. Some reasonable correlation between predicted high lying shell model states and those experimentally observed was achieved. These high energy spin-parity assignments are questionable, though.

A study of the excitation functions of these states at constant momentum transfer ( $q$ ) can, however, lead to identification of high lying distinct single component states. These  $\Delta S=1$ , "spin-flip", or "stretched" excitations have been identified in [SE85]. These states were at 10.7, 12.6, 14.1 and 17.2 MeV and contained stretched M4 strength. Figures 4.14 and 4.15 contain plots of energy dependent cross sections at constant angle and momentum transfer ( $q$  value) for the states identified as having no enhanced spin-flip excitation, while figure 4.16 shows these plots for the M4 states.

**Macroscopic Model-General Results** The macroscopic model, DWPI, was used to generate angular distributions for excited states up to an energy of 17.6 MeV. As strong states are generally collectively enhanced, their analysis with a macroscopic model calculation is interesting from a qualitative point

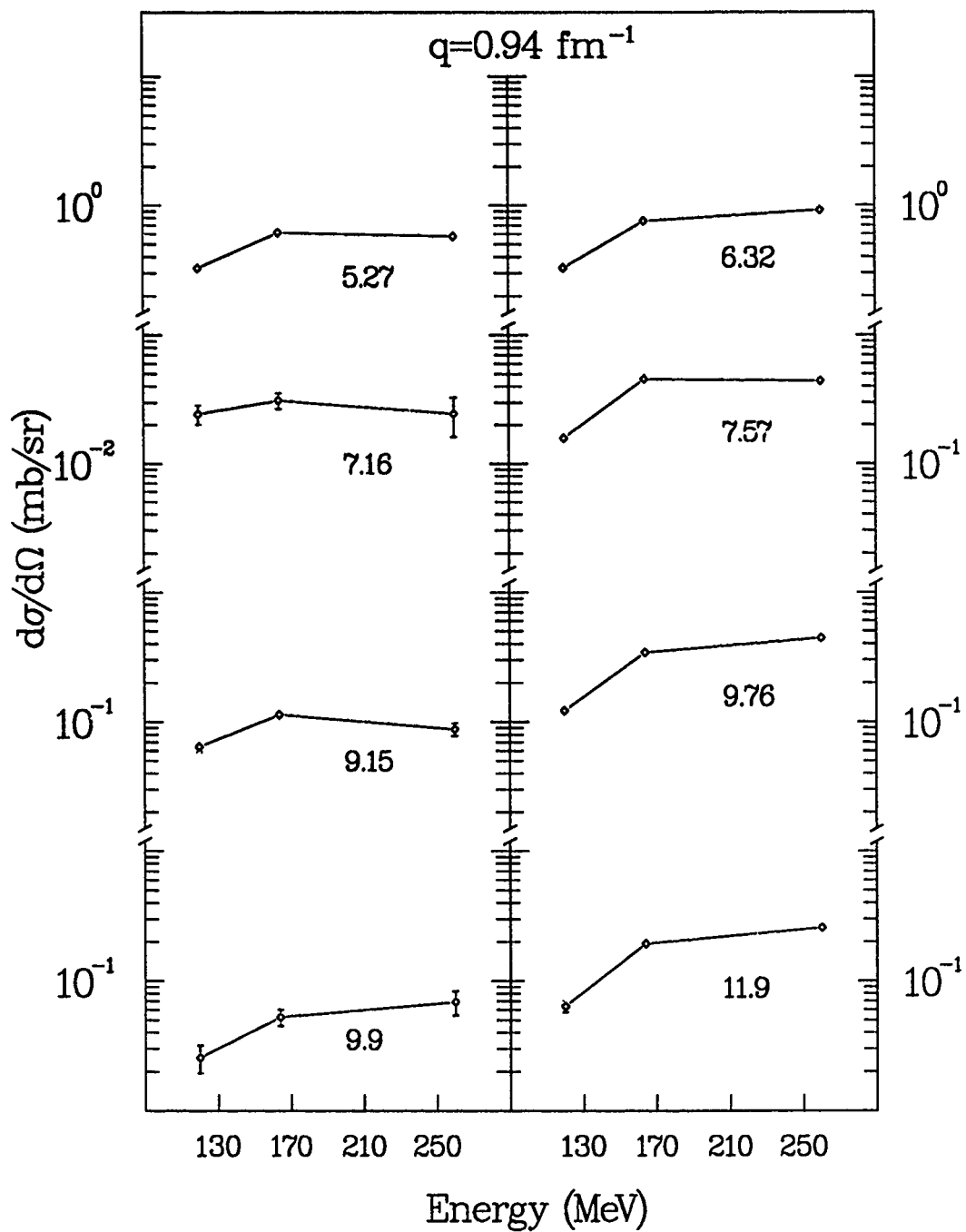


Figure 4.14: Constant momentum transfer excitation functions for states not identified as having "stretched" transitions with excitation energies from 5.27 to 11.9 MeV.

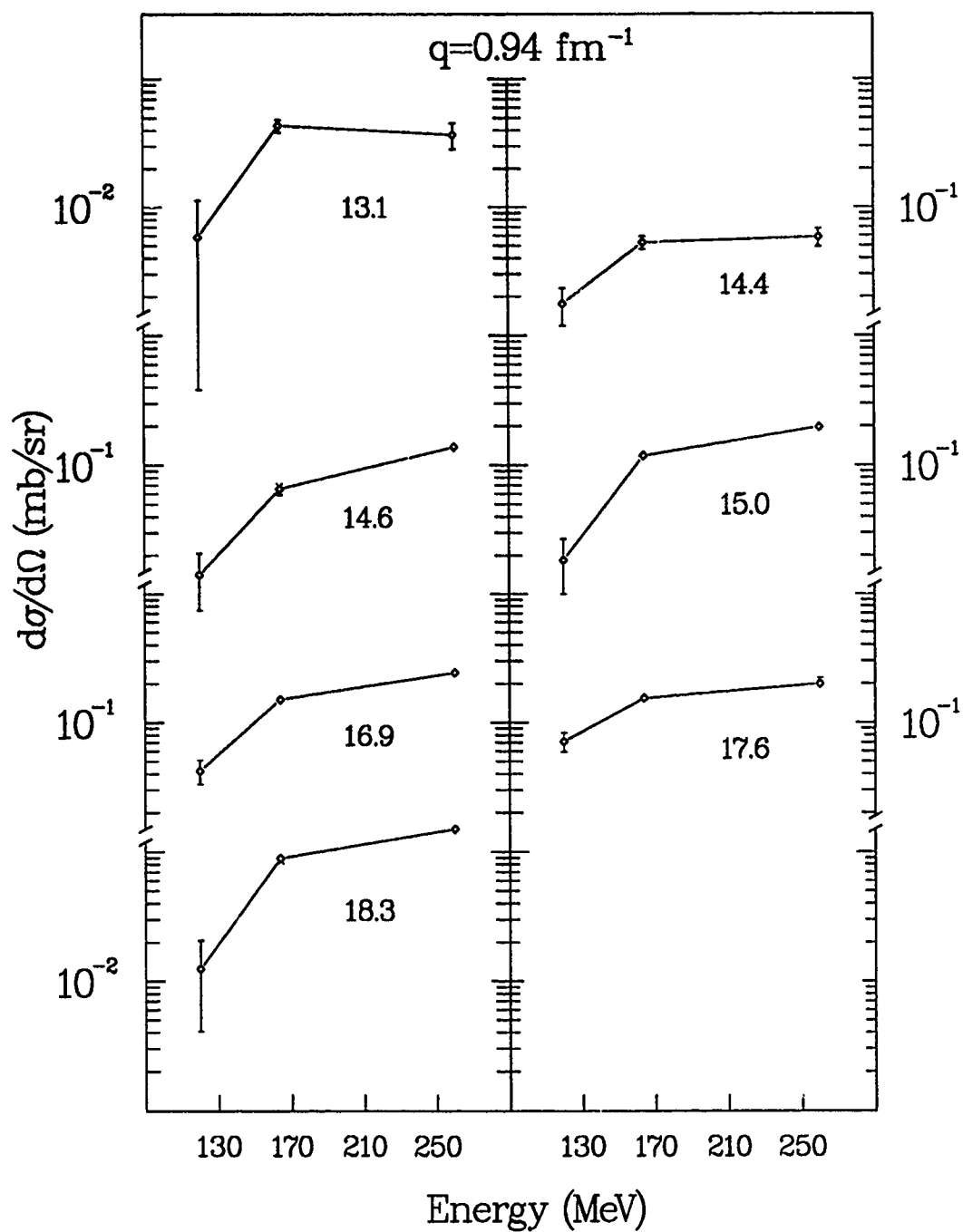


Figure 4.15: Constant momentum transfer excitation functions for states not identified as having "stretched" transitions with excitation energies from 13.1 to 18.3 MeV.



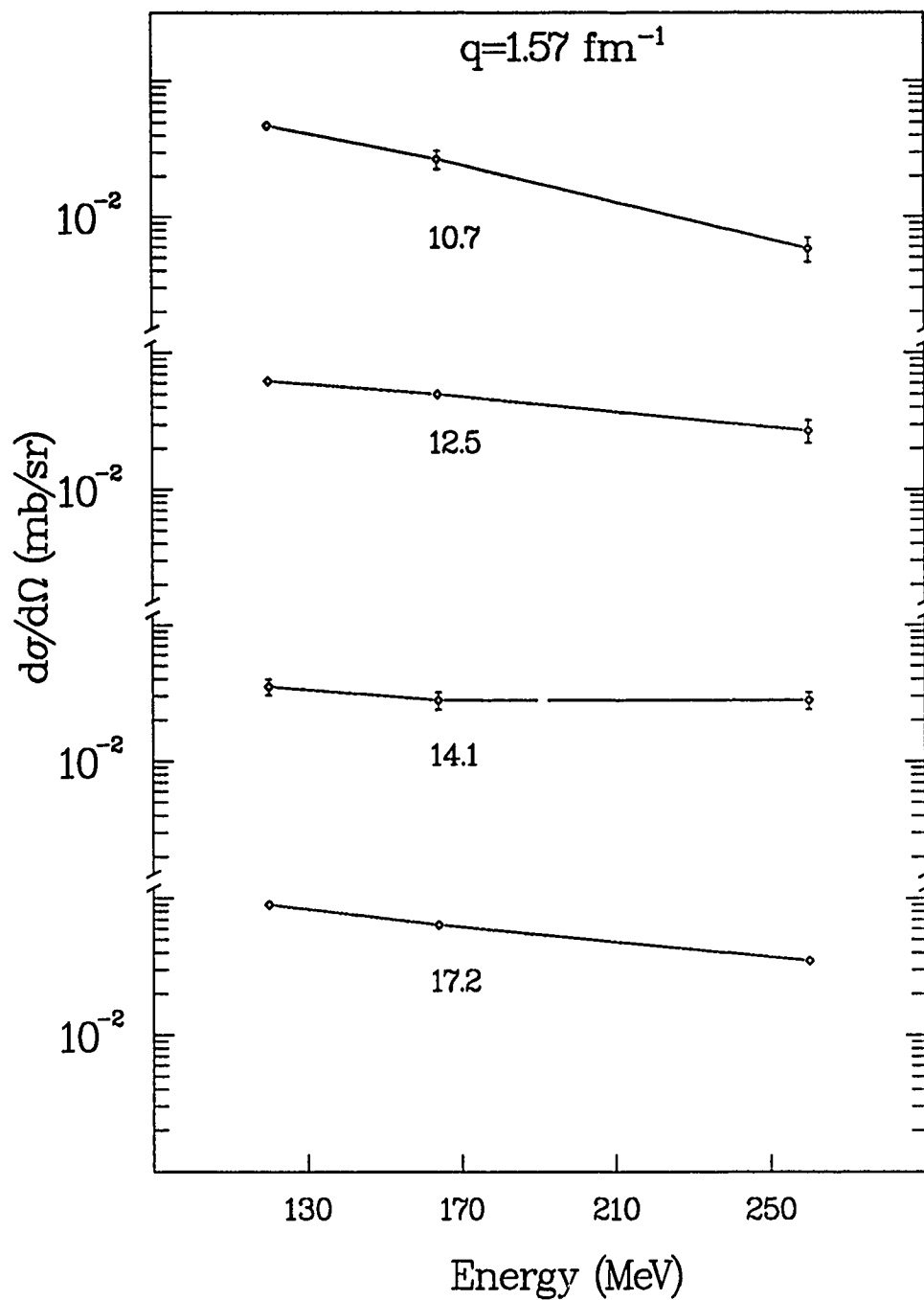


Figure 4.16: Constant momentum transfer excitation functions for states identified as having "stretched" transitions.

of view. Such an analysis was performed on these strong states, and in fact on all states observed. The plotted results on states for which DWPI and ARPIN calculations produced reasonable predictions are shown in figures 4.6 through 4.8. The basic result of this qualitative analysis is that reasonable calculations of the strong states at 5.27, 6.32, 7.16, 7.57, 9.15, 9.76, 9.9, 11.9, 13.1, 14.4, 14.6, 15.0, 16.5, 16.9, and 17.6 MeV were made. Angular momentum transfers used in these calculations were  $\Delta J = 3, 2, 3, 3, 2$  and  $3, 2, 2, 2, 2, 3, 1, 3, 1, 2$ , and  $3$  respectively. These angular momentum transfers are consistent with published spin and multipolarity to the ground state assignments. With the calculations reproducing the experimental cross sections well across the whole first diffractive maximum, they tended to underestimate the first minimum and the second peak for all but the 9.76 MeV state.

**Microscopic Model-General Results** Microscopic calculations made for states in  $^{15}\text{N}$  are shown in figures 4.9 through 4.13. Calculations other than those shown were made on other high-lying states, but their correlation with the data was questionable, so they were omitted from this paper. ARPIN was used to perform calculations with microscopic transition densities for excitation of states in the  $^{15}\text{N}$  nucleus. These calculations were made only for the positive parity states, and for energy levels up to 18.9 MeV. They were restricted to a  $1\hbar\omega$  space and produced, for a number of the states (especially the  $5/2^+$ ), cross sections which significantly underestimated the data. It was found that "effective charge" enhancements to the non-spin flip portions of the transitions were needed to generate cross sections whose magnitudes were reasonably close to those of the experimental cross sections.

These effective charges represented a collective enhancement to the discrete  $\Delta J=3$  transitions. Because the space is restricted to one unit of angular momentum transfer, some higher L transition components are omitted from the wave function, or, from another point of view, polarization of the core nucleons by asymmetries in the valence occurs, and is not accounted for in the extreme shell model. Both viewpoints lead to the conclusion that this model produces an underestimation of the strength and cross section of the transition. Isoscalar and isovector effective charges,  $\delta_0$  and  $\delta_1$ , are used to represent this polarization of the core in the model, or equivalently, to make up for the restricted model space. These effective charges simply modify the isoscalar and isovector nucleon densities[CH87] according to the following equations:

$$\rho'_0(r) = (1 + \delta_0)\rho_0(r) \quad (4.17)$$

$$\rho'_1(r) = (1 + \delta_1)\rho_1(r) \quad (4.18)$$

These enhancements were applied to the  $5/2^+$  and  $7/2^+$  states (the only ones which have LSJ=303 components) and were found to increase the cross sections as necessary to match the data. Manual variation of isoscalar and isovector effective charges produced best values of  $\delta_0=0.72$  and  $\delta_1=-0.29$  to enhance the  $\Delta J=\Delta L=3$ , (non spin-flip),  $\Delta T=0$  and  $\Delta T=1$  portions of the transitions to these states. Figures 4.9 and 4.10 only contain calculations for  $\frac{5}{2}^+$  and  $\frac{7}{2}^+$  states with no effective charge enhancements, while figures 4.11 through 4.13 contain the results for enhanced versions of these calculations along with those for states which did not require any enhancement.

The microscopic calculations, along with effective charge enhance-

Table 4.2: Neutron(n) and proton(p) One Body Density Matrix Elements for calculations made on excitation of positive parity  $J^\pi = \frac{1}{2}^+$  states in  $^{15}\text{N}$  with a  $1-\hbar\omega$  basis.

$\Delta J$		0			1				
$(\text{NLJ})_i$		$0s_{\frac{1}{2}}$	$0p_{\frac{1}{2}}$	$0p_{\frac{3}{2}}$	$0s_{\frac{1}{2}}$	$0p_{\frac{1}{2}}$	$0p_{\frac{1}{2}}$	$0p_{\frac{3}{2}}$	$0p_{\frac{3}{2}}$
$(\text{NLJ})_f$		$0p_{\frac{1}{2}}$	$1s_{\frac{1}{2}}$	$0d_{\frac{3}{2}}$	$0p_{\frac{1}{2}}$	$1s_{\frac{1}{2}}$	$0d_{\frac{3}{2}}$	$1s_{\frac{1}{2}}$	$0d_{\frac{5}{2}}$
Level 6									
$E_T=17.68$	n	.00	-.03	.47	.00	.05	-.27	-.04	.42
$E_E=18.9$	p	.04	.02	.06	-.07	.04	.00	.00	-.05

$E_T$  and  $E_E$  are theoretical and experimental energies in MeV.

ments as appropriate, produced “good calculations” of the data for the states presented in Tables 4.2 through 4.4, which are grouped by excited state  $J$  value and also give the associated theoretical energies and excitation levels. A “good calculation” reproduced the angular distribution and magnitude of the data, and had a theoretical energy within 1 MeV of the experimental energy. Some of the states for which unsuccessful identification attempts were made with the microscopic model had no spin-parity assignments in the literature, or were unresolvable from nearby states with negative or unknown parity. Lack of identification resulted in the conclusion that the strength in the state was probably from a negative parity state, or in some cases, possibly from a state whose energy was too high to be covered by the set of OBDME’s used. Neutron and Proton One Body Density Matrix Elements (OBDME’s) are also given in Tables 4.2 through 4.4.

Table 4.3: Neutron(n) and proton(p) One Body Density Matrix Elements for calculations made on excitation of positive parity  $J^\pi = \frac{3}{2}^+$  states in  $^{15}\text{N}$  with a  $1-\hbar\omega$  basis.

$\Delta J$		1					2				
$(\text{NLJ})_i$		$0p\frac{1}{2}$	$0p\frac{1}{2}$	$0p\frac{3}{2}$	$0p\frac{3}{2}$	$0p\frac{3}{2}$	$0p\frac{1}{2}$	$0p\frac{1}{2}$	$0p\frac{3}{2}$	$0p\frac{3}{2}$	$0p\frac{3}{2}$
$(\text{NLJ})_f$		$1s\frac{1}{2}$	$0d\frac{3}{2}$	$1s\frac{1}{2}$	$0d\frac{3}{2}$	$0d\frac{3}{2}$	$0d\frac{3}{2}$	$0d\frac{3}{2}$	$1s\frac{1}{2}$	$0d\frac{3}{2}$	$0d\frac{3}{2}$
Level 1											
$E_T=6.50$	n	.83	-.14	.26	.00	-.23	.01	.06	.13	.00	-.04
$E_E=7.30$	p	.00	-.09	.25	.03	-.10	-.12	.00	-.03	.00	.00
Level 2											
$E_T=8.93$	n	.02	-.02	-.02	-.03	.00	.27	.71	.06	-.06	.30
$E_E=8.57$	p	.00	.25	-.02	.05	-.15	.32	.00	-.02	-.06	.07
Level 6											
$E_T=13.98$	n	-.26	.15	.49	.15	-.04	-.29	-.10	.06	.14	.21
$E_E=14.6$	p	.00	-.17	.37	.00	-.21	-.22	.00	-.05	.06	-.08
Level 9											
$E_T=15.67$											
$E_E=16.5$											
$E_E=17.6$	n	-.10	.01	.11	.04	-.12	.00	-.10	.19	-.14	.46
$E_E=18.3$	p	.00	.01	-.20	-.02	.10	.01	.00	.13	-.04	.53
Level 8											
$E_T=14.47$	n	.20	.09	-.11	.03	.05	-.21	-.10	-.15	-.1	.44
$E_E=18.7$	p	.00	-.14	-.40	-.01	.17	-.18	.00	-.19	-.10	.18
Level 7											
$E_T=14.29$	n	.14	-.21	-.33	-.10	.30	-.20	.13	.16	.10	.04
$E_E=18.9$	p	.00	-.35	.01	-.07	.16	-.46	.00	.12	.15	-.25

$E_T$  and  $E_E$  are theoretical and experimental energies in MeV.

Table 4.4: Neutron(n) and proton(p) One Body Density Matrix Elements for calculations made on excitation of positive parity  $J^\pi = \frac{5}{2}^+, \frac{7}{2}^+$  states in  $^{15}\text{N}$  with a  $1-\hbar\omega$  basis.

$J^\pi = \frac{5}{2}^+$									
$\Delta J$									
(NLJ) <sub>i</sub>		0p $\frac{1}{2}$	0p $\frac{1}{2}$	2	0p $\frac{3}{2}$	0p $\frac{3}{2}$	0p $\frac{1}{2}$	3	0p $\frac{3}{2}$
(NLJ) <sub>f</sub>		0d $\frac{3}{2}$	0d $\frac{3}{2}$	1s $\frac{1}{2}$	0d $\frac{3}{2}$	0d $\frac{5}{2}$	0d $\frac{5}{2}$	0d $\frac{3}{2}$	0d $\frac{5}{2}$
Level 1									
E <sub>T</sub> =5.16	n	-.03	.05	.01	.04	.00	-.61	.26	-.19
E <sub>E</sub> =5.27	p	.00	-.55	-.04	-.03	-.06	-.65	.21	-.16
Level 2									
E <sub>T</sub> =7.42	n	-.18	-.62	-.01	.02	-.01	.31	-.01	-.25
E <sub>E</sub> =7.16	p	.00	-.21	-.02	.02	-.32	-.25	.00	.08
Level 6									
E <sub>T</sub> =13.50	n	.28	-.05	-.02	.06	.00	-.11	.02	.45
E <sub>E</sub> =14.4	p	.00	-.14	.22	-.06	.26	-.17	-.03	.30
Level 7									
E <sub>T</sub> =14.48	n	-.17	-.18	-.22	-.21	.57	.06	-.01	-.17
E <sub>E</sub> =15.0	p	.00	-.08	-.03	-.05	.57	-.10	.09	-.17
$J^\pi = \frac{7}{2}^+$									
$\Delta J$									
(NLJ) <sub>i</sub>		0p $\frac{1}{2}$	3	0p $\frac{3}{2}$	4	0p $\frac{3}{2}$			
(NLJ) <sub>f</sub>		0d $\frac{5}{2}$	0d $\frac{3}{2}$	1s $\frac{3}{2}$	0d $\frac{5}{2}$	0d $\frac{5}{2}$			
Level 1									
E <sub>T</sub> =6.15	n	-.87	.22	-.20		-.10			
E <sub>E</sub> =7.57	p	.00	.21	-.28		.00			
Level 2									
E <sub>T</sub> =11.15	n	.07	.03	.21		.33			
E <sub>E</sub> =11.3	p	.00	-.04	-.40		-.04			

E<sub>T</sub> and E<sub>E</sub> are theoretical and experimental energies in MeV.

## 4.4 Discussion

Following is a discussion of results for each state separately in light of the macroscopic and shell models, and in light of published literature on the states.

### 4.4.1 Low Lying Positive Parity States

#### 1/2<sup>+</sup> states

The first 1/2<sup>+</sup> state is identified in the literature[AJ86] as being at 5.30 MeV, and was unresolved from the 5/2<sup>+</sup> state at 5.27 MeV. This seems reasonable in that its published strength is 4 orders of magnitude less than that of the 5.27 MeV state[EN79]. It has also been identified as having a predominant E1 strength in transition to the ground state[EN79]. It has been suggested[OS82] that a limited idea of the relative intensities of these states could be obtained from the (combined) angular distribution, since the 5/2<sup>+</sup> state should have a maximum where the 1/2<sup>+</sup> has a minimum. A very simple analysis based on this idea, where the theoretical 5/2<sup>+</sup> calculations are subtracted from the experimental data and the result is extrapolated to 16°, where the peak 1/2<sup>+</sup> cross section should occur, gives a maximum 1/2<sup>+</sup>  $\pi^+$  cross section of about .22mb/sr, and  $\pi^-$  of about .26mb/sr, to give a  $\frac{\sigma(\pi^+)}{\sigma(\pi^-)}$  ratio (R) of 0.85. These estimates of  $\pi^+$  and  $\pi^-$  cross sections are considerably higher than predicted by the ARPIN shell model calculations (on the order of .03mb/sr) or Oset and Strottman's[OS82] (about .08mb/sr). Finally, the R of 0.85 does appear to agree with Oset and Strottman's quantitative calculations, but does not support the qualitative assertion that, in

a simple model where this is mainly a  $(1p_{1/2})^{-2}(2s_{1/2})$ , 1p-2h,  $T_h=1$  state (the  $T_h$  model), it should be excited appreciably more in a  $\pi^+$  reaction since a proton excitation would necessarily yield  $T_h=1$ . Calculations by Lie and Engeland[LI70] do not agree with this simple model, but instead predict a dominant 3p-4h strength of 65%, and a small 1p-2h,  $T_h=1$  strength of 23%. Nonetheless, ARPIN microscopic calculations agree with this assertion, showing the largest transition amplitudes for this component, (with  $\Delta J=1$ ), the proton amplitudes dominating, and also producing a theoretical R of 1.24.

The next  $1/2^+$  state is identified[AJ86] with an excitation energy of 8.31 MeV. This state was present in the data, but with poor statistics, especially for the  $\pi^-$  cross sections. Microscopic DWIA calculations reproduced the shape of the  $\pi^+$  experimental cross sections fairly well, but were almost three orders of magnitude too low. Macroscopic calculations failed to reproduce the shape at all. Table 3.1 shows a R of 1.41, which is at odds with the ( $T_h$  model) theory[OS82] that this  $T_h=0$  state should be preferentially excited by  $\pi^-$ . Lie and Engeland calculate a 69% 1p-2h  $T_h=1$  contribution to this state, in disagreement with the  $T_h$  model, but considering that their third  $1/2^+$  state has a large  $T_h=0$ , one might assume that the second and third  $1/2^+$  states are a  $T_h=1,0$  pair. Once again, though, the ARPIN microscopic calculation agrees with this theory and shows a dominant  $(1p_{1/2})^{-2}(2s_{1/2})$  ( $\Delta J=0$ ) neutron amplitude for this state. One cannot say, because of the poor  $\pi^-$  statistics and the lack of agreement with the  $\pi^+$  data magnitude, that the calculation is reasonable. No other low lying  $1/2^+$  states were observed, and the microscopic calculations indicate cross sections which would be too low for them to show up.



### 3/2<sup>+</sup> states

The first 3/2<sup>+</sup> state is identified as having an energy of 7.30 MeV [AJ86], and as having a predominant E1 transition to the ground state [EN79]. The calculations of Lie and Engeland show large (53% or greater) 1p-2h  $T_h=0$  strengths and small (6% or less)  $T_h=1$  strengths for the three lowest 3/2<sup>+</sup> states, in disagreement with the  $T_h$  model. Calculations for this state do show its largest amplitude in an E1 transition, in agreement with its identification, but this amplitude lies in a  $1p_{1/2}$  to  $2s_{1/2}$  neutron transition, which according to the simple  $T_h$  model, would indicate that it is the  $T_h=0$  member of one of the model pairs. According to the model, the other member of the pair would have to have a lower energy and a large  $1p_{1/2}$  to  $2s_{1/2}$  proton transition, but there is no lower energy 3/2<sup>+</sup> state. However, the microscopic model does not predict the shape or amplitude of the  $\pi^+$  data well at all, though it does agree with the  $\pi^-$  data, which has poor statistics. So the calculations are suspect, and a simple  $T_h$  model might do better here. The data itself does not really support this model either, though, with a R of 1.01.

The second 3/2<sup>+</sup> state is at 8.57 MeV [AJ86]. The calculations agree with the shape of the  $\pi^+$  data, though the magnitude of the prediction is a little low, and once again, the  $\pi^-$  data has poor statistics. The calculations have a dominant  $1p_{1/2}$  to  $1d_{3/2}$  neutron amplitude, with  $1p_{1/2}$  to  $1d_{3/2}$  neutron and proton amplitudes both of about half the magnitude of the dominant transition. These amplitudes are also difficult to reconcile with the simple  $T_h$  model. The experimental R here is 1.87, which does not agree with the  $T_h$  model. We observed no other low lying 3/2<sup>+</sup> states, and the calculations indicate that they could have been overshadowed by background or nearby

stronger states in the spectra.

### 5/2<sup>+</sup> states

The state at 5.27 MeV has been identified as the first  $J^\pi = 5/2^+$  [AJ86], and is reached by a predominantly E3 transition from the ground state [EN79]. In support of the  $T_h$  model here are calculations by Lie and Engeland [LI70] which indicate that there is a large  $5/2^+$ ,  $1p-2h$ ,  $T_h=1$  amplitude ( $A=.77$ ) in this state. Calculations by Alford and Purser agree ( $A=.93$ ) [AL69]. The experimental  $R$  of 1.15 is also in support. Table 4.4 indicates approximately equal neutron/proton contributions in the ARPIN calculations, which predict the data well, disagreeing with the simple  $T_h$  model.

The second  $5/2^+$  state is identified at 7.16 MeV [AJ86], with a predominant E3 transition [EN79] to the ground state. Lie and Engeland's calculations indicate a dominant (80%)  $1p-2h$   $T_h=0$  component in this state, which makes the 5.27 MeV state and this one the only pair on which the simple  $T_h$  model agrees with their calculations. The experimental  $R$  of 0.68 also agrees with the  $T_h$  model. The shell model calculations include a dominant  $M2$   $1p_{1/2}$  to  $1d_{3/2}$  transition, which in light of the E3 identification in the literature, calls them into question. They also contain a somewhat lower amplitude E3  $1p_{1/2}$  to  $1d_{3/2}$  component, and with the effective charge values used on all of the E3 components in the calculations, they are only somewhat low on their predictions of the  $\pi^+$  and  $\pi^-$  data. The neutron/proton amplitudes for this transition are also approximately equal, putting the ARPIN calculations in disagreement with the  $T_h$  model.

The third  $5/2^+$  state is at 9.16 MeV [AJ86] and was unresolved from

a  $3/2^-$  state at 9.15 MeV in the data. The DWPI macroscopic calculations, with a combination of both  $J=3/2$  and  $5/2$  cross sections, reproduced the data well. The microscopic calculations, on the other hand, appeared not to produce enough E3 strength to predict the  $5/2^+$  portion of the cross section. They also indicated that the fourth  $5/2^+$  state, (seen in the literature at 10.53 MeV), should have been strong enough to appear in the data, but it didn't.

#### $7/2^+$ states

The 7.57 MeV state is identified as the first  $7/2^+$  state[AJ86], and has a predominant E3 strength to the ground state[EN79]. Lie and Engeland calculate an almost complete dominance (95%) of a  $1p-2h$ ,  $T_h=0$  component for this state, disagreeing with the  $T_h$  model. The microscopic calculations don't support the model, with a dominant  $1p_{1/2}$  to  $1d_{3/2}$  neutron amplitude. The experimental R of 0.62 also disagrees. There are no other low lying  $7/2^+$  states, which again calls into question the simple  $T_h$  model.

#### 4.4.2 High Lying Positive Parity States

These states are treated in order of increasing energy, and identifications of  $J^\pi$  are generally questionable. The identifications are made based on the presence of a state of that or unknown  $J^\pi$  in the literature[AJ86] which is within the spectrometer resolution energy of the state of interest, a good match of the predicted angular dependent cross section to the experimental cross section and, for states of energy up to 16.5 MeV, a theoretical energy within 1 MeV of the experimental energy. For states above 16.5 MeV, all of which (except the 18.91 MeV state, which we deal with separately) appear to

be  $J=3/2$  states, we identify them with lower energy theoretical states since the  $1\hbar\omega$  model runs out of  $3/2^+$  states at 16.5 MeV. Theoretical energies and OBDME's are included in the tables presented for the states' respective identified  $J^\pi$ .

The first of the high lying positive parity states was seen experimentally at 11.3 MeV. The state at 11.29 MeV is identified in the literature[AJ86] as a  $J^\pi = 1/2^-$ , but the experimental angular distribution doesn't have the shape of a  $J=1/2$  transition. There is a nearby state at 11.24 MeV which has a  $J$  assignment of  $3/2$  or greater, and since the second level  $7/2^+$  theoretical calculation at 11.15 MeV matches reasonably well, we associate it with this state.

Considering the 14.4 MeV state, there is a 14.38 MeV state identified as having  $J^\pi=7/2^+$ [AJ86]. None of the  $7/2^+$  microscopic calculations match the data, though the  $5/2^+$  level 6 calculation does, and is presented in Fig. 4.12. Macroscopic model calculations with  $\Delta J=3$  and an excited state  $J$  of  $7/2$  do match the data, however, and these calculations are presented in Fig. 4.7. Since the  $R$  for this state is 0.98, we assume that it is collective and rely on the macroscopic model in saying it is probably a  $J=7/2$  state, with  $\Delta J=3$  from the ground state.

The state at 14.65 MeV has an unidentified  $J^\pi$ . Both macroscopic and microscopic calculations for this state indicate that its  $J$  is  $3/2$ , though the two calculations have very different shapes. With a  $R$  of 1.03 it appears that this state is also collective, and we propose its description as a  $J=3/2$ , with  $\Delta J=1$  from the ground state, based on the macroscopic calculations.

The state at 15.0 MeV is very strong in the data, and both microscopic and macroscopic calculations indicate that it is a  $J=5/2$  state, with  $\Delta J=3$  from the ground state. The microscopic calculation which predicted this state was for the seventh  $5/2^+$  level in the model, and had a theoretical energy of 14.48 MeV. The  $R$  of 0.99 indicates that it is a highly collective state.

The  $\pi^-$  statistics on the state at 16.5 MeV are poor, and we base its identification on the  $\pi^+$  data. Both calculations indicate that it is a  $J=3/2$ , with a  $\Delta J=1$  transition to the ground state.

The state at 17.6 MeV is also a strong state in the data. There is a state at 17.58 MeV in the literature[AJ86] identified as a  $3/2^+$  state, and both calculations on the 17.6 MeV state agree with this. Its  $R$  indicates that it is a collective state, and the agreement with the magnitude of the microscopic calculations appears to be completely accidental, since the theoretical state is predicted at an energy of 15.67 MeV. The microscopic calculation was made solely to get a confirmation of the experimental  $J^\pi$ , since we ran out of  $3/2^+$  levels and no level assignment was possible.

The states near 18.3 and 18.7 MeV have unknown  $J^\pi$ . We identify them here as possible  $J^\pi=3/2^+$  states, since their shapes seemed to be described fairly well by microscopic  $3/2^+$  levels 9 and 8 calculations, respectively. Both of these states have a  $R$  of 1.25, indicating that they are fairly collective, but the macroscopic model failed to predict their angular dependent cross section shapes.

Finally, the state at 18.91 MeV is described in the literature as a

$J^\pi=(1/2^++3/2^+)$  state. Experimental R's once again indicate that this state is collective, but again, the macroscopic calculations fail to predict the shapes. Fig. 4.13 shows microscopic calculations for the theoretical  $1/2^+$  level 6 and  $3/2^+$  level 7 added to obtain a reasonable match to the experimental data.

#### 4.4.3 Stretched (M4) Excitation States

Data and calculations taken from [SE85] for states which are thought to have significant strength from a stretched transition are shown in figures 4.17 through 4.20. This work is also based on the experiment 703 data. As mentioned before, these states are identified as stretched states based on their large (or small)  $\frac{\sigma(\pi^+)}{\sigma(\pi^-)}$  ratios, on the shape of their angular distributions, and on the (negative) slope of their excitation functions at constant angular momentum transfer. It must be noted that the 12.5 and 14.1 MeV  $\pi^-$  distributions do not have this characteristic M4 shape. This leads one to assume that these states are not simply the result of M4 strength, but also of strength from lower multiplicities. This assumption is supported by the smaller than expected  $\frac{\sigma(\pi^+)}{\sigma(\pi^-)}$  ratios found in the experiment. The multiple multipolarity assumption is also supported, in the case of the 14.1 MeV state, by its almost flat excitation function. These facts led to calculations of these states which included the addition of C2 and C3 strength. These multiple multipolarity calculations lead to more pronounced  $\frac{\sigma(\pi^+)}{\sigma(\pi^-)}$  ratios, as well as to a reconciliation of the angular distribution shape and excitation function slope problems. Considering only the M4 portions of these calculations results in larger  $\frac{\sigma(\pi^+)}{\sigma(\pi^-)}$  ratios of approximately 9 for the 10.7 and 12.5 MeV states, and approximately 2 and 0.7 for the 14.1 and 17.2 MeV states, respectively.

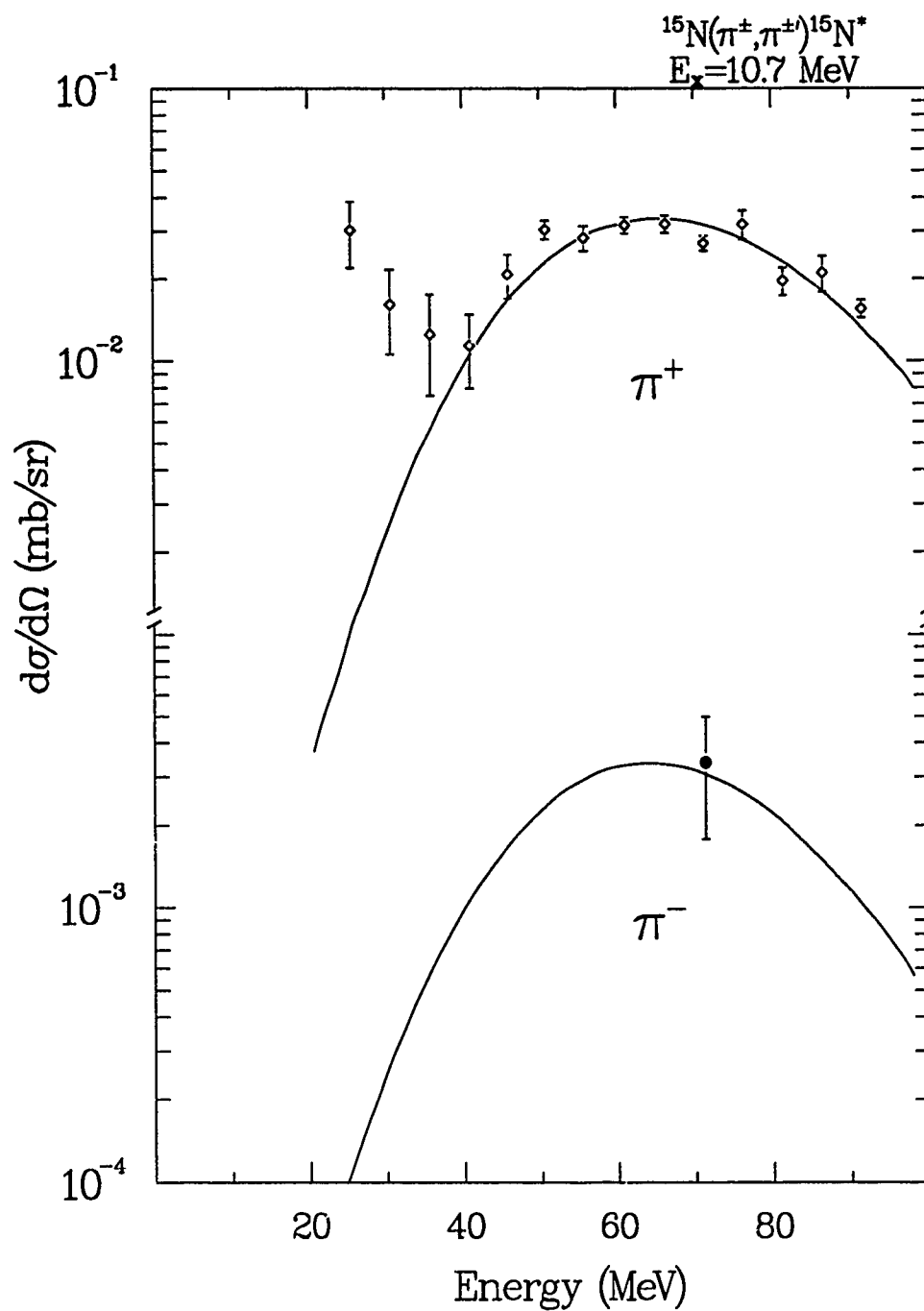


Figure 4.17:  $\pi^+$  angular distribution and  $70^\circ$  differential cross section, along with a pure M4 calculation, for 164 MeV pion scattering from  $^{15}\text{N}$  to the excited state at 10.7 MeV.

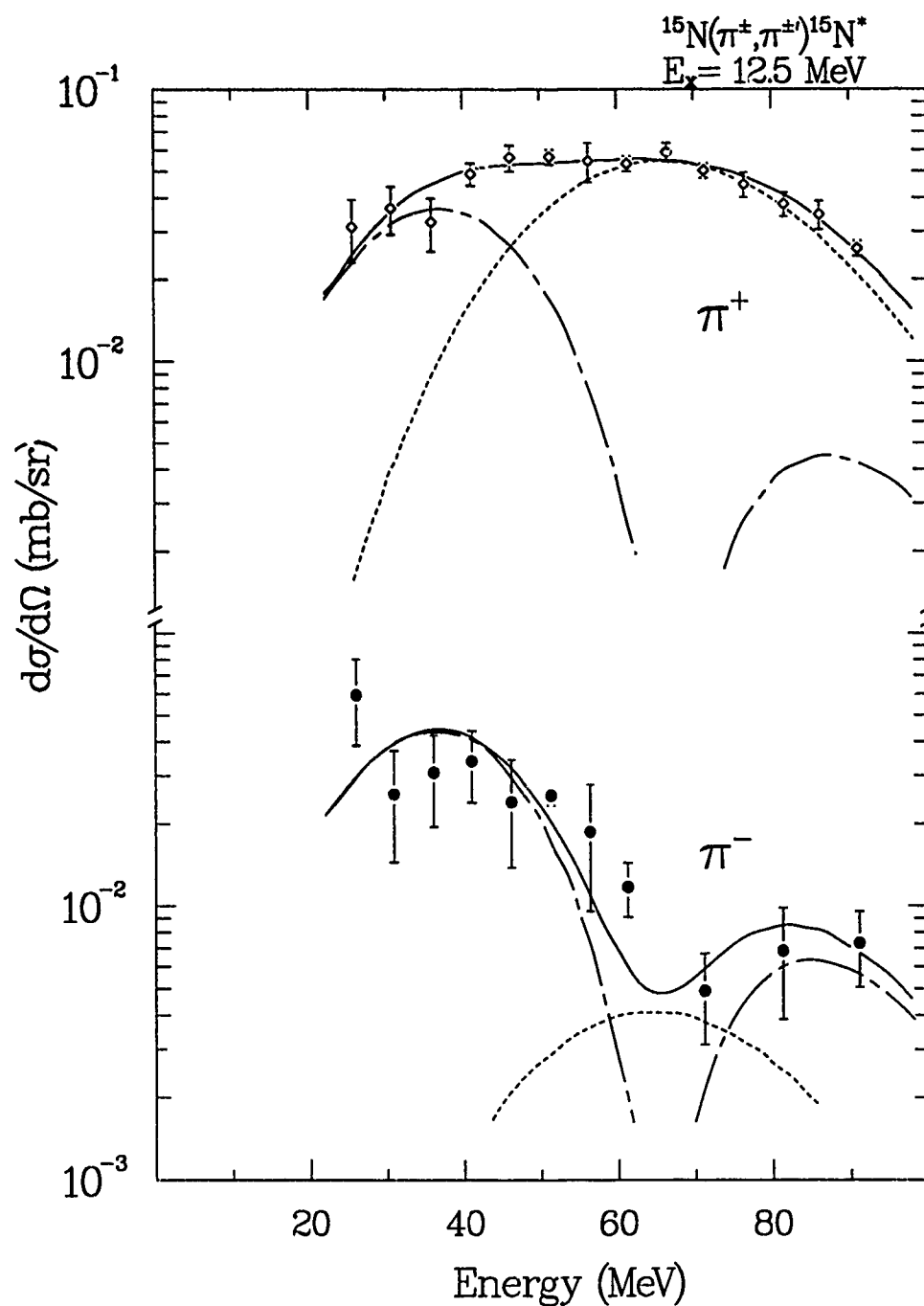


Figure 4.18:  $\pi^{\pm}$  angular distributions, along with a M4 calculation (dotted line), a C2 calculation (chain-dash lines), and the sum of these two calculations (solid line), for 164 MeV pion scattering from  $^{15}\text{N}$  to the excited state at 12.5 MeV.



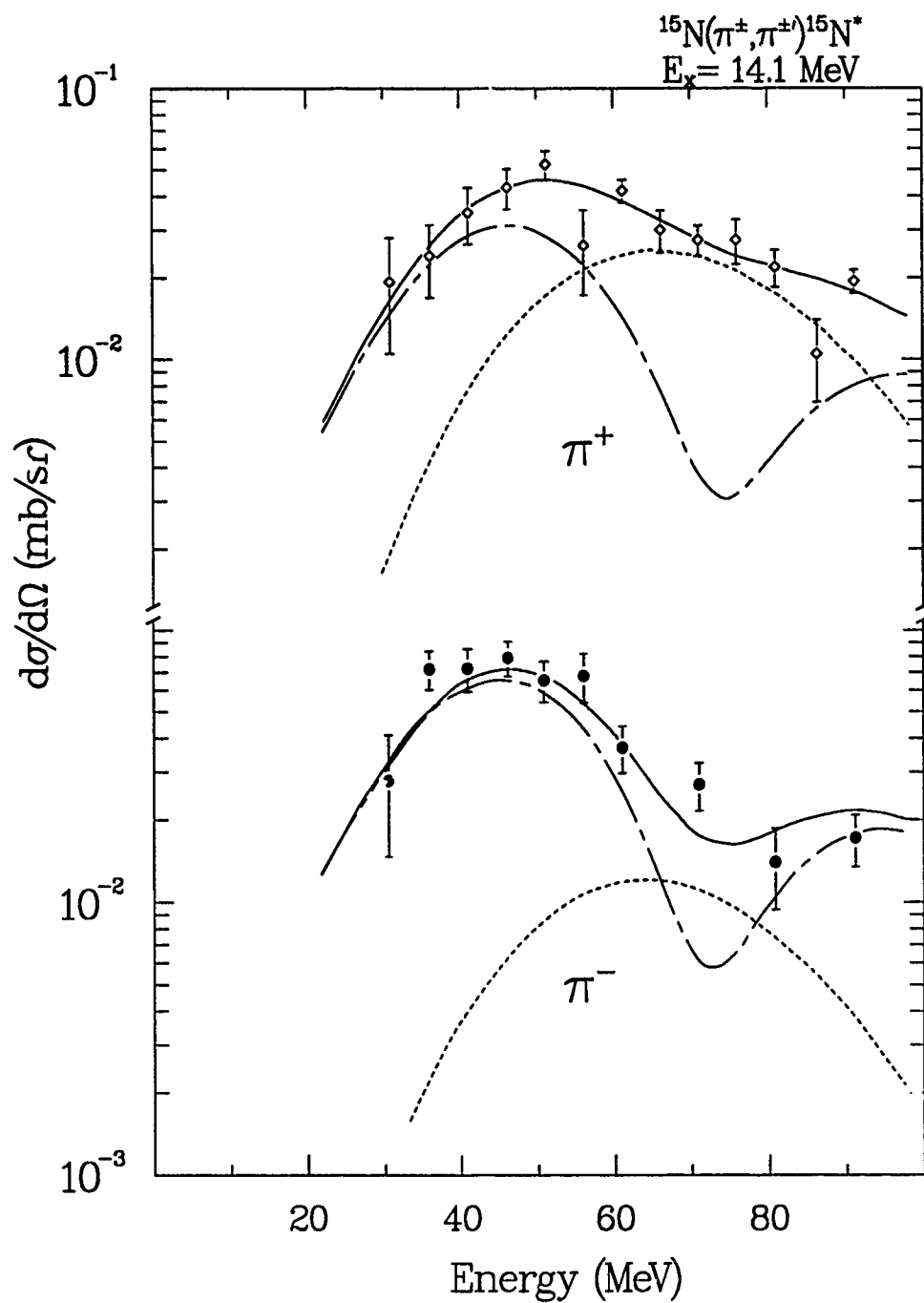


Figure 4.19:  $\pi^{\pm}$  angular distributions, along with a M4 calculation (dotted line), a C3 calculation (chain-dash lines), and the sum of these two calculations (solid line), for 164 MeV pion scattering from  $^{15}\text{N}$  to the excited state at 14.1 MeV.

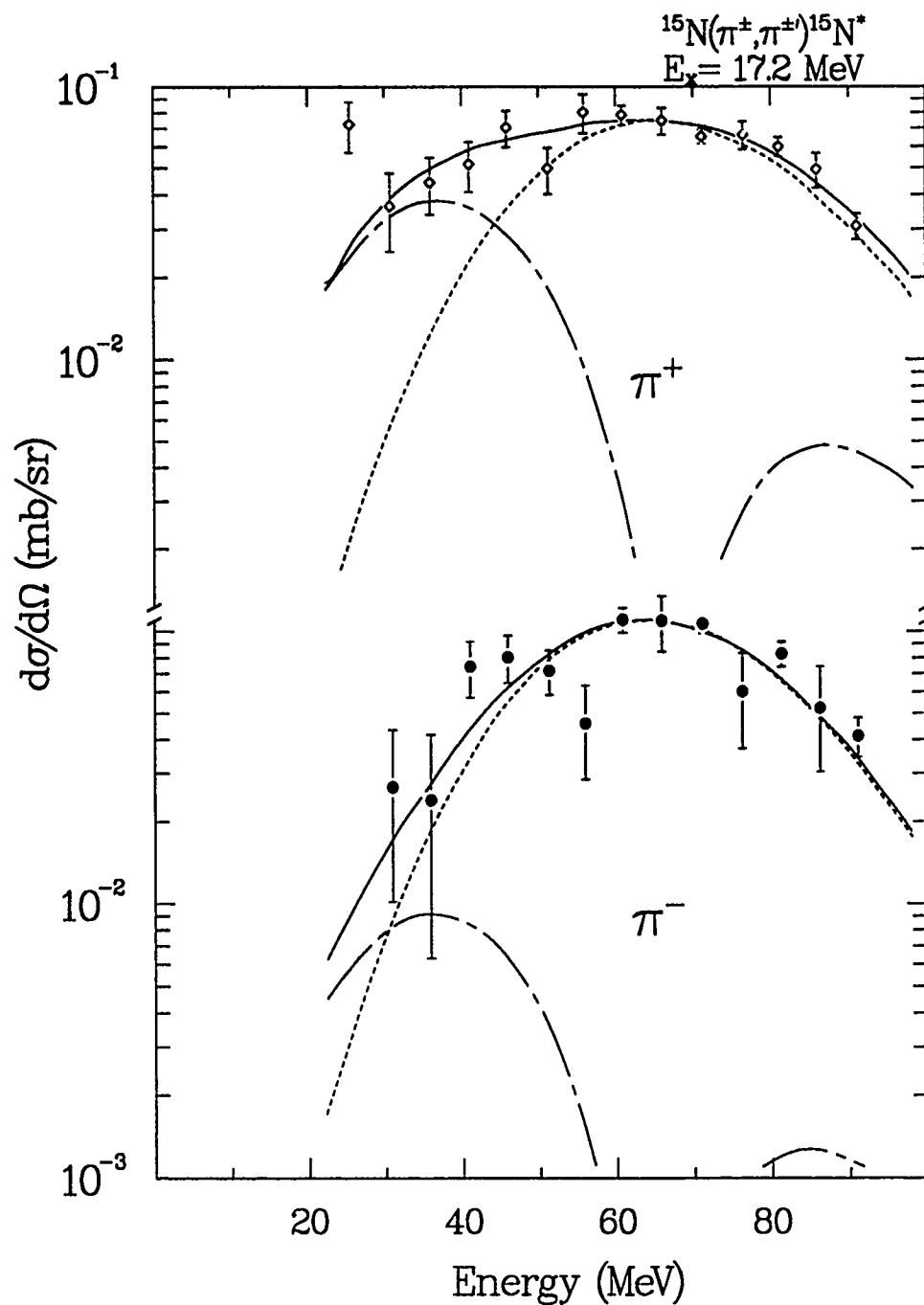


Figure 4.20:  $\pi^\pm$  angular distributions, along with a M4 calculation (dotted line), a C2 calculation (chain-dash lines), and the sum of these two calculations (solid line), for 164 MeV pion scattering from  $^{15}\text{N}$  to the excited state at 17.2 MeV.

These ratios indicate an almost pure proton excitation of the 10.7 and 12.5 MeV states via M4 excitation, proton dominance of the 14.1 MeV state, and neutron dominance of the state at 17.2 MeV.

The DWIA microscopic calculations performed with ARPIN, using shell model wave function calculations which were once again essentially the same as those presented in [MI75], were performed for comparison to the data, and these are shown in figures 4.17 through 4.20. Based on this comparison, isoscalar and isovector spectroscopic amplitudes were deduced. These amplitudes are comparable to form factors obtained from electron scattering, and this comparison was good for all but the state at 14.1 MeV.

From a consideration of figure 1.4, and its associated description in the text, two low energy proton dominated states are expected, which have a  $d_{\frac{5}{2}}^+$  proton coupled to the  $^{14}\text{C } 2^+ T_h=0,1$  states. Shell model calculations using a  $1\hbar\omega$  basis indicate that this configuration should actually result in a single  $\frac{9}{2}^+$  state at 11.64 MeV. The next  $\frac{9}{2}^+$  state is predicted by the model to be at 15.66 MeV, which is too high an energy to correlate to the 12.5 MeV experimental state. It is found that when a  $(1 + 3)\hbar\omega$  model is considered, which allows for 3p-4h configurations, splitting of the lowest  $\frac{9}{2}^+$  level into 2 states occurs. Additional evidence for the presence of the 3p-4h strength here comes, at least for the 10.7 MeV state, from the strength seen for this state in the  $^{12}\text{C}(\alpha, p)^{15}\text{N}$  reaction. Calculations which assume a simple two-state mixing of the lowest 1p-2h and 3p-4h states result in amplitudes which, if one assumes they add constructively for the 10.7 MeV state, produce cross sections for excitation of the 10.7 and 12.5 MeV states consistent with those seen experimentally in the  $^{12}\text{C}(\alpha, p)^{15}\text{N}$  reaction. (Which may mean nothing for

the 12.5 MeV state, since it has an essentially 0 cross section in this reaction, which might mean that it has 0 3p-4h amplitude). The fact that neither the 14.1 nor the 17.2 MeV states are seen strongly in the 3 particle transfer reactions may mean that they are 1p-2h states. Electron scattering form factors for the 17.2 MeV state quoted in [SE85] indicate that this transition has a very strong isoscalar excitation. This description is exactly that of the second  $\frac{9}{2}^+$  state in the shell model calculations, and also correlates with the simple description of this state in a weak coupling model as a  $d_{\frac{5}{2}}$  neutron coupled to a  $^{14}\text{N } 2^+$  state as in figure 1.4b). This, plus the identification[AJ86] of the 10.7-12.5 MeV pair as the lowest  $\frac{9}{2}^+$  states, indicates that the 14.1 MeV state is  $J^\pi = \frac{7}{2}^+$ .

Finally, sum rule fraction calculations showed a smaller fraction of the theoretically predicted isoscalar strength was detected in this experiment than that of the isovector strength. This is thought to be the result of the greater fragmentation of the isoscalar states, resulting from the fact that these states can have either  $\Delta T=0$  or  $\Delta T=1$ , as opposed to the isovector, which can have only  $\Delta T=1$ .

#### 4.4.4 Negative Parity States

At the lower end of the excitation energies in  $^{15}\text{N}$  there is only one negative parity excited state, which is at 6.32 MeV. This is a one hole state, where a proton hole moves from the  $1p_{\frac{1}{2}}$  to the  $1p_{\frac{3}{2}}$  shell, and is the only negative parity state that can be modeled in a  $1\hbar\omega$  space. In the extreme shell model, movement of this proton hole should produce the only strength in the

transition, and we should therefore get a 9:1 ratio for R. The experimental ratio of 1.78 indicates that this transition is collectively enhanced. Calculations with neutron and proton effective charges are shown in Fig. 4.21. These calculations include the expected  $0p_{3/2} \rightarrow 0p_{1/2}$ , but also contain a  $(LSJ) = (202)$  component scaled by neutron and proton polarization charges  $(1 + \delta_n)$  and  $(1 + \delta_p)$ , where  $\delta_n = 0.3$  and  $\delta_p = 1.0$ . This is in agreement with the work of Macauley *et. al.* [MA76], Suzuki [SU76], and Horikawa *et. al.* [HO77]. Higher lying negative parity states start at about 9 MeV with transitions from the 1p shell to the 1fg-2p shell. Macroscopic DWIA calculations were performed for all states seen consistently in the spectra, and identified the spin-parity ( $J^\pi$ ) of the low lying (less than 12 MeV) negative parity states by energy in the literature [AJ86]. These states are at 6.32, 9.15, 9.76, 9.93, and 11.88 MeV. Their assigned  $J^\pi$  values are  $3/2^-$ ,  $3/2^-$ ,  $5/2^-$ ,  $3/2^-$ , and  $3/2^-$ , respectively. Assigned multipolarities are E2 for the 6.32 and 9.76 MeV states, with which the calculations agree. Further, the calculations for the other low lying negative parity states all used spin transfers of  $\Delta J=2$ . Tenuous identification of higher lying states at 13.1 and 16.9 MeV as  $3/2^-$  is made in the forthcoming  $^{15}\text{N}$  paper. This identification is based on their angular dependent cross sections' similarity to those of the low lying negative parity states, and on the inability of the positive parity microscopic calculations to predict their shape. Other states predicted by the macroscopic DWIA did not correlate well with the data.

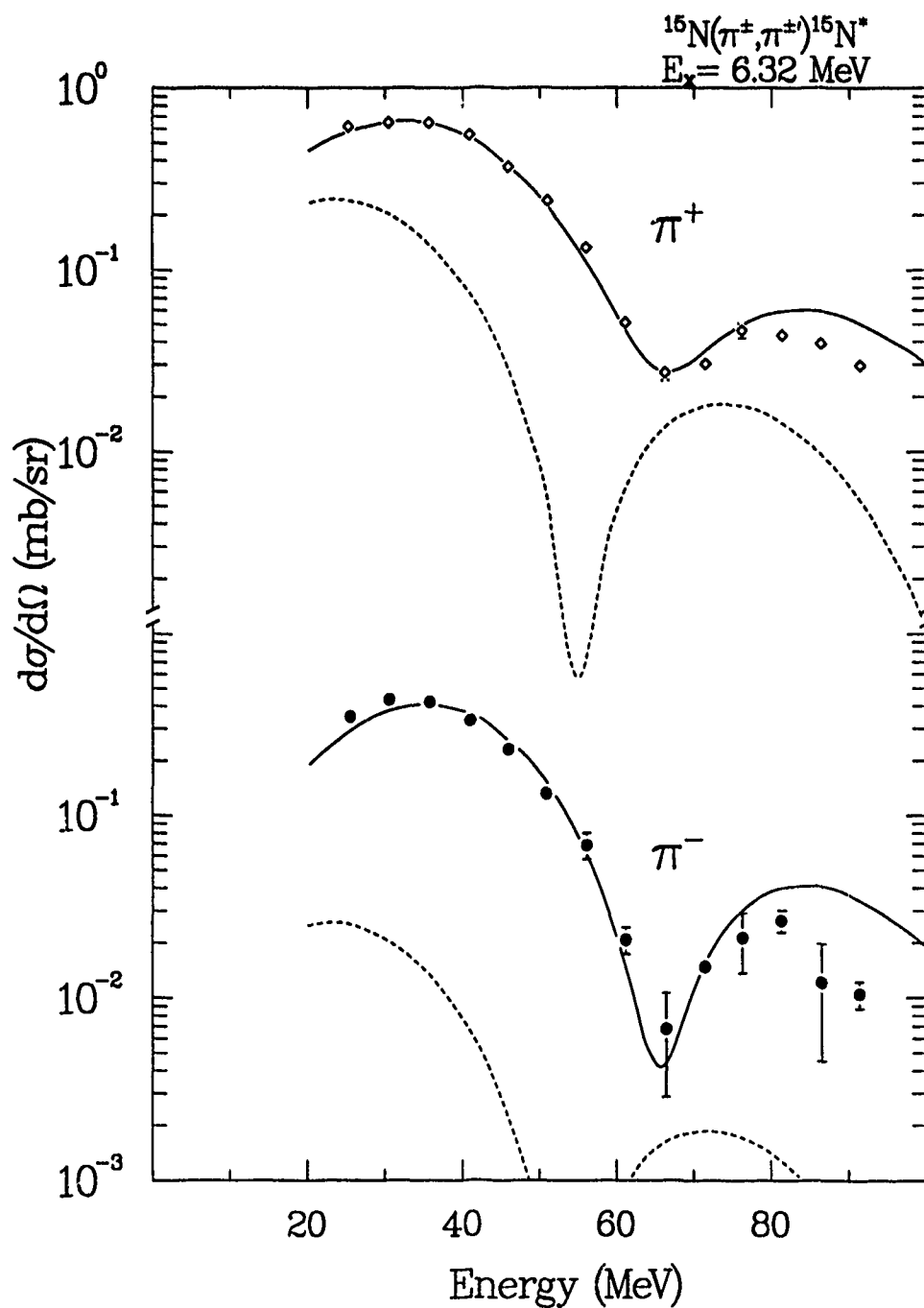


Figure 4.21: Calculations along with data for the negative parity "single hole" state at 6.32 MeV.

## Chapter 5

### Summary

Experimental data on pion elastic and inelastic scattering from  $^{15}\text{N}$  were presented. Microscopic and macroscopic DWIA calculations were also presented, and were shown to predict the data reasonably well. The microscopic calculations describe the  $J=5/2$  and  $7/2$  states very well (though calculations seemed lacking in their representation of  $J=3/2$  states as can be seen in their description of the 7.30 and 8.57 MeV states). Nonetheless, the shell model predicts some states that are more neutron or proton dominated than we observe. Effective charge enhancements applied here make the shell model calculations of  $\sigma_{\pi+}$  and  $\sigma_{\pi-}$  more equal, and allow the predictions to closely match the experimental data. These isoscalar and isovector effective charges were found to be  $\delta_0=0.72$  and  $\delta_1=-0.29$ , respectively, to enhance the  $\Delta J=\Delta L=3$ , (non spin-flip),  $\Delta T=0$  and  $\Delta T=1$  portions of the transitions to these states. The complementary use of  $\frac{\sigma(\pi^+)}{\sigma(\pi^-)}$  ratio comparison, shell model descriptions of the nucleus, collective enhancements to the shell model states, and purely macroscopic calculations allow us to determine much about the structure of the nucleus.

Some tenuous new  $J^\pi$  identifications were made, and are included in the following list of states seen in the experimental spectrum: 0.00- ( $\frac{1}{2}^-$ ), 5.27- ( $\frac{5}{2}^+$ ), 6.32- ( $\frac{3}{2}^-$ ), 7.16- ( $\frac{5}{2}^+$ ), 7.30- ( $\frac{3}{2}^+$ ), 7.57- ( $\frac{7}{2}^+$ ), 8.31- ( $\frac{1}{2}^+$ ), 8.57-

( $\frac{3}{2}^+$ ), 9.15- ( $\frac{3}{2}^-$  and  $\frac{5}{2}^+$ ), 9.76- ( $\frac{5}{2}^-$ ), 9.93- ( $\frac{3}{2}^-$ ), 10.69-( $\frac{9}{2}^+$ ), 11.29(11.24)- (possible  $\frac{7}{2}$ ), 11.88- ( $\frac{3}{2}^-$ ), 12.49-( $\frac{9}{2}^+$ ), 12.94(12.92)- ( $\frac{3}{2}^-$ ), 13.15- (possible  $\frac{3}{2}^-$ ), 14.09-(possible  $\frac{7}{2}^+$ ), 14.38(14.24)- ( $\frac{5}{2}^+$ ), 14.65- (possible  $\frac{3}{2}^+$ ), 15.03- (possible  $\frac{5}{2}^+$ ), 16.46- (possible  $\frac{3}{2}$ ), 16.91- (possible  $\frac{3}{2}^-$ ), 17.15-(possible  $\frac{9}{2}^+$ ), 17.58- ( $\frac{3}{2}^+$ ), 18.27- (possible  $\frac{3}{2}$ ), 18.70- (possible  $\frac{3}{2}$ ) and 18.91- ( $\frac{3}{2}+\frac{1}{2}$ ). (The energies given here are those at which the states were analyzed, and when there are two different energies, the one in parentheses is the energy of the known state with which the state in the present data is identified.) An evaluation of the simple model of low lying states being split into  $T_h=1,0$  pairs[OS82] is also made. It appears that the  $T_h$  model is too simple, that collective effects or other more involved shell model effects complicate the picture too much for the model to be of use at all, since its only success is with the lowest energy  $^{15}\text{N}$  excited state, a  $5/2^+$  state, and the next highest energy  $5/2^+$  state.

The  $\frac{\sigma(\pi^+)}{\sigma(\pi^-)}$  ratios, constant momentum transfer excitation functions, and angular distribution shapes were instrumental in the identification of transitions which contained significant M4 strength. These states were found at 10.7, 12.5, 14.1, and 17.2 MeV. Spectroscopic amplitudes were extracted for these states, and they were in reasonable agreement with the amplitudes extracted from electron scattering. Shell model calculations performed with a  $1\hbar\omega$  basis produced only one low energy  $\frac{3}{2}^+$  state. A  $(1+3)\hbar\omega$  basis was required to reproduce the two experimentally observed states at low energy. The need for this  $(1+3)\hbar\omega$  basis indicates that 3p-4h components are present in these states, and it is thought that the lowest 1p-2h and 3p-4h states mix to form the experimentally observed states at 10.7 and 12.5 MeV.

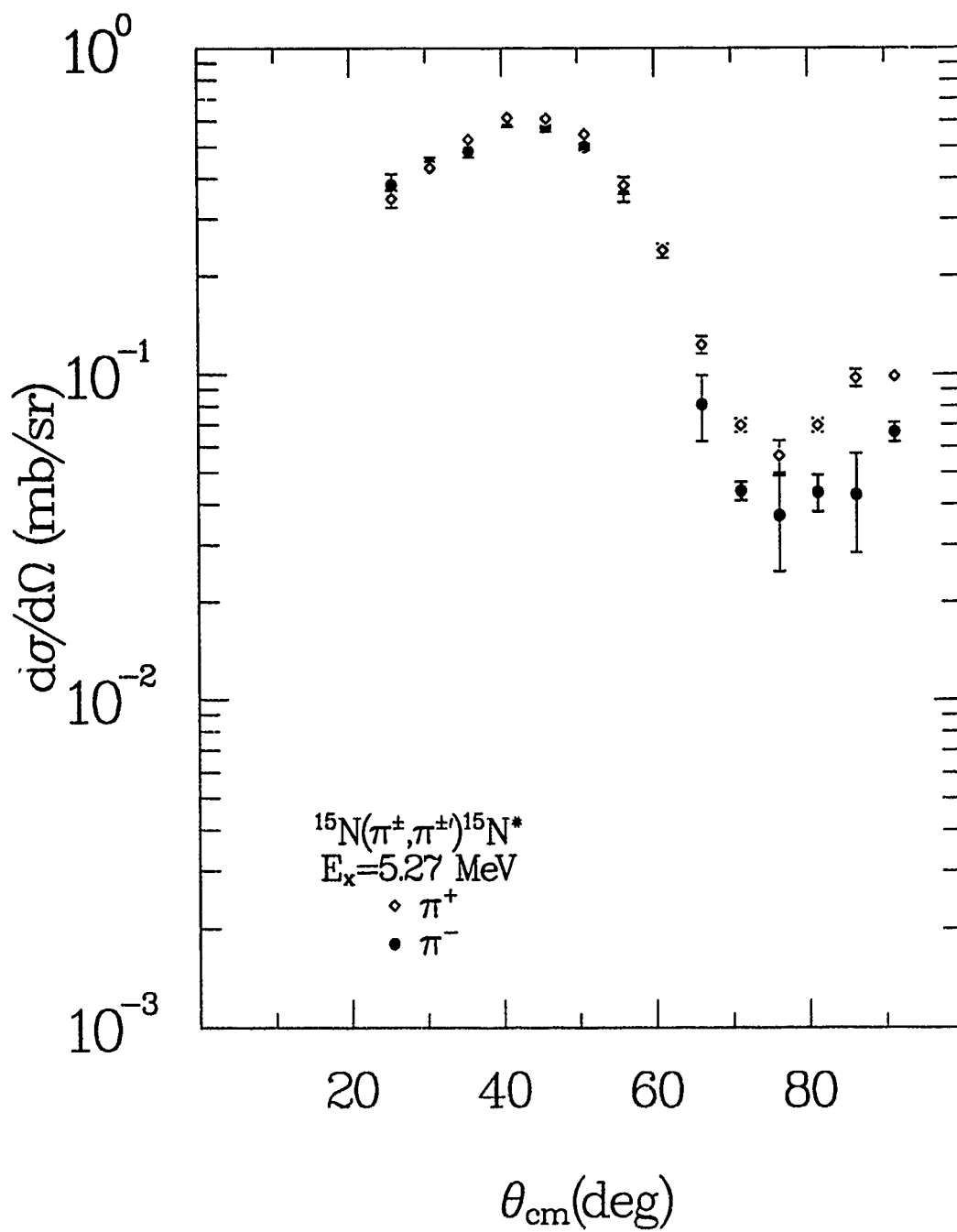
Finally, both macroscopic and microscopic calculations for the single

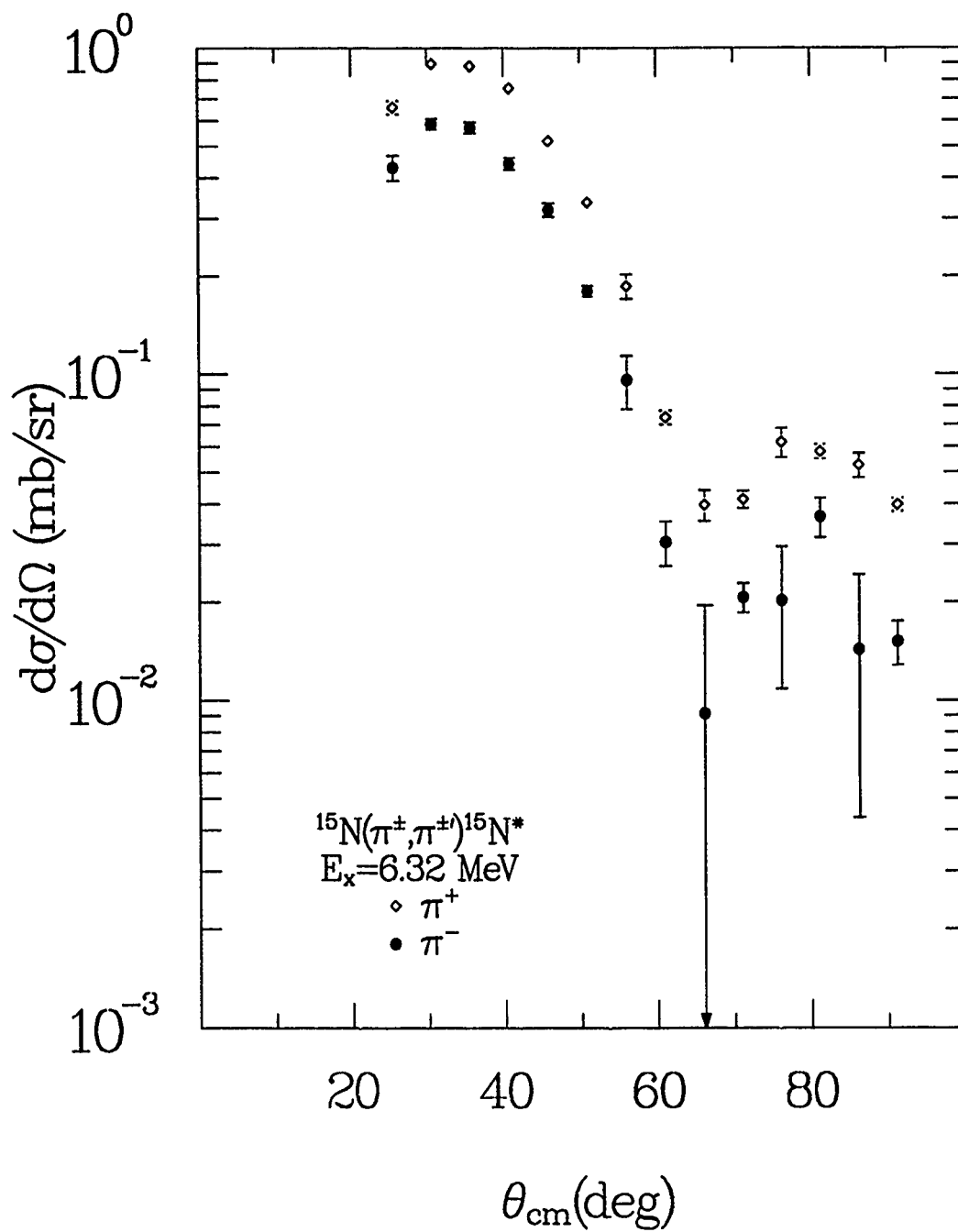


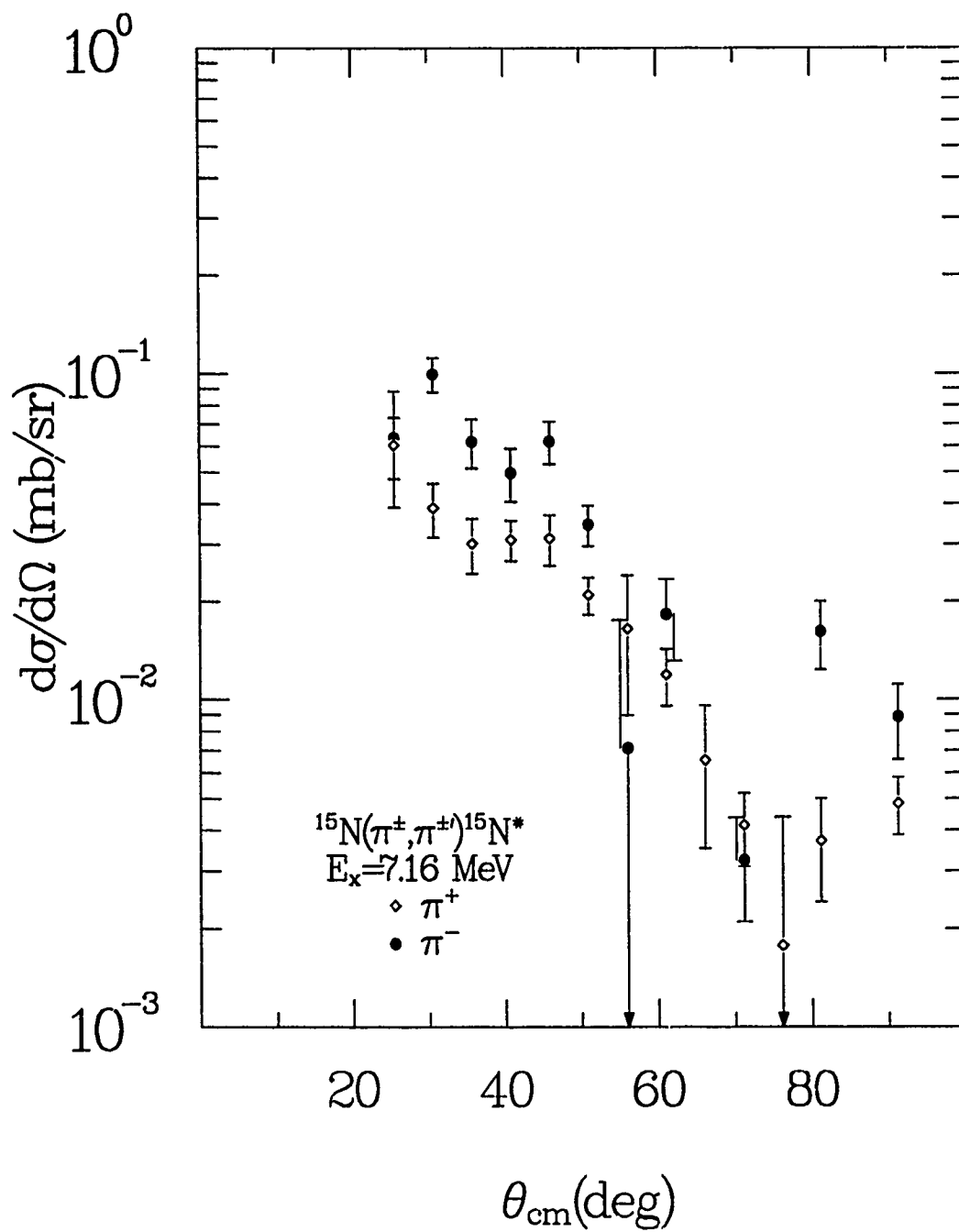
hole negative parity state at 6.32 MeV were performed. The  $\frac{\sigma(\pi^+)}{\sigma(\pi^-)}$  ratio was 1.78, contrary to the extreme shell model predictions that this state should be completely proton dominated and have a  $\frac{\sigma(\pi^+)}{\sigma(\pi^-)}$  ratio of 9. It was found that neutron and proton collective effective charge enhancements of  $(1 + \delta_n)$  and  $(1 + \delta_p)$ , where  $\delta_n = 0.3$  and  $\delta_p = 1.0$  were necessary to appropriately enhance the angular distributions. For the rest of the negative parity states, only macroscopic calculations were performed, and these mostly reinforced the identifications found presently in the literature, although some tenuous new identifications were made.

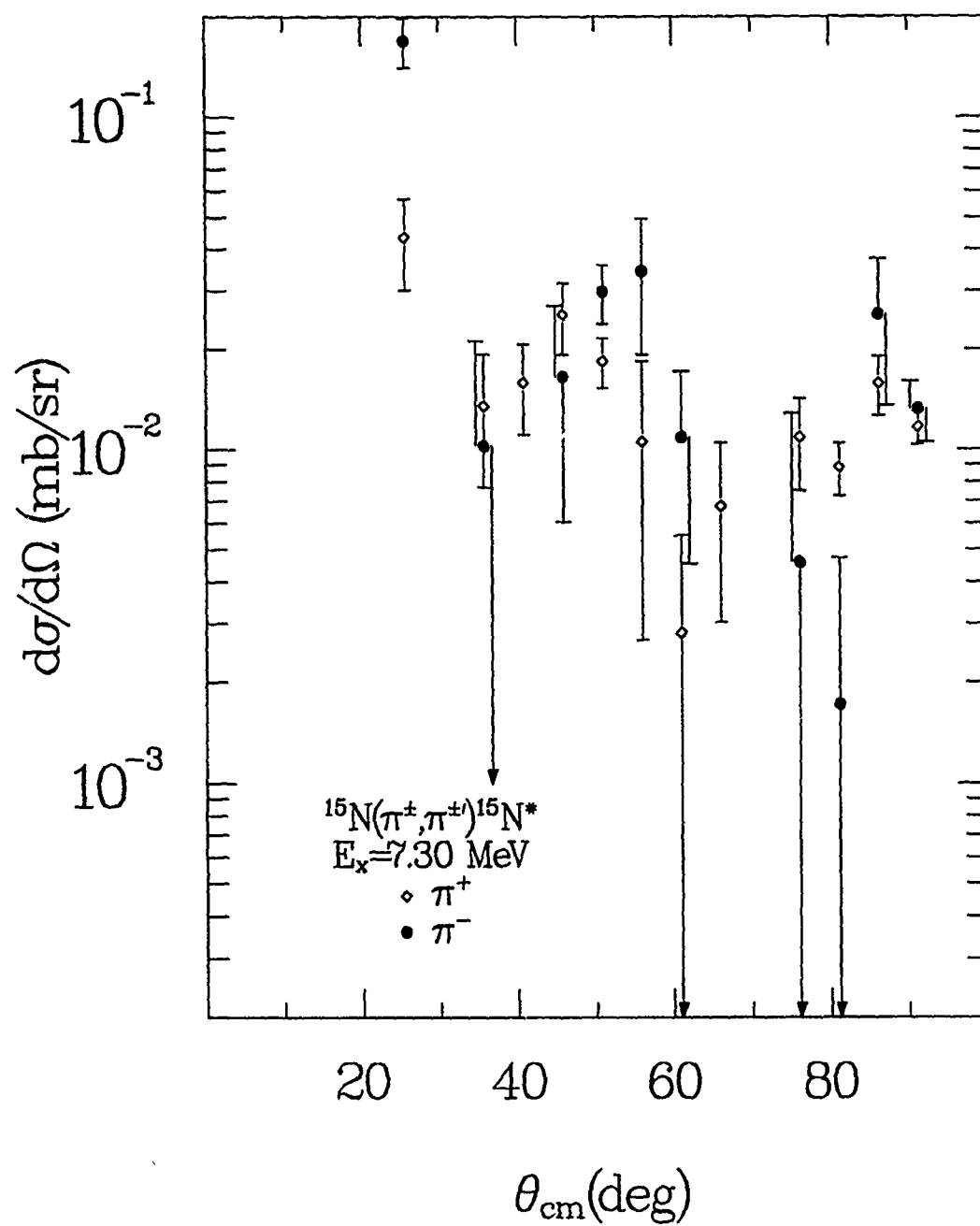
# **Appendix A**

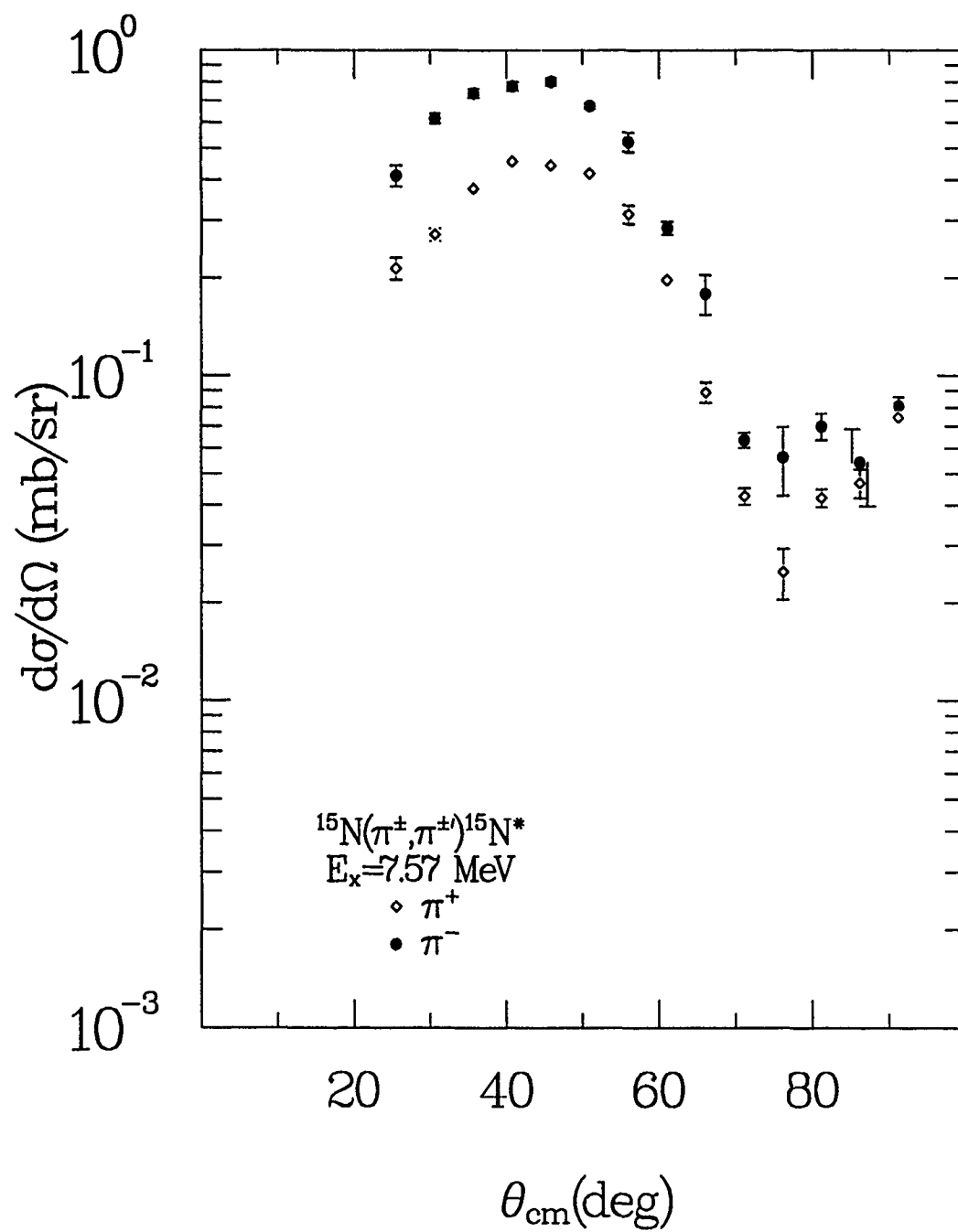
## **Experimental Data Plots**

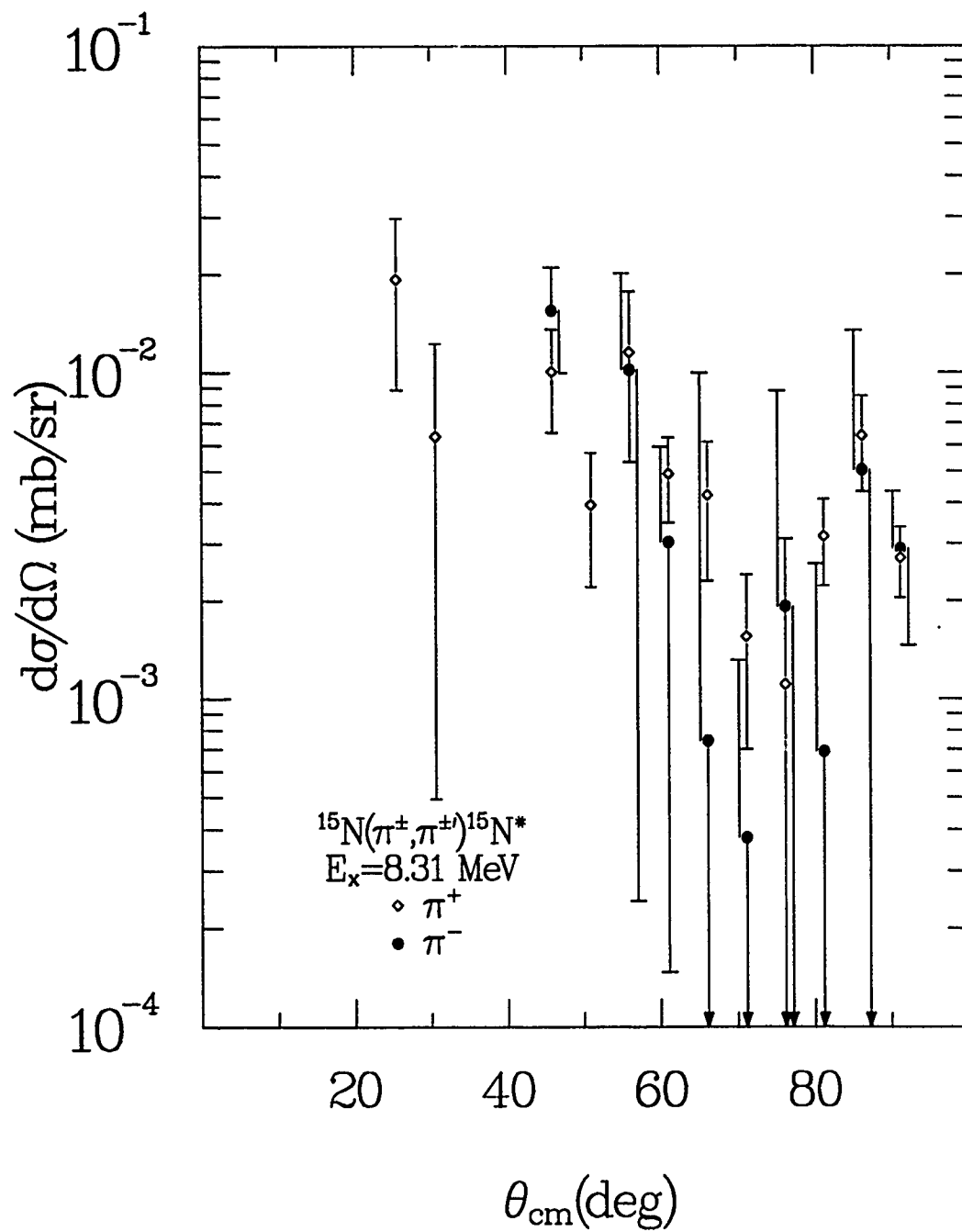




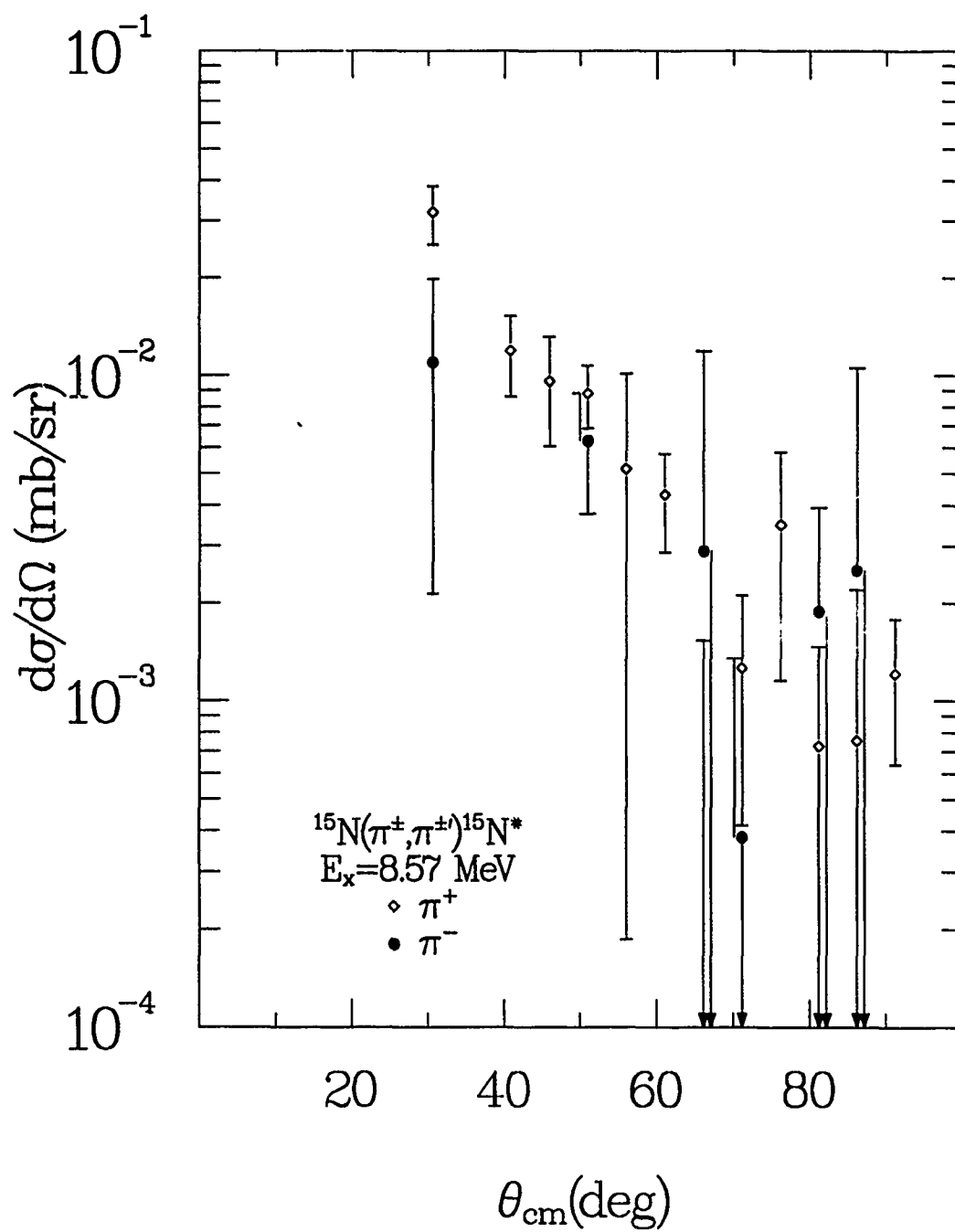


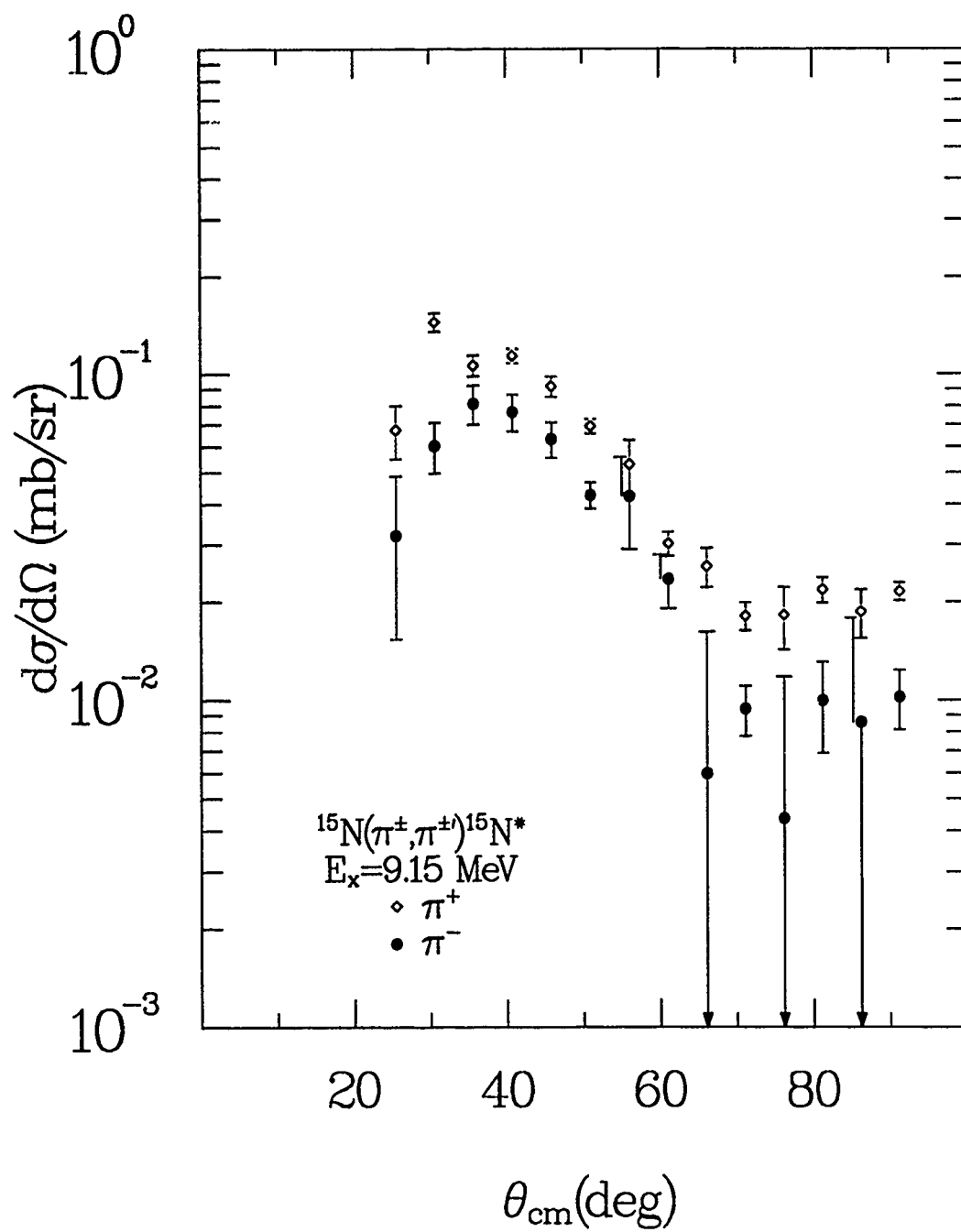


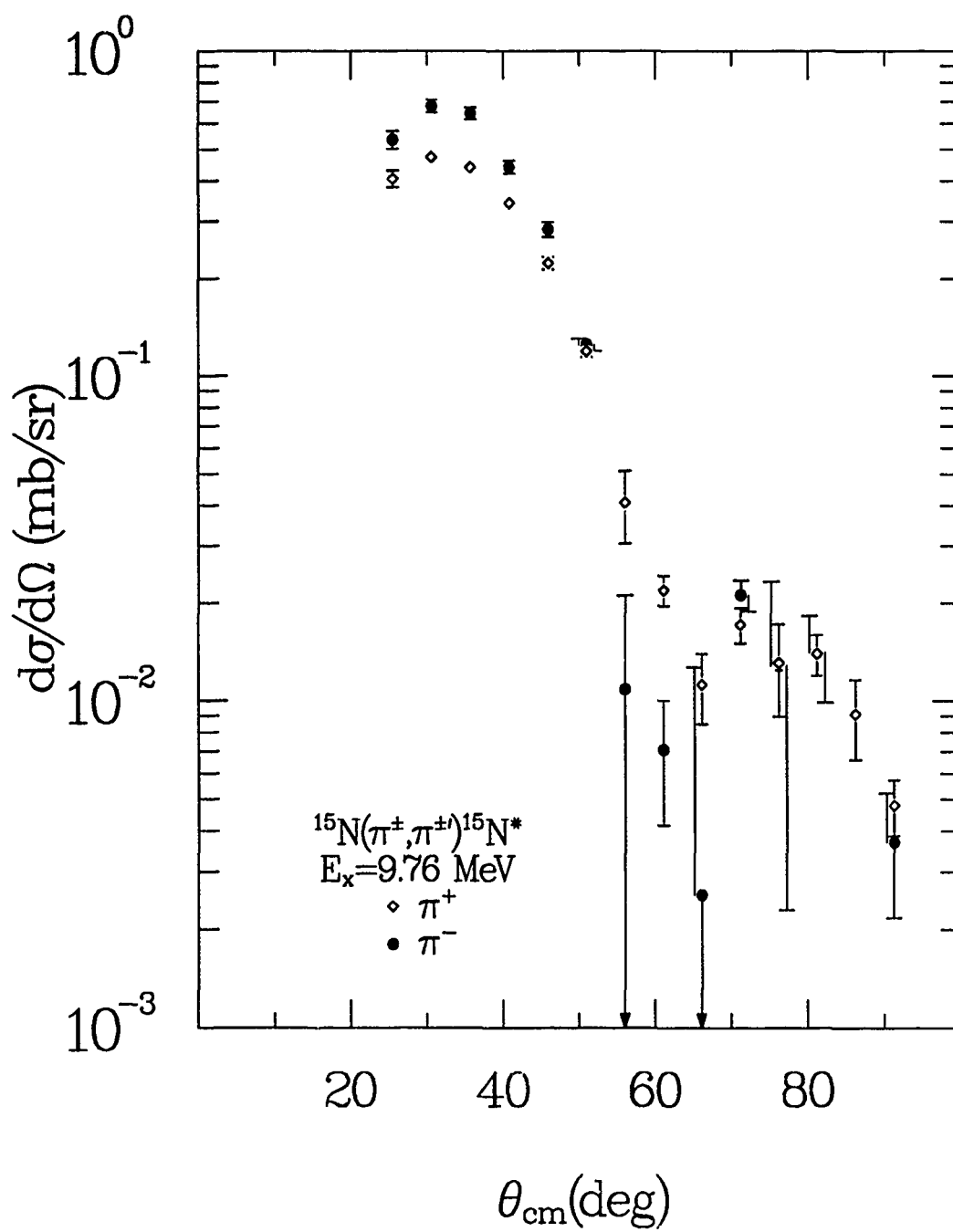


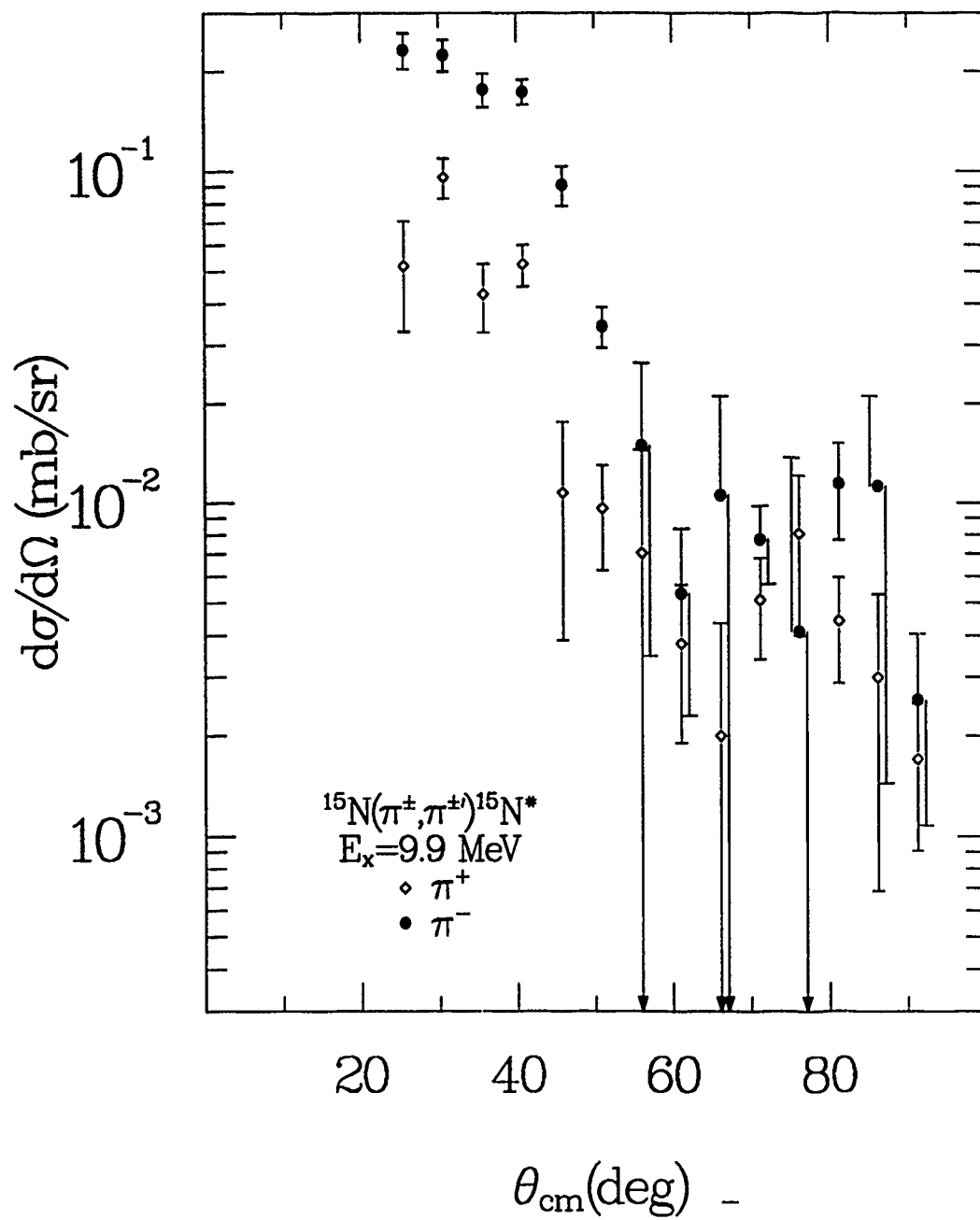


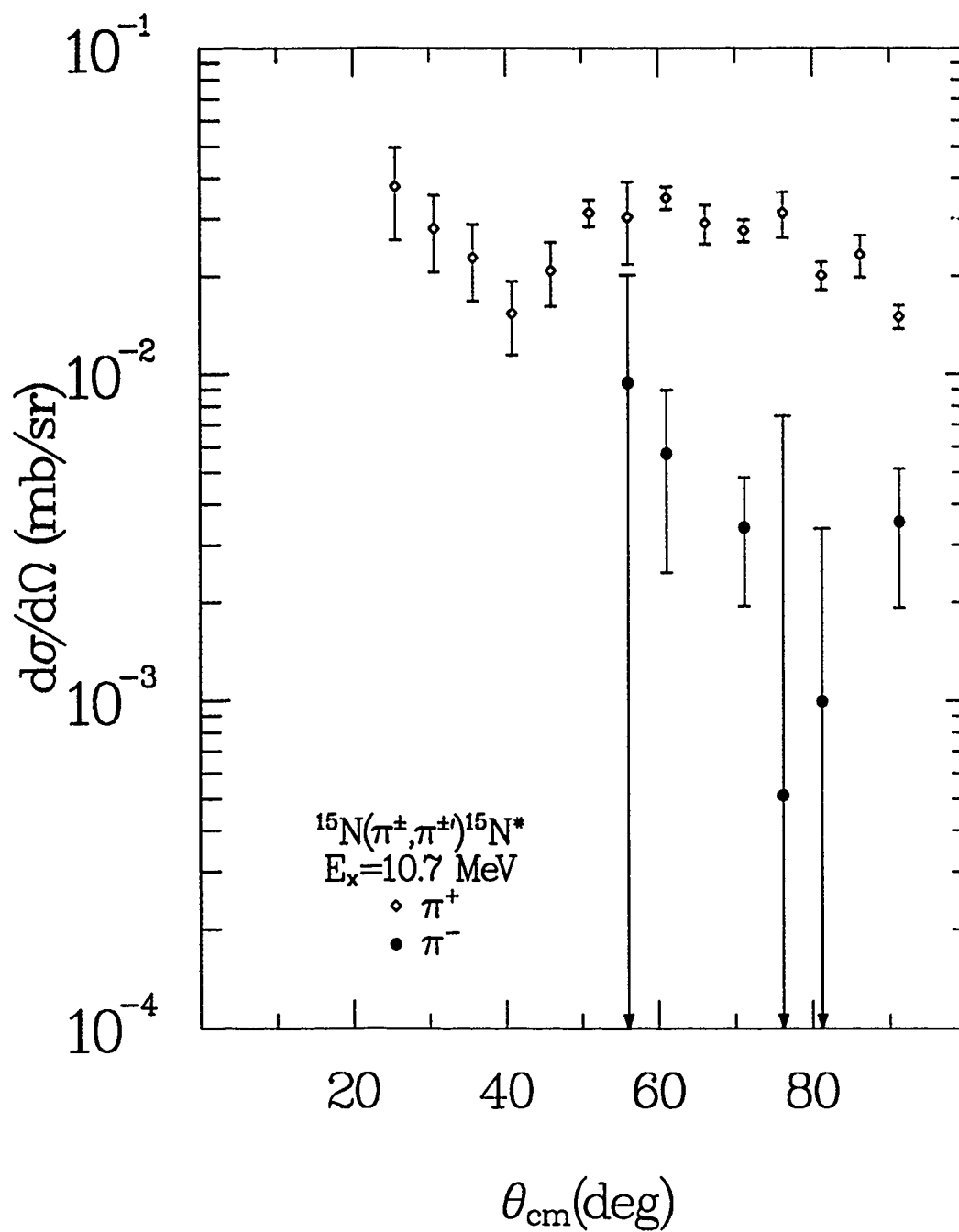


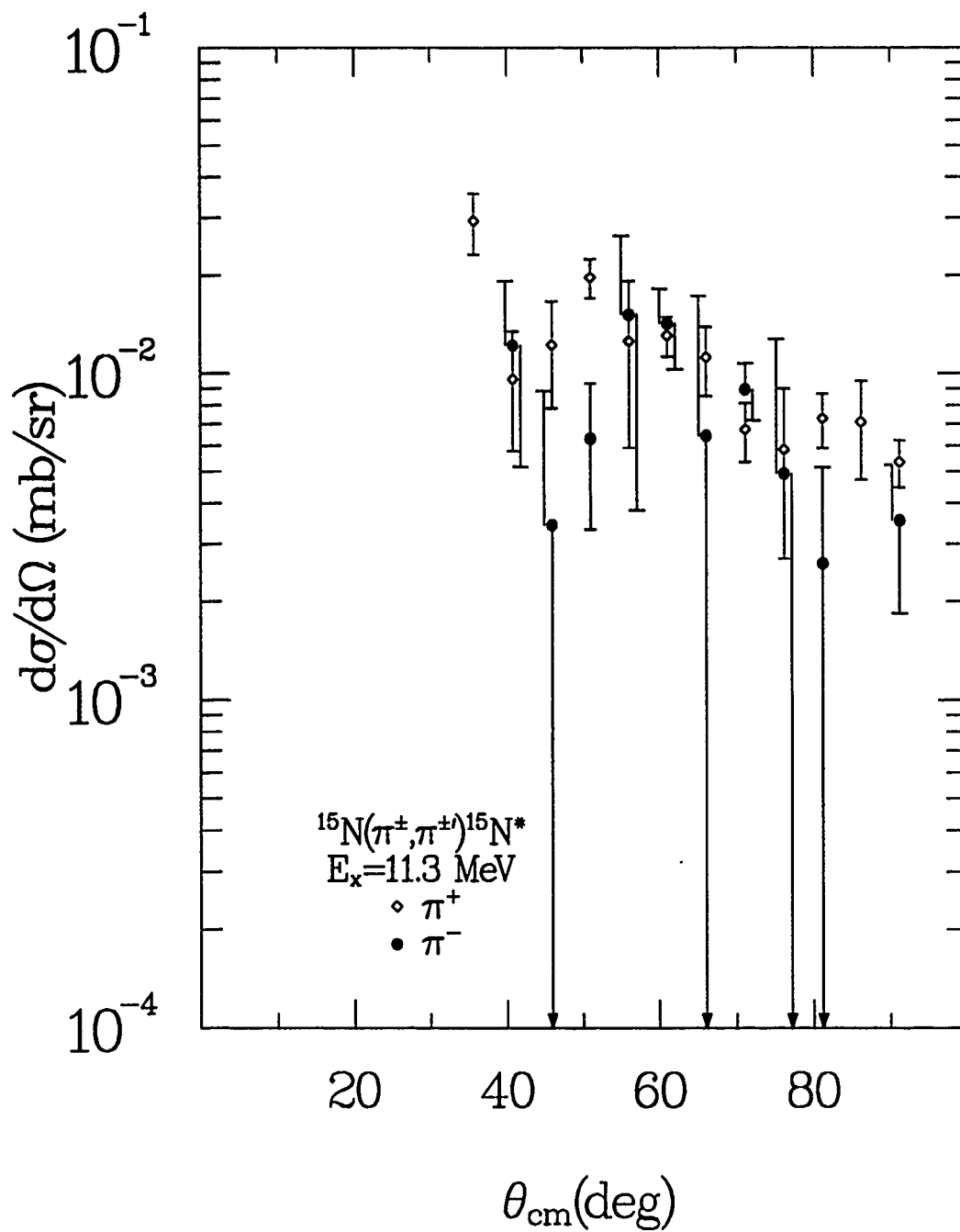


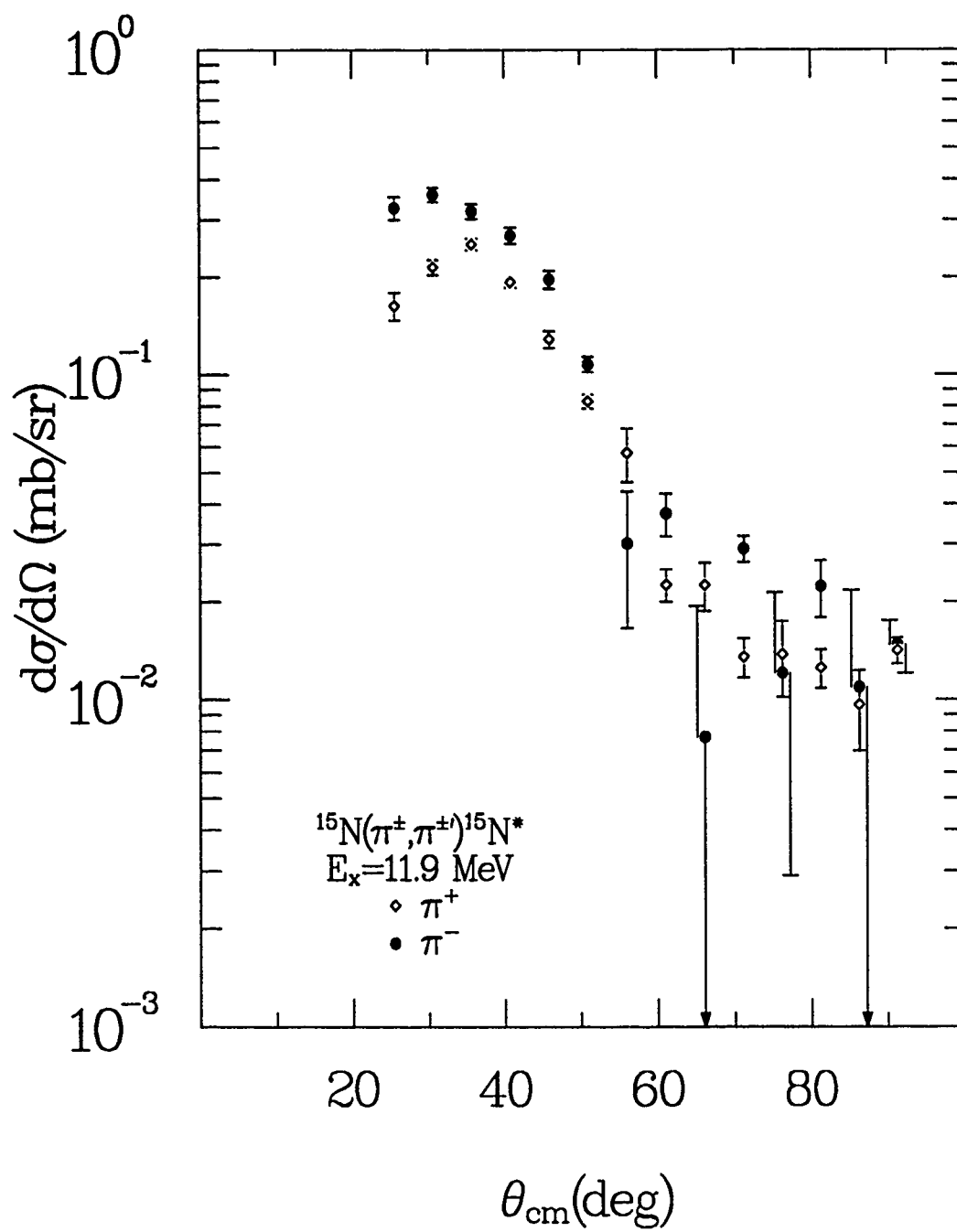


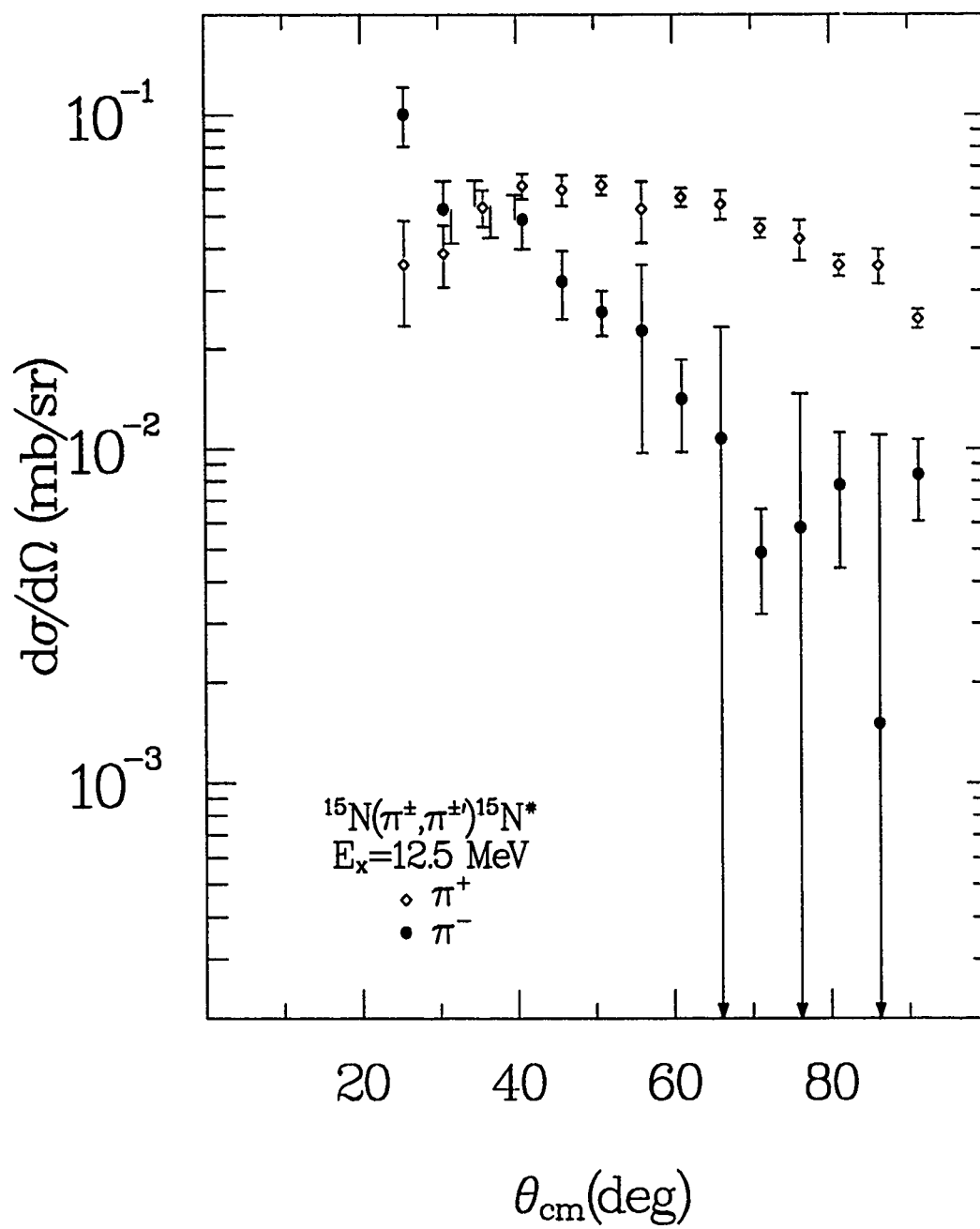




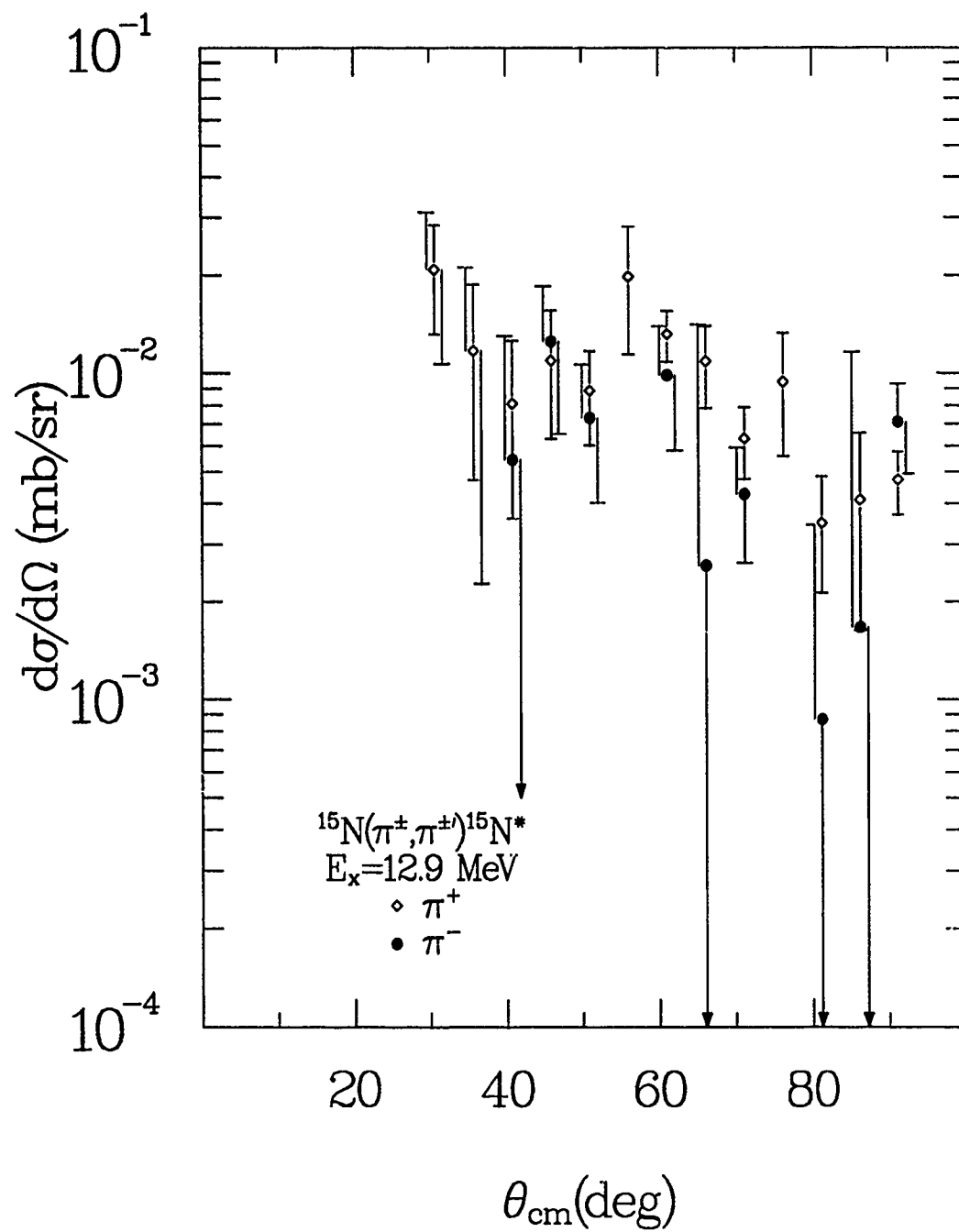


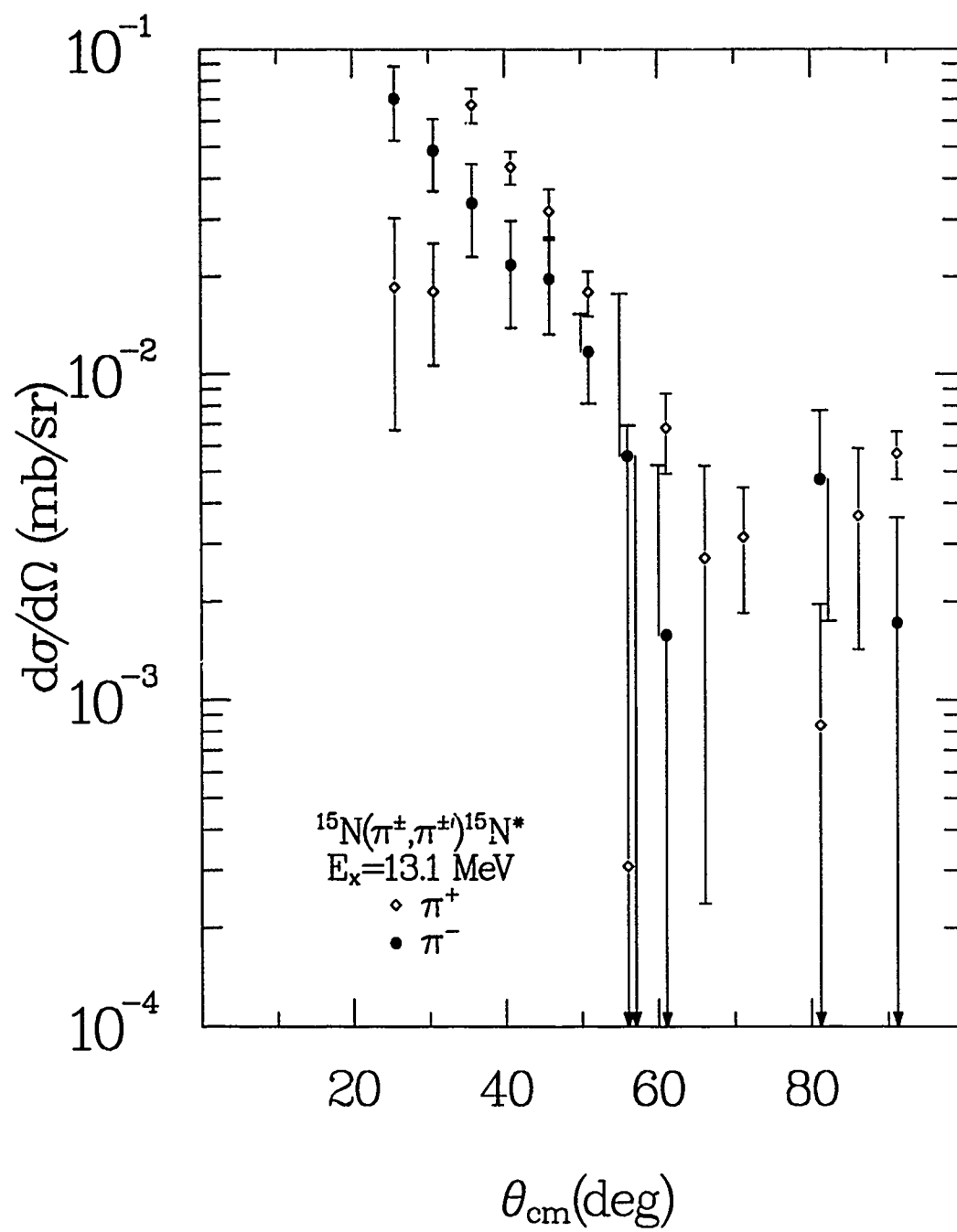


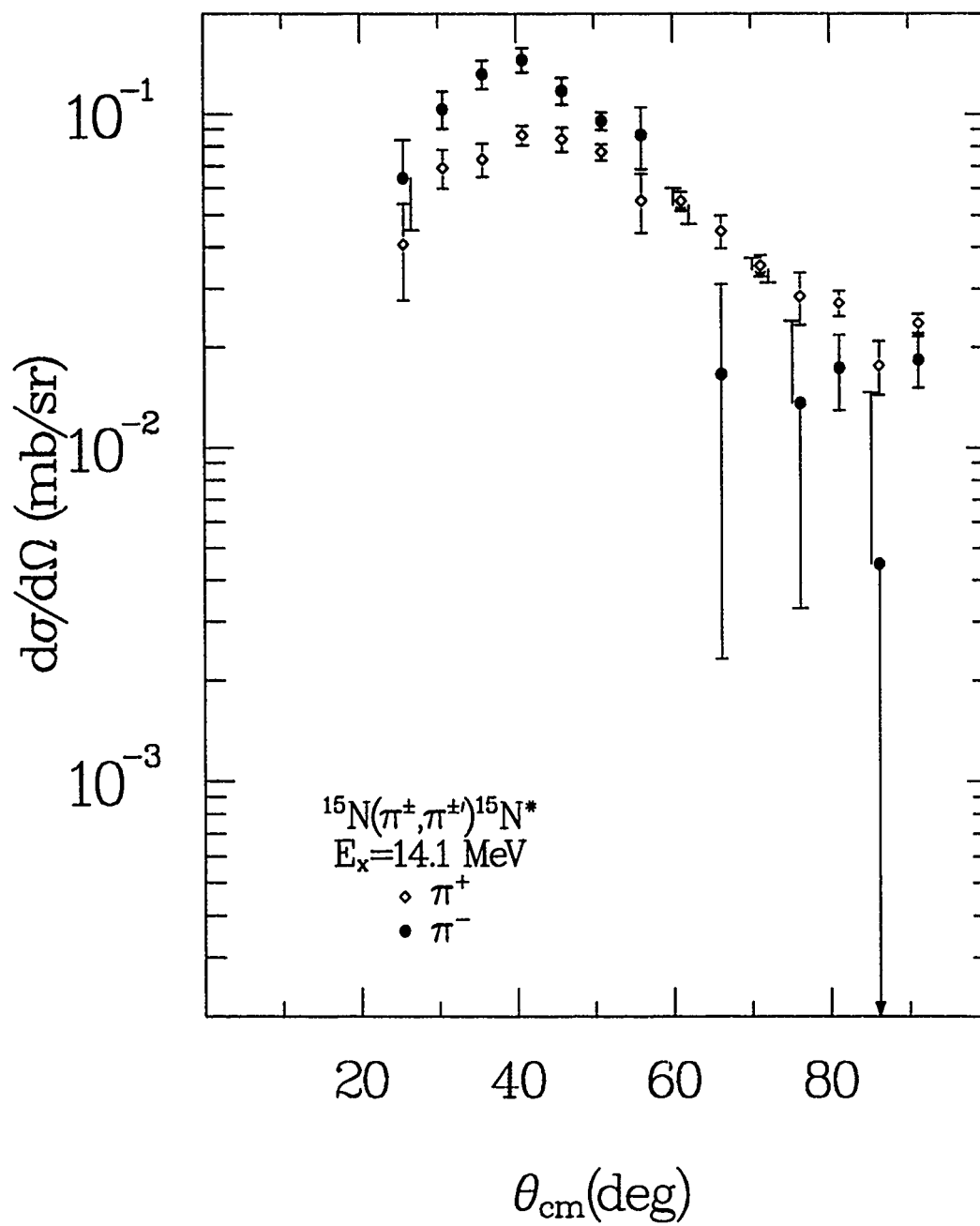


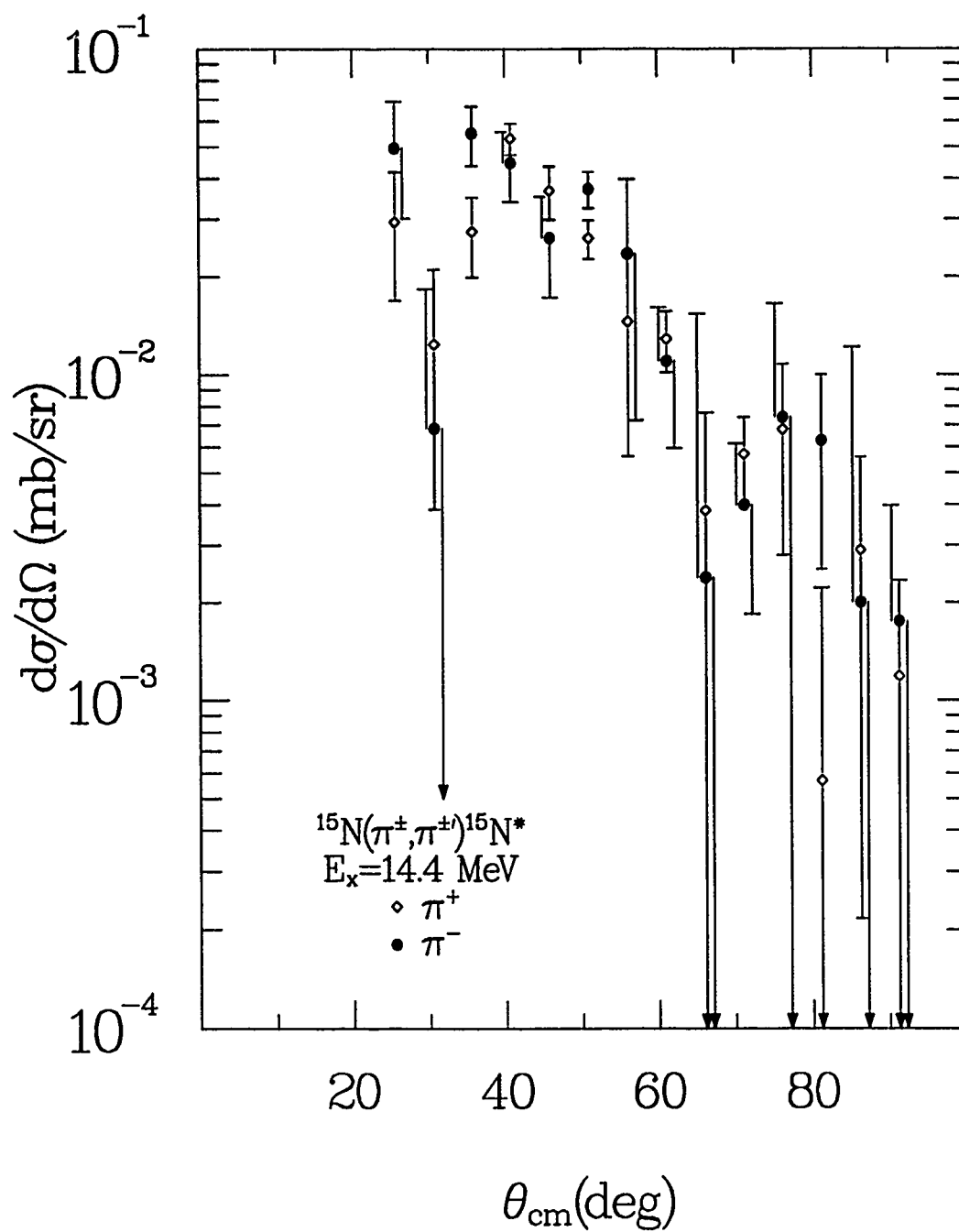


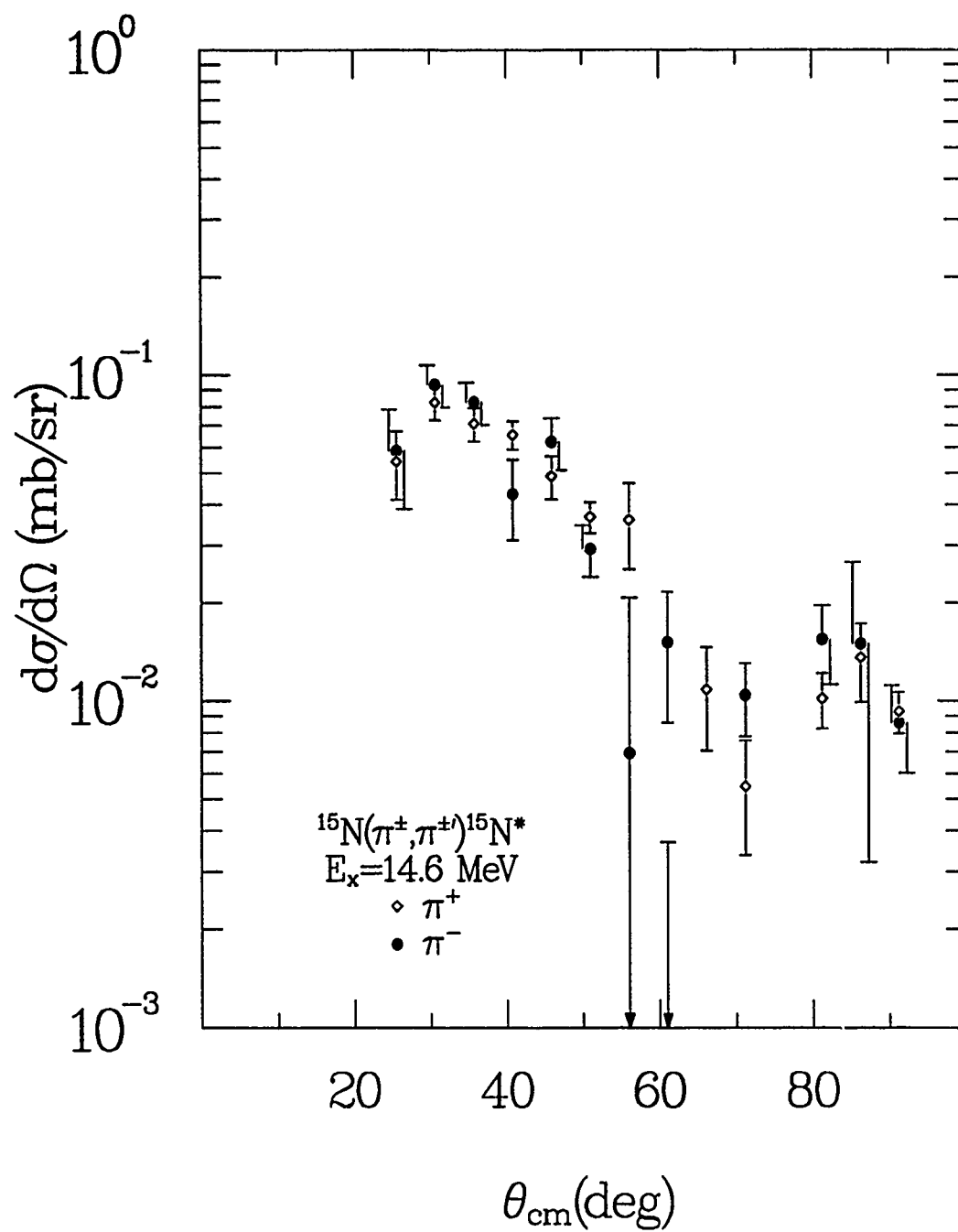


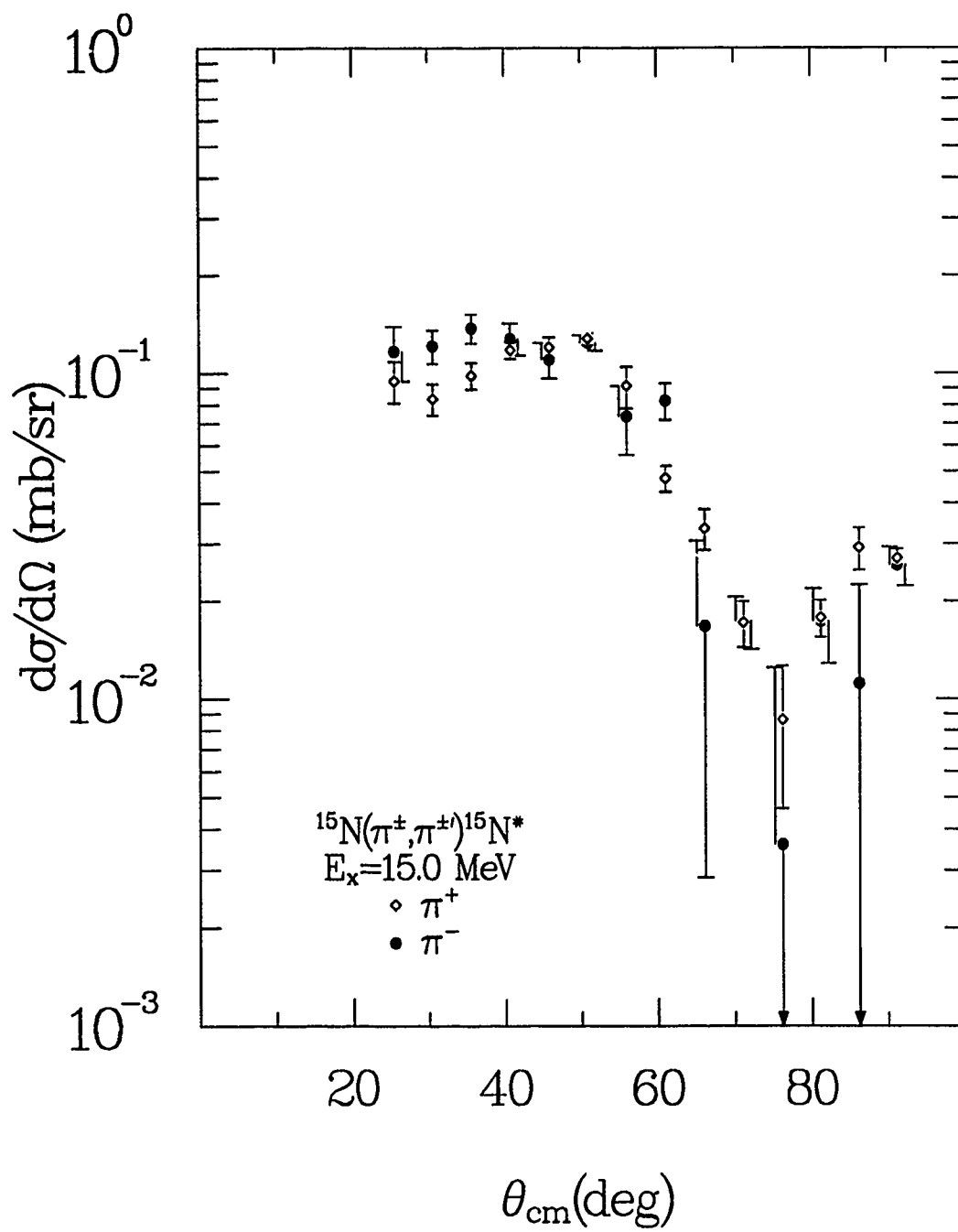


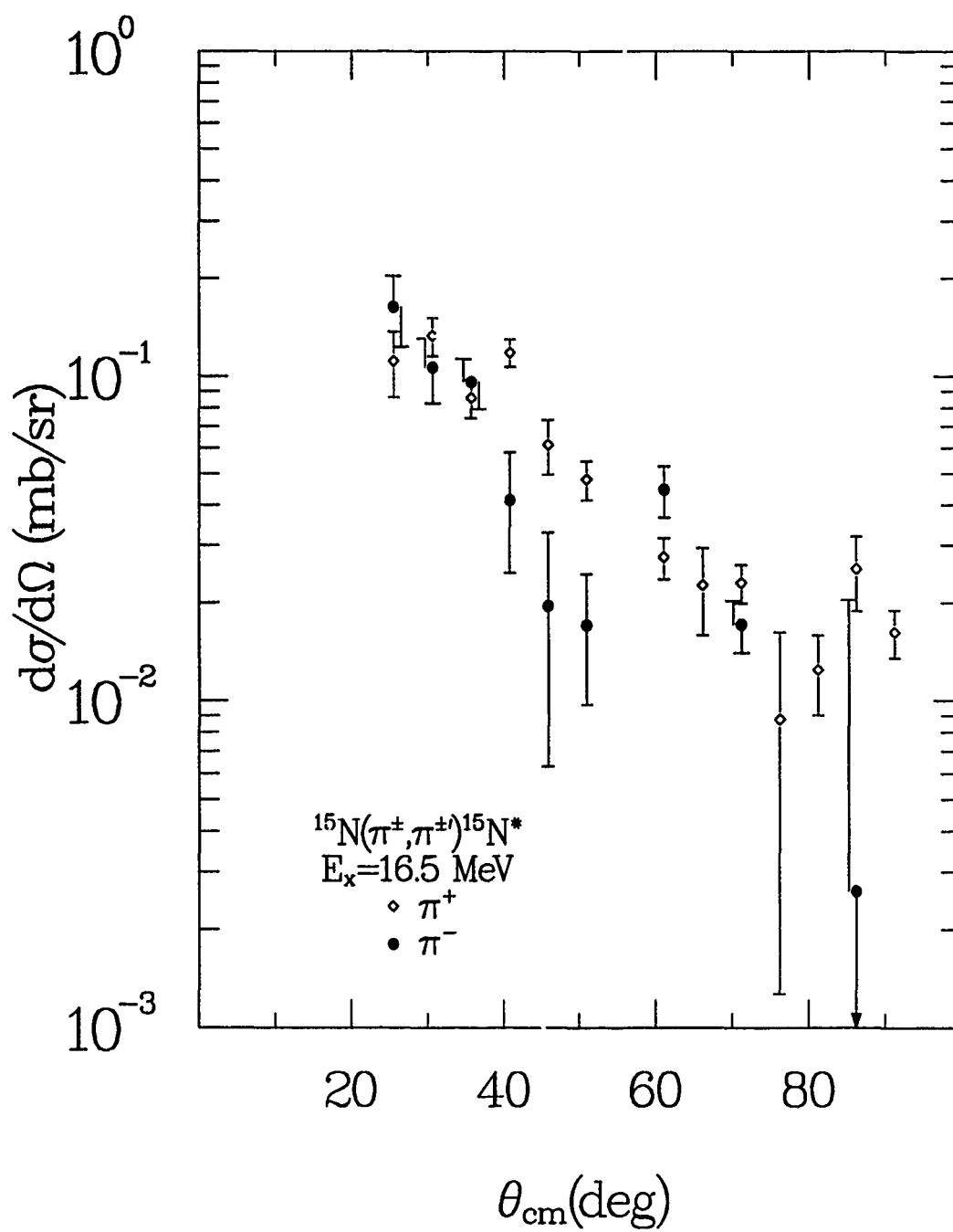


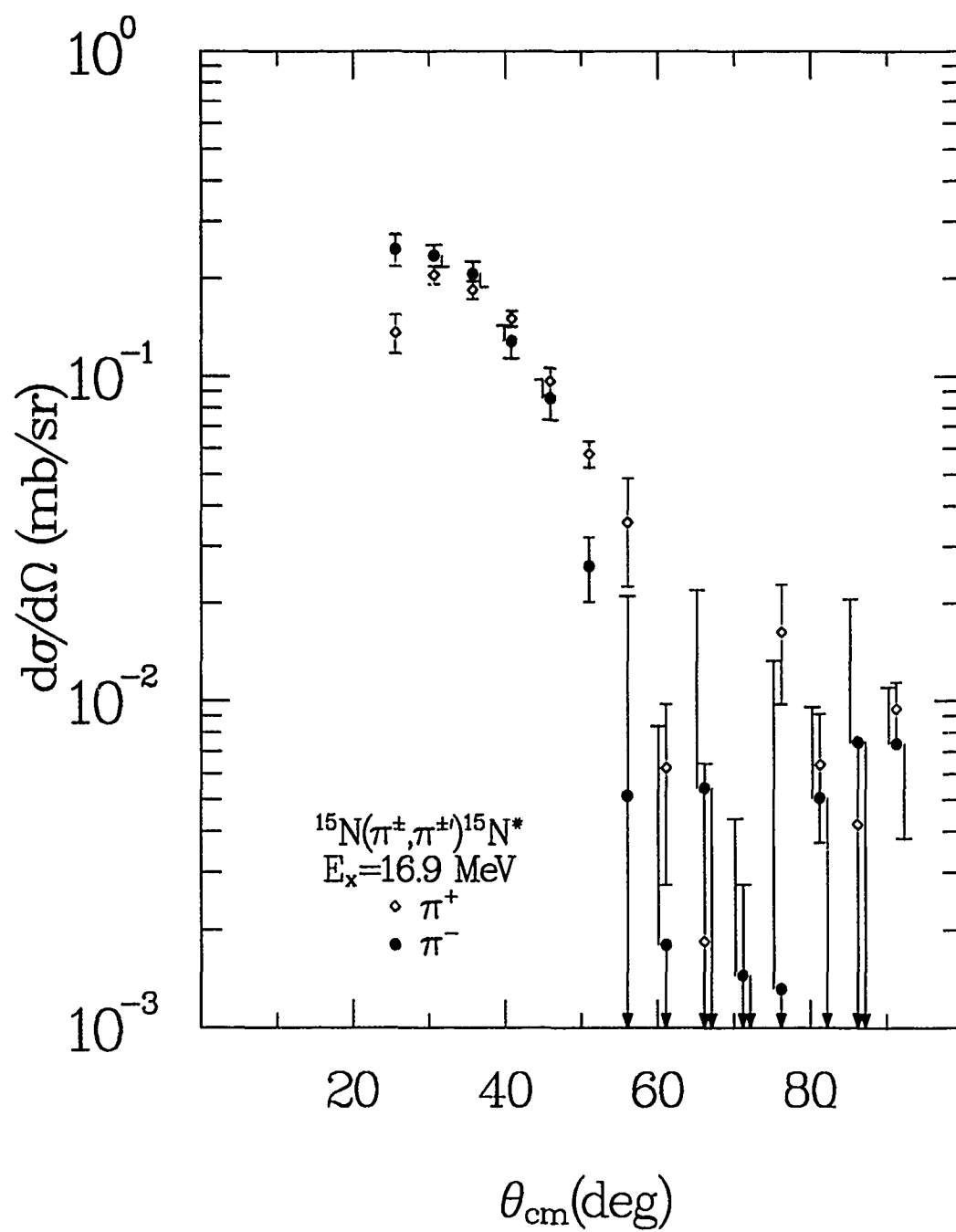




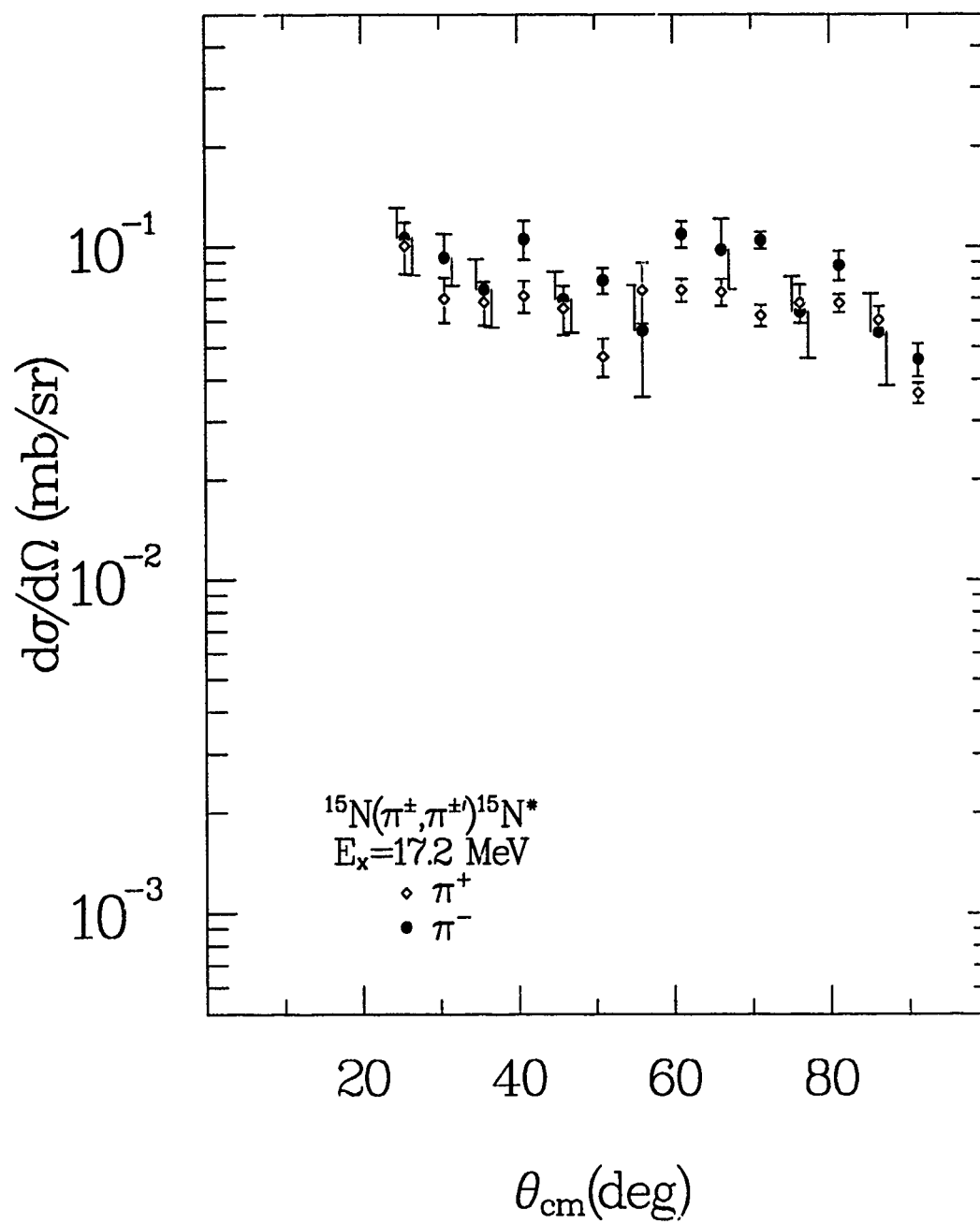


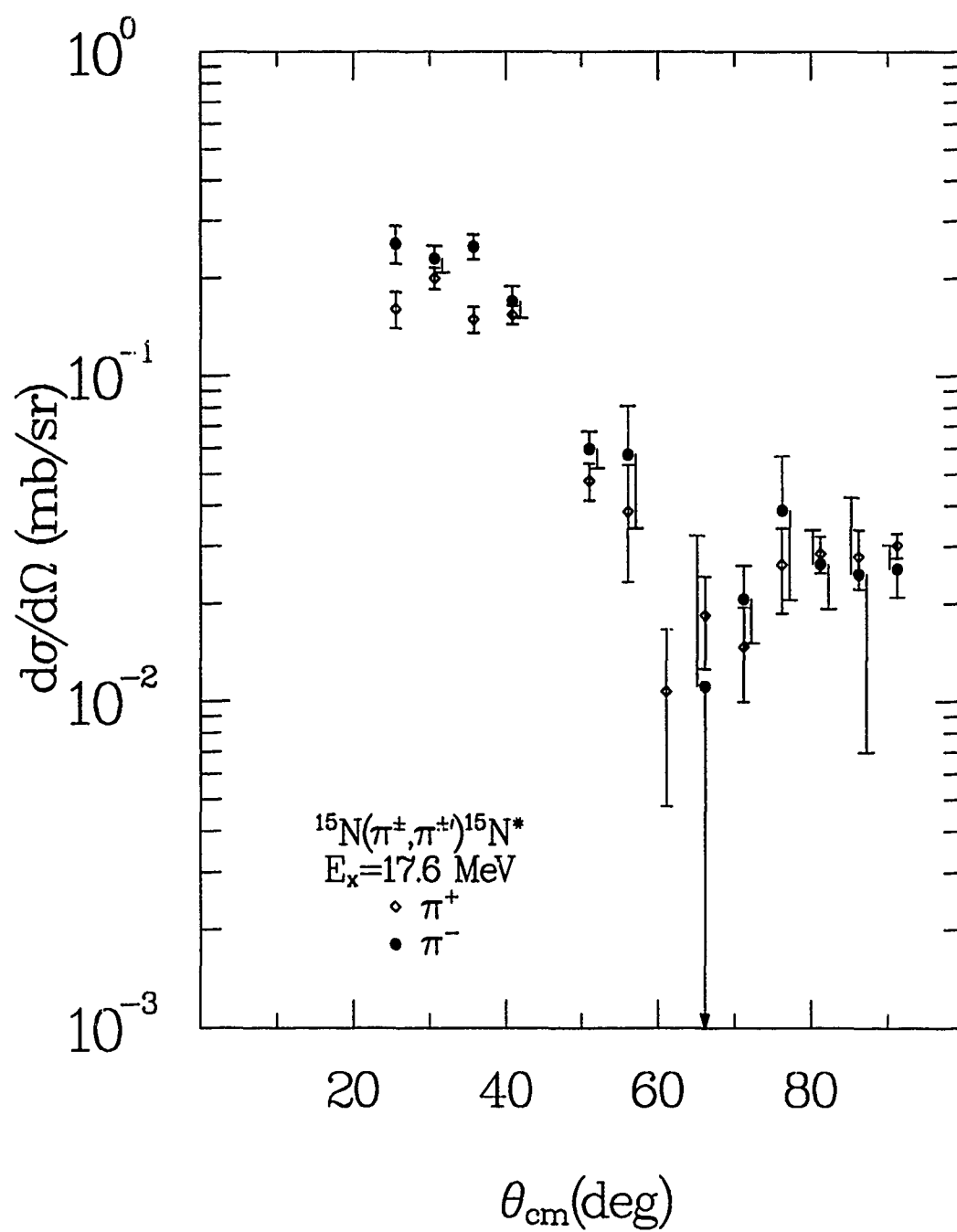


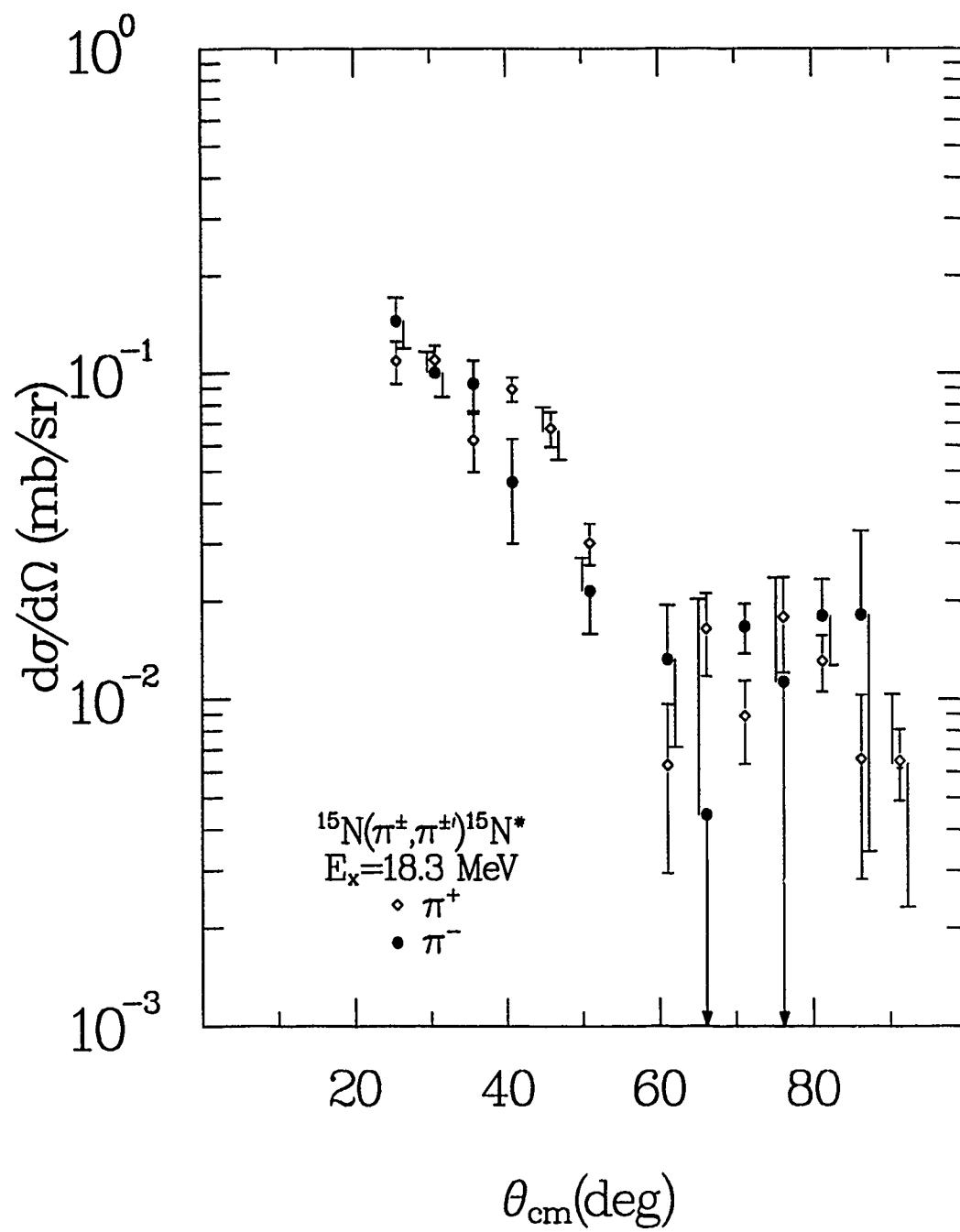


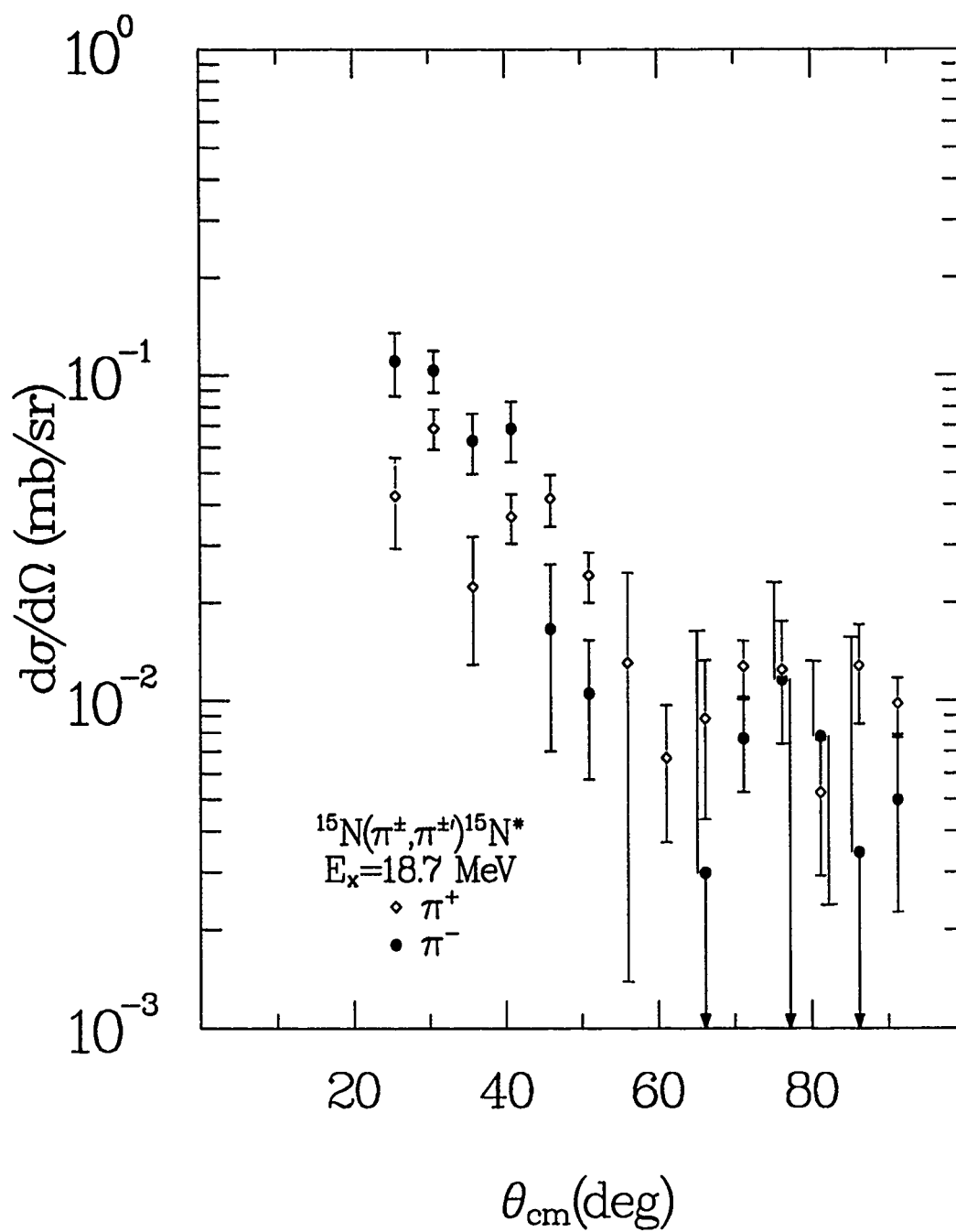


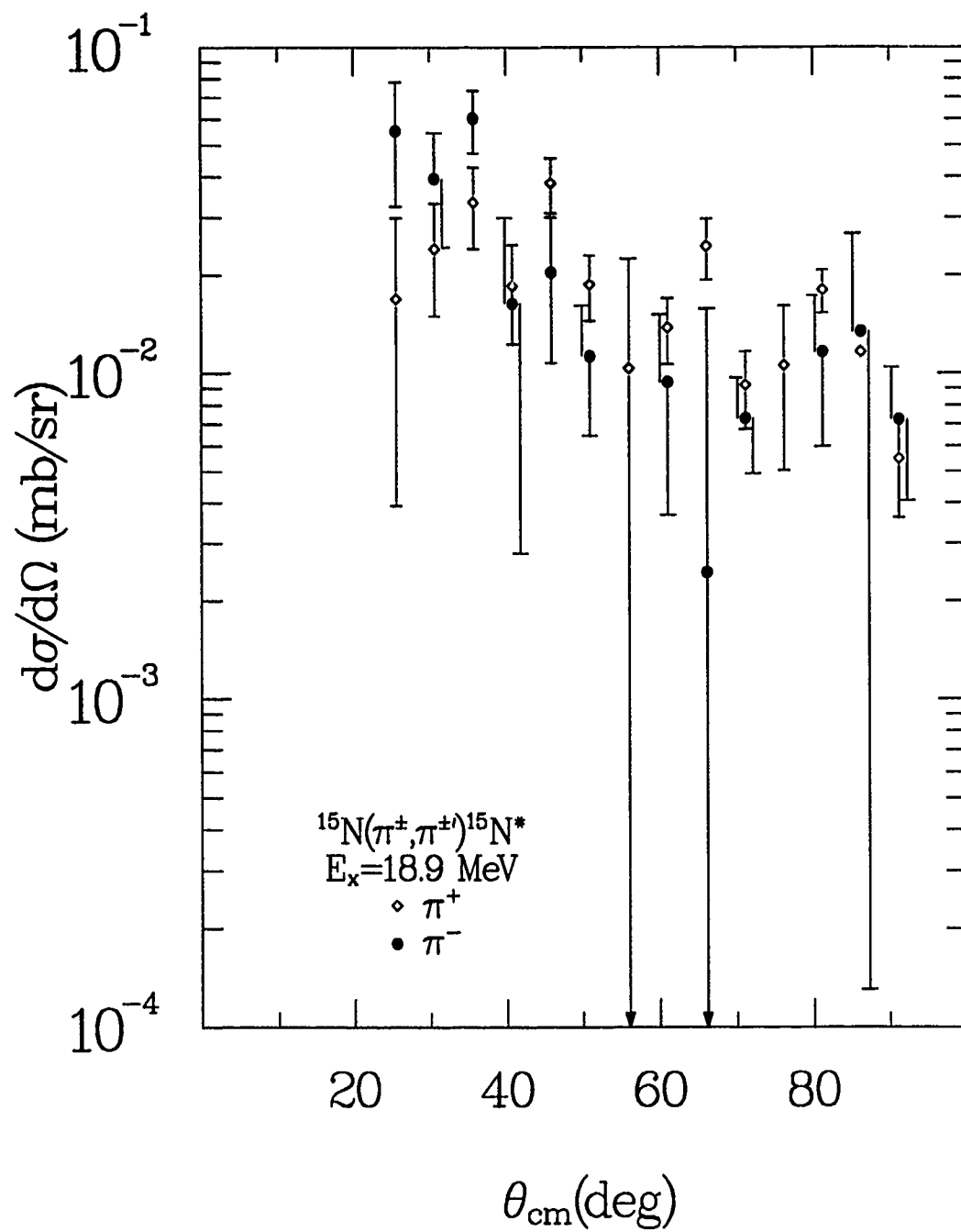












**Appendix B**  
**Tabulated Data**

0.00 MeV (Elastic)  $\pi^\pm$  tabulated data

	$\theta_{\text{cm}}$ (deg)	$\frac{d\sigma}{d\omega}$ (mb/sr)	error (mb/sr)
$\pi^+$			
	25.52	0.1789E+03	0.2843E+01
	30.62	0.8647E+02	0.3274E+00
	35.71	0.3234E+02	0.1121E+00
	40.79	0.9625E+01	0.4958E-01
	45.87	0.1082E+01	0.2168E-01
	50.94	0.3421E+00	0.8070E-02
	56.01	0.1414E+01	0.4652E-01
	61.07	0.2160E+01	0.2063E-01
	66.11	0.2024E+01	0.3033E-01
	71.15	0.1458E+01	0.1543E-01
	76.19	0.7613E+00	0.2260E-01
	81.21	0.2671E+00	0.6673E-02
	86.22	0.8064E-01	0.5922E-02
	91.22	0.7055E-01	0.2468E-02
$\pi^-$			
	25.52	0.1858E+03	0.1805E+01
	30.62	0.8261E+02	0.2860E+00
	35.71	0.2907E+02	0.1602E+00
	40.79	0.6846E+01	0.7764E-01
	45.87	0.5873E+00	0.2178E-01
	50.94	0.9418E+00	0.1671E-01
	56.01	0.2252E+01	0.8038E-01
	61.07	0.2847E+01	0.4225E-01
	66.11	0.2424E+01	0.8978E-01
	71.15	0.1464E+01	0.1666E-01
	76.19	0.7565E+00	0.4291E-01
	81.21	0.6014E-01	0.6127E-02
	86.22	0.1145E+00	0.1824E-01
	91.22	0.1178E+00	0.6158E-02

5.27 MeV  $\pi^\pm$  tabulated data

	$\theta_{\text{cm}}$ (deg)	$\frac{d\sigma}{d\omega}$ (mb/sr)	error (mb/sr)
$\pi^+$			
	25.53	0.3464E+00	0.2091E-01
	30.62	0.4312E+00	0.1487E-01
	35.71	0.5264E+00	0.1422E-01
	40.80	0.6136E+00	0.1182E-01
	45.88	0.6094E+00	0.1522E-01
	50.95	0.5469E+00	0.9067E-02
	56.02	0.3805E+00	0.2321E-01
	61.08	0.2404E+00	0.6566E-02
	66.12	0.1232E+00	0.7366E-02
	71.17	0.6969E-01	0.3271E-02
	76.20	0.5621E-01	0.6416E-02
	81.22	0.6975E-01	0.3237E-02
	86.23	0.9747E-01	0.6048E-02
	91.24	0.9868E-01	0.2817E-02
$\pi^-$			
	25.53	0.3821E+00	0.3039E-01
	30.62	0.4435E+00	0.2064E-01
	35.71	0.4861E+00	0.2122E-01
	40.80	0.5983E+00	0.2170E-01
	45.88	0.5766E+00	0.2002E-01
	50.95	0.5008E+00	0.1122E-01
	56.02	0.3703E+00	0.3242E-01
	61.08	0.2396E+00	0.1196E-01
	66.12	0.8082E-01	0.1852E-01
	71.17	0.4385E-01	0.2917E-02
	76.20	0.3687E-01	0.1205E-01
	81.22	0.4342E-01	0.5574E-02
	86.23	0.4272E-01	0.1433E-01
	91.24	0.6651E-01	0.4605E-02



6.32 MeV  $\pi^\pm$  tabulated data

	$\theta_{\text{cm}}$ (deg)	$\frac{d\sigma}{d\omega}$ (mb/sr)	error (mb/sr)
$\pi^+$			
	25.53	0.6591E+00	0.3161E-01
	30.62	0.8950E+00	0.1982E-01
	35.71	0.8818E+00	0.1742E-01
	40.80	0.7543E+00	0.1250E-01
	45.88	0.5182E+00	0.1379E-01
	50.95	0.3362E+00	0.7062E-02
	56.02	0.1859E+00	0.1622E-01
	61.08	0.7375E-01	0.3671E-02
	66.12	0.3965E-01	0.4301E-02
	71.17	0.4128E-01	0.2516E-02
	76.20	0.6181E-01	0.6440E-02
	81.22	0.5786E-01	0.2958E-02
	86.23	0.5256E-01	0.4622E-02
	91.24	0.3974E-01	0.1805E-02
$\pi^-$			
	25.53	0.4299E+00	0.3783E-01
	30.62	0.5851E+00	0.2199E-01
	35.71	0.5703E+00	0.2220E-01
	40.80	0.4421E+00	0.1895E-01
	45.88	0.3188E+00	0.1501E-01
	50.95	0.1799E+00	0.6900E-02
	56.02	0.9589E-01	0.1776E-01
	61.08	0.3053E-01	0.4744E-02
	66.12	0.9123E-02	0.1041E-01
	71.17	0.2066E-01	0.2129E-02
	76.20	0.2020E-01	0.9353E-02
	81.22	0.3651E-01	0.5044E-02
	86.23	0.1431E-01	0.9935E-02
	91.24	0.1515E-01	0.2332E-02

7.16 MeV  $\pi^\pm$  tabulated data

	$\theta_{\text{cm}}$ (deg)	$\frac{d\sigma}{d\omega}$ (mb/sr)	error (mb/sr)
$\pi^+$			
	25.53	0.6042E-01	0.1279E-01
	30.62	0.3881E-01	0.7342E-02
	35.71	0.3014E-01	0.5775E-02
	40.80	0.3105E-01	0.4398E-02
	45.88	0.3132E-01	0.5567E-02
	50.95	0.2094E-01	0.2725E-02
	56.02	0.1649E-01	0.7537E-02
	61.08	0.1192E-01	0.2352E-02
	66.12	0.6549E-02	0.3032E-02
	71.17	0.4138E-02	0.1047E-02
	76.20	0.1775E-02	0.2613E-02
	81.22	0.3703E-02	0.1291E-02
	91.24	0.4840E-02	0.9693E-03
$\pi^-$			
	25.53	0.6370E-01	0.2465E-01
	30.62	0.9974E-01	0.1198E-01
	35.71	0.6188E-01	0.1056E-01
	40.80	0.4977E-01	0.9150E-02
	45.88	0.6202E-01	0.9275E-02
	50.95	0.3455E-01	0.4884E-02
	56.02	0.7120E-02	0.1043E-01
	61.08	0.1828E-01	0.5130E-02
	71.17	0.3229E-02	0.1137E-02
	81.22	0.1615E-01	0.3844E-02
	91.24	0.8862E-02	0.2271E-02

7.30 MeV  $\pi^\pm$  tabulated data

	$\theta_{\text{cm}}$ (deg)	$\frac{d\sigma}{d\omega}$ (mb/sr)	error (mb/sr)
$\pi^+$			
	25.53	0.4357E-01	0.1345E-01
	35.71	0.1353E-01	0.5829E-02
	40.80	0.1592E-01	0.4838E-02
	45.88	0.2547E-01	0.6196E-02
	50.95	0.1846E-01	0.3146E-02
	56.02	0.1056E-01	0.7879E-02
	61.08	0.2815E-02	0.2702E-02
	66.12	0.6747E-02	0.3715E-02
	76.20	0.1089E-01	0.3362E-02
	81.22	0.8841E-02	0.1601E-02
	86.23	0.1584E-01	0.3207E-02
	91.24	0.1168E-01	0.1324E-02
$\pi^-$			
	25.53	0.1690E+00	0.2867E-01
	35.71	0.1027E-01	0.1099E-01
	45.88	0.1658E-01	0.1052E-01
	50.95	0.2990E-01	0.5997E-02
	56.02	0.3447E-01	0.1517E-01
	61.08	0.1088E-01	0.6344E-02
	76.20	0.4581E-02	0.8287E-02
	81.22	0.1715E-02	0.3007E-02
	86.23	0.2553E-01	0.1196E-01
	91.24	0.1327E-01	0.2757E-02

7.57 MeV  $\pi^\pm$  tabulated data

	$\theta_{\text{cm}}$ (deg)	$\frac{d\sigma}{d\omega}$ (mb/sr)	error (mb/sr)
$\pi^+$			
	25.53	0.2142E+00	0.1652E-01
	30.62	0.2715E+00	0.1182E-01
	35.71	0.3765E+00	0.1177E-01
	40.80	0.4560E+00	0.1008E-01
	45.88	0.4433E+00	0.1282E-01
	50.95	0.4185E+00	0.7533E-02
	56.02	0.3138E+00	0.2060E-01
	61.08	0.1974E+00	0.5787E-02
	66.12	0.8891E-01	0.6323E-02
	71.17	0.4255E-01	0.2493E-02
	76.20	0.2487E-01	0.4436E-02
	81.22	0.4207E-01	0.2660E-02
	86.23	0.4672E-01	0.4794E-02
	91.24	0.7462E-01	0.2449E-02
$\pi^-$			
	25.53	0.4125E+00	0.3077E-01
	30.62	0.6178E+00	0.2214E-01
	35.71	0.7393E+00	0.2394E-01
	40.80	0.7763E+00	0.2399E-01
	45.88	0.8022E+00	0.2316E-01
	50.95	0.6752E+00	0.1261E-01
	56.02	0.5230E+00	0.3583E-01
	61.08	0.2848E+00	0.1309E-01
	66.12	0.1789E+00	0.2514E-01
	71.17	0.6348E-01	0.3383E-02
	76.20	0.5616E-01	0.1347E-01
	81.22	0.6998E-01	0.6538E-02
	86.23	0.5419E-01	0.1451E-01
	91.24	0.8085E-01	0.5193E-02

8.31 MeV  $\pi^\pm$  tabulated data

	$\theta_{\text{cm}}$ (deg)	$\frac{d\sigma}{d\omega}$ (mb/sr)	error (mb/sr)
$\pi^+$			
	25.53	0.1930E-01	0.1044E-01
	30.62	0.6376E-02	0.5882E-02
	45.88	0.1005E-01	0.3510E-02
	50.95	0.3939E-02	0.1737E-02
	56.02	0.1152E-01	0.6188E-02
	61.08	0.4903E-02	0.1431E-02
	66.12	0.4216E-02	0.1916E-02
	71.17	0.1551E-02	0.8509E-03
	76.20	0.1105E-02	0.1997E-02
	81.22	0.3155E-02	0.9353E-03
	86.23	0.6402E-02	0.2076E-02
	91.24	0.2705E-02	0.6663E-03
$\pi^-$			
	45.88	0.1549E-01	0.5533E-02
	56.02	0.1019E-01	0.9948E-02
	61.08	0.3031E-02	0.2884E-02
	66.12	0.7426E-03	0.9214E-02
	71.17	0.3778E-03	0.9359E-03
	76.20	0.1918E-02	0.6873E-02
	81.22	0.6889E-03	0.1911E-02
	86.23	0.5036E-02	0.8409E-02
	91.24	0.2893E-02	0.1435E-02

8.57 MeV  $\pi^\pm$  tabulated data

	$\theta_{\text{cm}}$ (deg)	$\frac{d\sigma}{d\omega}$ (mb/sr)	error (mb/sr)
$\pi^+$			
	30.62	0.3191E-01	0.6524E-02
	40.80	0.1193E-01	0.3340E-02
	45.88	0.9605E-02	0.3557E-02
	50.95	0.3792E-02	0.1925E-02
	56.02	0.5158E-02	0.4972E-02
	61.08	0.4305E-02	0.1433E-02
	66.12	0.3619E-04	0.1494E-02
	71.17	0.1262E-02	0.8460E-03
	76.20	0.3482E-02	0.2329E-02
	81.22	0.7267E-03	0.7398E-03
	86.23	0.7550E-03	0.1442E-02
	91.24	0.1211E-02	0.5738E-03
$\pi^-$			
	30.62	0.1099E-01	0.8858E-02
	50.95	0.6287E-02	0.2530E-02
	66.12	0.2891E-02	0.8993E-02
	71.17	0.3819E-03	0.9699E-03
	81.22	0.1884E-02	0.2042E-02
	86.23	0.2521E-02	0.8043E-02

9.15 MeV  $\pi^\pm$  tabulated data

	$\theta_{\text{cm}}$ (deg)	$\frac{d\sigma}{d\omega}$ (mb/sr)	error (mb/sr)
$\pi^+$			
	25.53	0.6742E-01	0.1252E-01
	30.62	0.1444E+00	0.9508E-02
	35.71	0.1063E+00	0.7717E-02
	40.80	0.1137E+00	0.5771E-02
	45.88	0.9170E-01	0.6521E-02
	50.95	0.6917E-01	0.3594E-02
	56.02	0.5291E-01	0.9790E-02
	61.08	0.3022E-01	0.2549E-02
	66.12	0.2573E-01	0.3552E-02
	71.17	0.1807E-01	0.1788E-02
	76.20	0.1819E-01	0.3945E-02
	81.22	0.2179E-01	0.1938E-02
	86.23	0.1862E-01	0.3165E-02
	91.24	0.2152E-01	0.1343E-02
$\pi^-$			
	25.53	0.3199E-01	0.1664E-01
	30.62	0.6029E-01	0.1060E-01
	35.71	0.8121E-01	0.1106E-01
	40.80	0.7659E-01	0.9921E-02
	45.88	0.6325E-01	0.7863E-02
	50.95	0.4257E-01	0.3938E-02
	56.02	0.4230E-01	0.1331E-01
	61.08	0.2348E-01	0.4442E-02
	66.12	0.5969E-02	0.1020E-01
	71.17	0.9399E-02	0.1648E-02
	76.20	0.4356E-02	0.7434E-02
	81.22	0.9968E-02	0.3072E-02
	86.23	0.8556E-02	0.9289E-02
	91.24	0.1022E-01	0.2098E-02

9.76 MeV  $\pi^\pm$  tabulated data

	$\theta_{\text{cm}}$ (deg)	$\frac{d\sigma}{d\omega}$ (mb/sr)	error (mb/sr)
$\pi^+$			
	25.53	0.4064E+00	0.2430E-01
	30.62	0.4738E+00	0.1687E-01
	35.71	0.4403E+00	0.1440E-01
	40.80	0.3422E+00	0.1044E-01
	45.88	0.2235E+00	0.9941E-02
	50.95	0.1194E+00	0.4954E-02
	56.02	0.4080E-01	0.1027E-01
	61.08	0.2189E-01	0.2330E-02
	66.12	0.1121E-01	0.2736E-02
	71.17	0.1712E-01	0.2133E-02
	76.20	0.1307E-01	0.4123E-02
	81.22	0.1394E-01	0.1986E-02
	86.23	0.9110E-02	0.2502E-02
	91.24	0.4793E-02	0.9312E-03
$\pi^-$			
	25.53	0.5363E+00	0.3368E-01
	30.62	0.6783E+00	0.3011E-01
	35.71	0.6440E+00	0.2592E-01
	40.80	0.4419E+00	0.1960E-01
	45.88	0.2838E+00	0.1487E-01
	50.95	0.1253E+00	0.5703E-02
	56.02	0.1086E-01	0.1022E-01
	61.08	0.7092E-02	0.2928E-02
	66.12	0.2551E-02	0.1015E-01
	71.17	0.2116E-01	0.2321E-02
	76.20	0.1279E-01	0.1050E-01
	81.22	0.1408E-01	0.4204E-02
	91.24	0.3701E-02	0.1528E-02



9.9 MeV  $\pi^\pm$  tabulated data

	$\theta_{\text{cm}}$ (deg)	$\frac{d\sigma}{d\omega}$ (mb/sr)	error (mb/sr)
$\pi^+$			
	25.53	0.5195E-01	0.1892E-01
	30.62	0.9598E-01	0.1311E-01
	35.71	0.4271E-01	0.9889E-02
	40.80	0.5256E-01	0.7517E-02
	45.88	0.1077E-01	0.6900E-02
	50.95	0.9647E-02	0.3407E-02
	56.02	0.7046E-02	0.7473E-02
	61.08	0.3785E-02	0.1880E-02
	66.12	0.1998E-02	0.2351E-02
	71.17	0.5099E-02	0.1710E-02
	76.20	0.8074E-02	0.4085E-02
	81.22	0.4411E-02	0.1537E-02
	86.23	0.2994E-02	0.2309E-02
	91.24	0.1701E-02	0.7968E-03
$\pi^-$			
	25.53	0.2324E+00	0.2904E-01
	30.62	0.2242E+00	0.2483E-01
	35.71	0.1761E+00	0.2054E-01
	40.80	0.1733E+00	0.1500E-01
	45.88	0.9126E-01	0.1245E-01
	50.95	0.3430E-01	0.4741E-02
	56.02	0.1501E-01	0.1154E-01
	61.08	0.5336E-02	0.3036E-02
	66.12	0.1059E-01	0.1051E-01
	71.17	0.7749E-02	0.2058E-02
	76.20	0.4113E-02	0.9650E-02
	81.22	0.1147E-01	0.3767E-02
	86.23	0.1130E-01	0.9852E-02
	91.24	0.2563E-02	0.1484E-02

10.7 MeV  $\pi^\pm$  tabulated data

	$\theta_{\text{cm}}$ (deg)	$\frac{d\sigma}{d\omega}$ (mb/sr)	error (mb/sr)
$\pi^+$			
	25.53	0.3764E-01	0.1182E-01
	30.62	0.2800E-01	0.7427E-02
	35.71	0.2281E-01	0.6013E-02
	40.80	0.1537E-01	0.3918E-02
	45.88	0.2078E-01	0.4591E-02
	50.95	0.3128E-01	0.2933E-02
	56.02	0.3037E-01	0.8607E-02
	61.08	0.3481E-01	0.2771E-02
	66.12	0.2906E-01	0.3983E-02
	71.17	0.2765E-01	0.2174E-02
	76.20	0.3120E-01	0.4999E-02
	81.22	0.2011E-01	0.1945E-02
	86.23	0.2329E-01	0.3441E-02
	91.24	0.1502E-01	0.1247E-02
$\pi^-$			
	56.02	0.9440E-02	0.1073E-01
	61.08	0.5718E-02	0.3244E-02
	71.17	0.3396E-02	0.1443E-02
	76.20	0.5127E-03	0.6930E-02
	81.22	0.9953E-03	0.2374E-02
	91.24	0.3532E-02	0.1605E-02

11.3 MeV  $\pi^\pm$  tabulated data

	$\theta_{\text{cm}}$ (deg)	$\frac{d\sigma}{d\omega}$ (mb/sr)	error (mb/sr)
$\pi^+$			
	35.71	0.2940E-01	0.6215E-02
	40.80	0.9606E-02	0.3822E-02
	45.88	0.1223E-01	0.4406E-02
	50.95	0.1973E-01	0.2715E-02
	56.02	0.1255E-01	0.6637E-02
	61.08	0.1310E-01	0.1828E-02
	66.12	0.1121E-01	0.2678E-02
	71.17	0.6735E-02	0.1395E-02
	76.20	0.5845E-02	0.3143E-02
	81.22	0.7287E-02	0.1387E-02
	86.23	0.7111E-02	0.2380E-02
	91.24	0.5348E-02	0.8875E-03
$\pi^-$			
	40.80	0.1219E-01	0.7012E-02
	45.88	0.3430E-02	0.5421E-02
	50.95	0.6317E-02	0.2997E-02
	56.02	0.1515E-01	0.1134E-01
	61.08	0.1425E-01	0.3950E-02
	66.12	0.6439E-02	0.1087E-01
	71.17	0.8947E-02	0.1774E-02
	76.20	0.4929E-02	0.7826E-02
	81.22	0.2613E-02	0.2540E-02
	91.24	0.3539E-02	0.1705E-02

11.9 MeV  $\pi^\pm$  tabulated data

	$\theta_{\text{cm}}$ (deg)	$\frac{d\sigma}{d\omega}$ (mb/sr)	error (mb/sr)
$\pi^+$			
	25.53	0.1633E+00	0.1576E-01
	30.62	0.2151E+00	0.1147E-01
	35.71	0.2529E+00	0.1053E-01
	40.80	0.1934E+00	0.7224E-02
	45.88	0.1290E+00	0.7901E-02
	50.95	0.8269E-01	0.4172E-02
	56.02	0.5747E-01	0.1077E-01
	61.08	0.2254E-01	0.2559E-02
	66.12	0.2251E-01	0.3807E-02
	71.17	0.1355E-01	0.1879E-02
	76.20	0.1380E-01	0.3622E-02
	81.22	0.1256E-01	0.1714E-02
	86.23	0.9648E-02	0.2667E-02
	91.24	0.1421E-01	0.1293E-02
$\pi^-$			
	25.53	0.3271E+00	0.2671E-01
	30.62	0.3598E+00	0.1811E-01
	35.71	0.3197E+00	0.1732E-01
	40.80	0.2693E+00	0.1506E-01
	45.88	0.1970E+00	0.1243E-01
	50.95	0.1078E+00	0.5814E-02
	56.02	0.3021E-01	0.1359E-01
	61.08	0.3738E-01	0.5675E-02
	66.12	0.7687E-02	0.1176E-01
	71.17	0.2909E-01	0.2667E-02
	76.20	0.1211E-01	0.9207E-02
	81.22	0.2232E-01	0.4400E-02
	86.23	0.1094E-01	0.1077E-01
	91.24	0.1480E-01	0.2725E-02

12.5 MeV  $\pi^\pm$  tabulated data

	$\theta_{\text{cm}}$ (deg)	$\frac{d\sigma}{d\omega}$ (mb/sr)	error (mb/sr)
$\pi^+$			
	25.53	0.3588E-01	0.1242E-01
	30.62	0.3869E-01	0.8048E-02
	35.71	0.5302E-01	0.6626E-02
	40.80	0.6132E-01	0.5230E-02
	45.88	0.5973E-01	0.6249E-02
	50.95	0.6155E-01	0.3913E-02
	56.02	0.5233E-01	0.1076E-01
	61.08	0.5670E-01	0.3607E-02
	66.12	0.5405E-01	0.5333E-02
	71.17	0.4594E-01	0.2940E-02
	76.20	0.4273E-01	0.5819E-02
	81.22	0.3569E-01	0.2616E-02
	86.23	0.3557E-01	0.4200E-02
	91.24	0.2470E-01	0.1650E-02
$\pi^-$			
	25.53	0.1007E+00	0.2046E-01
	30.62	0.5242E-01	0.1098E-01
	35.71	0.5337E-01	0.1022E-01
	40.80	0.4877E-01	0.8908E-02
	45.88	0.3199E-01	0.7357E-02
	50.95	0.2590E-01	0.3985E-02
	56.02	0.2274E-01	0.1303E-01
	61.08	0.1416E-01	0.4396E-02
	66.12	0.1076E-01	0.1256E-01
	71.17	0.4891E-02	0.1695E-02
	76.20	0.5812E-02	0.8844E-02
	81.22	0.7793E-02	0.3402E-02
	86.23	0.1511E-02	0.9502E-02
	91.24	0.8373E-02	0.2290E-02

12.9 MeV  $\pi^\pm$  tabulated data

	$\theta_{\text{cm}}$ (deg)	$\frac{d\sigma}{d\omega}$ (mb/sr)	error (mb/sr)
$\pi^+$			
	30.62	0.2084E-01	0.7645E-02
	35.71	0.1172E-01	0.7000E-02
	40.80	0.8090E-02	0.4489E-02
	45.88	0.1095E-01	0.4651E-02
	50.95	0.8866E-02	0.2845E-02
	56.02	0.1980E-01	0.8385E-02
	61.08	0.1318E-01	0.2334E-02
	66.12	0.1089E-01	0.3072E-02
	71.17	0.6324E-02	0.1576E-02
	76.20	0.9429E-02	0.3854E-02
	81.22	0.3479E-02	0.1350E-02
	86.23	0.4098E-02	0.2468E-02
	91.24	0.4728E-02	0.1036E-02
$\pi^-$			
	30.62	0.2092E-01	0.1023E-01
	35.71	0.1171E-01	0.9439E-02
	40.80	0.5439E-02	0.7570E-02
	45.88	0.1253E-01	0.6010E-02
	50.95	0.7326E-02	0.3306E-02
	61.08	0.9862E-02	0.4065E-02
	66.12	0.2583E-02	0.1151E-01
	71.17	0.4274E-02	0.1646E-02
	81.22	0.8672E-03	0.2570E-02
	86.23	0.1664E-02	0.9965E-02
	91.24	0.7119E-02	0.2187E-02

13.1 MeV  $\pi^\pm$  tabulated data

	$\theta_{\text{cm}}$ (deg)	$\frac{d\sigma}{d\omega}$ (mb/sr)	error (mb/sr)
$\pi^+$			
	25.53	0.1858E-01	0.1185E-01
	30.62	0.1801E-01	0.7361E-02
	35.71	0.6733E-01	0.8166E-02
	40.80	0.4347E-01	0.4970E-02
	45.88	0.3190E-01	0.5350E-02
	50.95	0.1790E-01	0.2852E-02
	56.02	0.3087E-03	0.6636E-02
	61.08	0.6833E-02	0.1896E-02
	66.12	0.2724E-02	0.2487E-02
	71.17	0.3152E-02	0.1306E-02
	81.22	0.8364E-03	0.1128E-02
	86.23	0.3668E-02	0.2236E-02
	91.24	0.5685E-02	0.9567E-03
$\pi^-$			
	25.53	0.7043E-01	0.1807E-01
	30.62	0.4881E-01	0.1212E-01
	35.71	0.3377E-01	0.1064E-01
	40.80	0.2185E-01	0.7962E-02
	45.88	0.1973E-01	0.6425E-02
	50.95	0.1173E-01	0.3602E-02
	56.02	0.5593E-02	0.1213E-01
	61.08	0.1582E-02	0.3661E-02
	81.22	0.4741E-02	0.2997E-02
	91.24	0.1723E-02	0.1893E-02

14.1 MeV  $\pi^\pm$  tabulated data

	$\theta_{\text{cm}}$ (deg)	$\frac{d\sigma}{d\omega}$ (mb/sr)	error (mb/sr)
$\pi^+$			
	25.53	0.4084E-01	0.1316E-01
	30.62	0.6909E-01	0.9171E-02
	35.71	0.7331E-01	0.8340E-02
	40.80	0.8658E-01	0.5916E-02
	45.88	0.8425E-01	0.7077E-02
	50.95	0.7711E-01	0.4221E-02
	56.02	0.5524E-01	0.1107E-01
	61.08	0.5504E-01	0.3639E-02
	66.12	0.4467E-01	0.5039E-02
	71.17	0.3519E-01	0.2585E-02
	76.20	0.2841E-01	0.5099E-02
	81.22	0.2718E-01	0.2364E-02
	86.23	0.1765E-01	0.3209E-02
	91.24	0.2361E-01	0.1582E-02
$\pi^-$			
	25.53	0.6445E-01	0.1931E-01
	30.62	0.1037E+00	0.1331E-01
	35.71	0.1321E+00	0.1288E-01
	40.80	0.1458E+00	0.1230E-01
	45.88	0.1178E+00	0.1079E-01
	50.95	0.9559E-01	0.5804E-02
	56.02	0.8679E-01	0.1831E-01
	61.08	0.5351E-01	0.6564E-02
	66.12	0.1663E-01	0.1431E-01
	71.17	0.3417E-01	0.2927E-02
	76.20	0.1363E-01	0.1034E-01
	81.22	0.1738E-01	0.4405E-02
	86.23	0.4476E-02	0.1022E-01
	91.24	0.1835E-01	0.3222E-02



14.4 MeV  $\pi^\pm$  tabulated data

	$\theta_{\text{cm}}$ (deg)	$\frac{d\sigma}{d\omega}$ (mb/sr)	error (mb/sr)
$\pi^+$			
	25.53	0.2939E-01	0.1249E-01
	30.62	0.1244E-01	0.8572E-02
	35.72	0.2747E-01	0.7561E-02
	40.80	0.5308E-01	0.5845E-02
	45.88	0.3676E-01	0.6815E-02
	50.95	0.2623E-01	0.3563E-02
	56.02	0.1463E-01	0.9010E-02
	61.08	0.1294E-01	0.2763E-02
	66.13	0.3839E-02	0.3800E-02
	71.17	0.5695E-02	0.1697E-02
	76.20	0.6798E-02	0.4003E-02
	81.22	0.5678E-03	0.1648E-02
	86.24	0.2898E-02	0.2682E-02
	91.24	0.1185E-02	0.1149E-02
$\pi^-$			
	25.53	0.4952E-01	0.1939E-01
	30.62	0.6839E-02	0.1155E-01
	35.72	0.5513E-01	0.1132E-01
	40.80	0.4473E-01	0.1080E-01
	45.88	0.2628E-01	0.8977E-02
	50.95	0.3719E-01	0.4745E-02
	56.02	0.2352E-01	0.1627E-01
	61.08	0.1105E-01	0.5096E-02
	66.13	0.2389E-02	0.1309E-01
	71.17	0.3994E-02	0.2154E-02
	76.20	0.7401E-02	0.9162E-02
	81.22	0.6277E-02	0.3746E-02
	86.24	0.2003E-02	0.1017E-01
	91.24	0.1753E-02	0.2219E-02

14.6 MeV  $\pi^\pm$  tabulated data

	$\theta_{\text{cm}}$ (deg)	$\frac{d\sigma}{d\omega}$ (mb/sr)	error (mb/sr)
$\pi^+$			
	25.53	0.5434E-01	0.1295E-01
	30.62	0.8241E-01	0.9756E-02
	35.72	0.7098E-01	0.8349E-02
	40.80	0.6560E-01	0.6468E-02
	45.88	0.4894E-01	0.7412E-02
	50.95	0.3666E-01	0.3960E-02
	56.02	0.3590E-01	0.1055E-01
	61.08	0.8769E-03	0.2821E-02
	66.13	0.1083E-01	0.3765E-02
	71.17	0.5471E-02	0.2109E-02
	81.22	0.1017E-01	0.1940E-02
	86.24	0.1357E-01	0.3642E-02
	91.24	0.9282E-02	0.1329E-02
$\pi^-$			
	25.53	0.5860E-01	0.1984E-01
	30.62	0.9355E-01	0.1378E-01
	35.72	0.8263E-01	0.1227E-01
	40.80	0.4306E-01	0.1190E-01
	45.88	0.6243E-01	0.1137E-01
	50.95	0.2929E-01	0.5256E-02
	56.02	0.6928E-02	0.1380E-01
	61.08	0.1512E-01	0.6536E-02
	71.17	0.1041E-01	0.2618E-02
	81.22	0.1542E-01	0.4219E-02
	86.24	0.1495E-01	0.1175E-01
	91.24	0.8580E-02	0.2572E-02

15.0 MeV  $\pi^\pm$  tabulated data

	$\theta_{\text{cm}}$ (deg)	$\frac{d\sigma}{d\omega}$ (mb/sr)	error (mb/sr)
$\pi^+$			
	25.53	0.9475E-01	0.1381E-01
	30.62	0.8344E-01	0.9147E-02
	35.72	0.9847E-01	0.9293E-02
	40.80	0.1180E+00	0.7039E-02
	45.88	0.1203E+00	0.8811E-02
	50.95	0.1277E+00	0.5278E-02
	56.02	0.9146E-01	0.1341E-01
	61.08	0.4757E-01	0.4397E-02
	66.13	0.3342E-01	0.4751E-02
	71.17	0.1719E-01	0.2771E-02
	76.20	0.8628E-02	0.3998E-02
	81.22	0.1779E-01	0.2314E-02
	86.24	0.2924E-01	0.4339E-02
	91.24	0.2706E-01	0.1862E-02
$\pi^-$			
	25.53	0.1169E+00	0.2236E-01
	30.62	0.1214E+00	0.1426E-01
	35.72	0.1377E+00	0.1401E-01
	40.80	0.1279E+00	0.1440E-01
	45.88	0.1102E+00	0.1384E-01
	50.95	0.1242E+00	0.6740E-02
	56.02	0.7370E-01	0.1766E-01
	61.08	0.8236E-01	0.1051E-01
	66.13	0.1674E-01	0.1390E-01
	71.17	0.1739E-01	0.3153E-02
	76.20	0.3594E-02	0.8877E-02
	81.22	0.1733E-01	0.4458E-02
	86.24	0.1116E-01	0.1125E-01
	91.24	0.2578E-01	0.3537E-02

16.5 MeV  $\pi^\pm$  tabulated data

	$\theta_{\text{cm}}$ (deg)	$\frac{d\sigma}{d\omega}$ (mb/sr)	error (mb/sr)
$\pi^+$			
	25.53	0.1117E+00	0.2550E-01
	30.62	0.1334E+00	0.1774E-01
	35.72	0.8587E-01	0.1168E-01
	40.80	0.1184E+00	0.1140E-01
	45.88	0.6140E-01	0.1182E-01
	50.95	0.4800E-01	0.6617E-02
	61.08	0.2757E-01	0.3989E-02
	66.13	0.2262E-01	0.6752E-02
	71.17	0.2301E-01	0.3095E-02
	76.20	0.8762E-02	0.7493E-02
	81.22	0.1245E-01	0.3445E-02
	86.24	0.2536E-01	0.6522E-02
	91.24	0.1625E-01	0.2699E-02
$\pi^-$			
	25.53	0.1635E+00	0.4002E-01
	30.62	0.1068E+00	0.2417E-01
	35.72	0.9617E-01	0.1699E-01
	40.80	0.4135E-01	0.1673E-01
	45.88	0.1955E-01	0.1325E-01
	50.95	0.1708E-01	0.7389E-02
	61.08	0.4459E-01	0.8039E-02
	71.17	0.1716E-01	0.3108E-02
	86.24	0.2611E-02	0.1776E-01

16.9 MeV  $\pi^\pm$  tabulated data

	$\theta_{\text{cm}}$ (deg)	$\frac{d\sigma}{d\omega}$ (mb/sr)	error (mb/sr)
$\pi^+$			
	25.53	0.1364E+00	0.1857E-01
	30.62	0.2051E+00	0.1288E-01
	35.72	0.1846E+00	0.1157E-01
	40.80	0.1508E+00	0.8535E-02
	45.88	0.9650E-01	0.9440E-02
	50.95	0.5769E-01	0.5251E-02
	56.02	0.3554E-01	0.1303E-01
	61.08	0.6247E-02	0.3503E-02
	66.13	0.1841E-02	0.4592E-02
	71.17	0.1914E-03	0.2557E-02
	76.20	0.1629E-01	0.6547E-02
	81.22	0.6389E-02	0.2699E-02
	86.24	0.4206E-02	0.3299E-02
	91.24	0.9425E-02	0.1949E-02
$\pi^-$			
	25.53	0.2458E+00	0.2763E-01
	30.62	0.2355E+00	0.1849E-01
	35.72	0.2068E+00	0.1885E-01
	40.80	0.1286E+00	0.1488E-01
	45.88	0.8546E-01	0.1211E-01
	50.95	0.2607E-01	0.5883E-02
	56.02	0.5142E-02	0.1589E-01
	61.08	0.1800E-02	0.6539E-02
	66.13	0.5427E-02	0.1650E-01
	71.17	0.1449E-02	0.2918E-02
	76.20	0.1315E-02	0.1194E-01
	81.22	0.5061E-02	0.4488E-02
	86.24	0.7475E-02	0.1306E-01
	91.24	0.7396E-02	0.3597E-02

17.2 MeV  $\pi^\pm$  tabulated data

	$\theta_{\text{cm}}$ (deg)	$\frac{d\sigma}{d\omega}$ (mb/sr)	error (mb/sr)
$\pi^+$			
	25.53	0.1007E+00	0.1783E-01
	30.62	0.7009E-01	0.1088E-01
	35.72	0.6831E-01	0.1033E-01
	40.80	0.7131E-01	0.7755E-02
	45.88	0.6541E-01	0.1105E-01
	50.95	0.4674E-01	0.6145E-02
	56.02	0.7418E-01	0.1534E-01
	61.08	0.7432E-01	0.5819E-02
	66.13	0.7319E-01	0.6859E-02
	71.17	0.6217E-01	0.4667E-02
	76.20	0.6797E-01	0.9079E-02
	81.22	0.6787E-01	0.4268E-02
	86.24	0.6025E-01	0.6001E-02
	91.24	0.3641E-01	0.2569E-02
$\pi^-$			
	25.53	0.1067E+00	0.2434E-01
	30.62	0.9298E-01	0.1641E-01
	35.72	0.7468E-01	0.1725E-01
	40.80	0.1056E+00	0.1430E-01
	45.88	0.6970E-01	0.1447E-01
	50.95	0.7932E-01	0.7054E-02
	56.02	0.5613E-01	0.2070E-01
	61.08	0.1094E+00	0.1007E-01
	66.13	0.9792E-01	0.2324E-01
	71.17	0.1046E+00	0.6042E-02
	76.20	0.6389E-01	0.1761E-01
	81.22	0.8812E-01	0.8888E-02
	86.24	0.5544E-01	0.1705E-01
	91.24	0.4593E-01	0.5227E-02

17.6 MeV  $\pi^\pm$  tabulated data

	$\theta_{\text{cm}}$ (deg)	$\frac{d\sigma}{d\omega}$ (mb/sr)	error (mb/sr)
$\pi^+$			
	25.53	0.1608E+00	0.2043E-01
	30.62	0.2003E+00	0.1531E-01
	35.72	0.1493E+00	0.1364E-01
	40.80	0.1542E+00	0.1003E-01
	50.95	0.4770E-01	0.6207E-02
	56.02	0.3834E-01	0.1504E-01
	61.08	0.1072E-01	0.5948E-02
	66.13	0.1839E-01	0.5820E-02
	71.17	0.1471E-01	0.4748E-02
	76.20	0.2635E-01	0.7688E-02
	81.22	0.2848E-01	0.3615E-02
	86.24	0.2791E-01	0.5775E-02
	91.24	0.3022E-01	0.2559E-02
$\pi^-$			
	25.53	0.2554E+00	0.3393E-01
	30.62	0.2301E+00	0.2184E-01
	35.72	0.2503E+00	0.2207E-01
	40.80	0.1698E+00	0.1895E-01
	50.95	0.5982E-01	0.7685E-02
	56.02	0.5743E-01	0.2337E-01
	66.13	0.1112E-01	0.2124E-01
	71.17	0.2066E-01	0.5536E-02
	76.20	0.3863E-01	0.1810E-01
	81.22	0.2646E-01	0.7206E-02
	86.24	0.2466E-01	0.1768E-01
	91.24	0.2562E-01	0.4672E-02

18.3 MeV  $\pi^\pm$  tabulated data

	$\theta_{\text{cm}}$ (deg)	$\frac{d\sigma}{d\omega}$ (mb/sr)	error (mb/sr)
$\pi^+$			
	25.53	0.1091E+00	0.1649E-01
	30.62	0.1101E+00	0.1184E-01
	35.72	0.6236E-01	0.1262E-01
	40.80	0.8940E-01	0.7697E-02
	45.88	0.6781E-01	0.8294E-02
	50.95	0.3015E-01	0.4394E-02
	61.08	0.6283E-02	0.3343E-02
	66.13	0.1643E-01	0.4679E-02
	71.17	0.8873E-02	0.2540E-02
	76.20	0.1786E-01	0.5777E-02
	81.22	0.1312E-01	0.2579E-02
	86.24	0.6570E-02	0.3747E-02
	91.24	0.6486E-02	0.1583E-02
$\pi^-$			
	25.53	0.1452E+00	0.2589E-01
	30.62	0.1006E+00	0.1592E-01
	35.72	0.9299E-01	0.1666E-01
	40.80	0.4642E-01	0.1643E-01
	45.88	0.6658E-01	0.1221E-01
	50.95	0.2151E-01	0.5624E-02
	61.08	0.1327E-01	0.6142E-02
	66.13	0.4440E-02	0.1582E-01
	71.17	0.1670E-01	0.2875E-02
	76.20	0.1134E-01	0.1222E-01
	81.22	0.1803E-01	0.5285E-02
	86.24	0.1816E-01	0.1473E-01
	91.24	0.6354E-02	0.4034E-02



18.7 MeV  $\pi^\pm$  tabulated data

	$\theta_{\text{cm}}$ (deg)	$\frac{d\sigma}{d\omega}$ (mb/sr)	error (mb/sr)
$\pi^+$			
	25.53	0.4253E-01	0.1321E-01
	30.62	0.6870E-01	0.9777E-02
	35.72	0.2240E-01	0.9525E-02
	40.80	0.3670E-01	0.6315E-02
	45.88	0.4168E-01	0.7520E-02
	50.95	0.2426E-01	0.4241E-02
	56.02	0.1304E-01	0.1165E-01
	61.08	0.6683E-02	0.2981E-02
	66.13	0.8795E-02	0.4455E-02
	71.17	0.1273E-01	0.2487E-02
	76.20	0.1245E-01	0.5065E-02
	81.22	0.5254E-02	0.2326E-02
	86.24	0.1280E-01	0.4317E-02
	91.24	0.9816E-02	0.1922E-02
$\pi^-$			
	25.53	0.1107E+00	0.2433E-01
	30.62	0.1036E+00	0.1518E-01
	35.72	0.6292E-01	0.1332E-01
	40.80	0.6864E-01	0.1445E-01
	45.88	0.1659E-01	0.9594E-02
	50.95	0.1053E-01	0.4781E-02
	66.13	0.2982E-02	0.1339E-01
	71.17	0.7664E-02	0.2405E-02
	76.20	0.1160E-01	0.1146E-01
	81.22	0.7798E-02	0.5418E-02
	86.24	0.3451E-02	0.1220E-01
	91.24	0.4988E-02	0.2726E-02

18.9 MeV  $\pi^\pm$  tabulated data

	$\theta_{\text{cm}}$ (deg)	$\frac{d\sigma}{d\omega}$ (mb/sr)	error (mb/sr)
$\pi^+$			
	25.53	0.1692E-01	0.1300E-01
	30.62	0.2407E-01	0.9072E-02
	35.72	0.3340E-01	0.9364E-02
	40.80	0.1855E-01	0.6251E-02
	45.88	0.3824E-01	0.7344E-02
	50.95	0.1872E-01	0.4235E-02
	56.02	0.1035E-01	0.1210E-01
	61.08	0.1381E-01	0.3167E-02
	66.13	0.2452E-01	0.5195E-02
	71.17	0.9216E-02	0.2460E-02
	76.20	0.1056E-01	0.5536E-02
	81.22	0.1801E-01	0.2700E-02
	86.24	0.1164E-01	0.4334E-02
	91.24	0.5471E-02	0.1875E-02
$\pi^-$			
	25.53	0.5522E-01	0.2280E-01
	30.62	0.3946E-01	0.1507E-01
	35.72	0.6037E-01	0.1313E-01
	40.80	0.1638E-01	0.1358E-01
	45.88	0.2042E-01	0.9659E-02
	50.95	0.1129E-01	0.4849E-02
	61.08	0.9398E-02	0.5738E-02
	66.13	0.2444E-02	0.1334E-01
	71.17	0.7298E-02	0.2384E-02
	81.22	0.1164E-01	0.5669E-02
	86.24	0.1344E-01	0.1331E-01
	91.24	0.7229E-02	0.3175E-02

## BIBLIOGRAPHY

- [AJ86] F. Ajzenberg-Selove, Nuc. Phys. **A449**, 113 (1986).
- [AL69] W. P. Alford and K. H. Purser, Nuc. Phys. **A132**, 86 (1969).
- [AM79] J. F. Aman, *et. al.*, IEEE Trans. Nucl. Sci. **NS-26**, 4389 (1979).
- [AT81] L. G. Atencio, *et. al.*, Nucl. Instr. Meth. **187**, 381 (1981).
- [AU67] E. H. Auerbach, D. M. Fleming, and M. M. Sternheim, Phys. Rev. **162**, 1683 (1967).
- [CH87] S. Chakravarti, *et. al.*, Phys. Rev. C **35**, 2197 (1987).
- [CO80] W. B. Cottingham and D. B. Holtkamp, Phys. Rev. Lett. **45**, 1830 (1980).
- [DE79] D. Dehnhard, *et. al.*, Phys. Rev. C **43**, 1091 (1979).
- [DE87] H. De Vries, *et. al.*, Atomic and Nuclear Data Tables **36**, 503 (1987).
- [EI74] R. A. Eisenstein and G. A. Miller, Comput. Phys. Commun. **8**, 130 (1974).
- [EI76A] R. A. Eisenstein and G. A. Miller, Comput. Phys. Commun. **11**, 95 (1976).
- [EI76B] R. A. Eisenstein and F. Tabakin, Comput. Phys. Commun. **12**, 237 (1976).
- [EN79] P. M. Endt, Atomic Data and Nuclear Data Tables **23**, 14 (1979).
- [FR53] N. C. Francis and K. M. Watson, Phys. Rev. **92**, 291 (1953).

- [FRA] Codes modified by Mike Franey to run on Vax/VMS.
- [FRB] Point densities provided by Mike Franey.
- [HO85] D. B. Holtkamp *et. al.*, Phys. Rev. C **31**, 957 (1985).
- [HO77] Y. Horikawa *et. al.*, Nucl. Phys. **A278**, 297 (1977).
- [JA89] F. James and M. Roos, Computer Program MINUIT, CERN Program Library entry D506, Copyright CERN, Geneva Switzerland (1989).
- [KA64] G. Källén, *Elementary Particle Physics*, 71-74, (Addison-Wesley Publishing Company, Inc. 1964).
- [KE59] A. K. Kerman, *et. al.*, Annals of Physics **8**, 551 (1959).
- [KI84] R. R. Kiziah, Ph. D. Thesis, The University of Texas at Austin, (1984).
- [KI55] L. S. Kisslinger, Phys. Rev. **98**, 761 (1955).
- [KO69] D. S. Koltun, *Advances in Nuclear Science*, Vol. 3, edited by M. Baranger and E. Vogt, 71, ff (Plenum Press, 1969).
- [LA84] *LAMPF Users Handbook*, Los Alamos Scientific Laboratory, MP-DO-3-UHB (Rev.), (1984).
- [LE80] T.S. H. Lee and D. Kurath, Phys. Rev. C **21**, 293 (1980).
- [LE80A] T.S. H. Lee and R. D. Lawson, Phys. Rev. C **21**, 679 (1980).
- [LE73] M. Leon, *Particle Physics: An Introduction*, 125-131, (Academic Press 1973).
- [LI70] S. Lie *et. al.*, Nuc. Phys. **A156**, 449 (1970).
- [LI77] M. Stanley Livingston, Los Alamos Scientific Laboratory Report LA-6878-MS, 1977 (unpublished).

- [MA76] M. W. S. Macauley *et. al.*, J. Phys. G **2**, L35 (1976).
- [ME66] A. C. Melissinos, *Experiments in Modern Physics*, 158 (1966).
- [MI75] D. J. Millener and D. Kurath, Nucl. Phys. **A255**, 315 (1975).
- [MO] C. L. Morris and L. G. Atencio, (private communication).
- [MO82] C. L. Morris, Nucl. Instr. Meth. **196**, 263 (1982).
- [OS82] E. Oset and D. Strottman, Nucl. Phys. **A377**, 297 (1982).
- [PR75] M. A. Preston and R. K. Bhaduri, *Structure of the Nucleus* 193, (Addison-Wesley 1975).
- [RO78] G. Rowe, M. Salamon, R. H. Landau, Phys. Rev. C **18**, 584 (1978).
- [SE85] S. J. Seestrom-Morris, *et. al.*, Phys. Rev. C **31**, 923 (1985).
- [SI81] E. R. Siciliano and G. E. Walker, Phys. Rev. C **23**, 2661 (1981).
- [SM78] L. E. Smith, computer program LOAF, Physics Department, University of Texas at Austin, Austin, TX 78712, (1978).
- [SU76] T. Suzuki, Nuc. Phys. **A267**, 109 (1976).
- [TH70] H. A. Thiessen and S. Sobottka, Los Alamos Scientific Laboratory Report LA-4535-MS, 1970 (unpublished).
- [YU35] H. Yukawa, Proceedings of the Mathematical Society of Japan **17**, 48 (1935).

## VITA

David Patrick Saunders was born in Reidsville, North Carolina on August 31, 1959, the son of Percy L. and Inez R. Saunders. After completing his work at Fort Johnson High School, Charleston, South Carolina, he entered the USAF Academy at Colorado Springs, Colorado. He received a Bachelor of Science degree and a comission as a Second Lieutenant from the Academy in May, 1981. The following year he was employed at the Air Force Weapons Laboratory at Kirtland Air Force Base, New Mexico. In August, 1982 he entered The Graduate School of The University of Texas at Austin, and received the degree of Master of Arts in May 1984, after which he was employed at the Weapons Laboratory, married the former Deborah Stephens, had a son, David, and moved to the Air Force Academy, where he became an Assistant Professor of Physics. He continued his work towards a Doctorate, and in June 1990 again became a full time graduate student at The University of Texas at Austin.

Permanent address: 398 Richard Court  
Los Alamos, New Mexico  
87544

This dissertation was typeset<sup>1</sup> with L<sup>A</sup>T<sub>E</sub>X by the author.

---

1

L<sup>A</sup>T<sub>E</sub>X document preparation system was developed by Leslie Lamport as a special version of Donald Knuth's T<sub>E</sub>X program for computer typesetting. T<sub>E</sub>X is a trademark of the American Mathematical Society. The L<sup>A</sup>T<sub>E</sub>X macro package for The University of Texas at Austin dissertation format was written by Khe-Sing The.